Appendix J

ANALYSIS OF INHIBITION OF FAULTING AT FAULT BRANCHES
Paul Somerville

ANALYSIS OF INHIBITION OF FAULTING AT FAULT BRANCHES

Paul Somerville, URS, 6 April 2009

Objective

The branching rupture scenario addressed in this study is one in which rupture begins on the main fault and branches onto the branch fault (with or without continuing to rupture on the main fault past the branch point). For Diablo Canyon, the scenario is one in which rupture begins on the Hosgri fault and branches onto the Shoreline fault. Other modes of branching, for example from the branch fault onto the main fault (e.g. Fliss et al., 2005), are not addressed in this study.

Method

We first compile a list of fault geometries with branch faulting and observed ruptures, including both cases in which there was rupture on the branch fault and cases in which there was no rupture on the branch fault. Next, we compare the observed cases with the predictions of the Kame et al. (2003) model to assess whether they are consistent with that model. For cases with rupture on the branch fault, we assess its impacts on ground motions recorded near the branch fault based on observed ground motions and previously published simulations.

The Kame et al (2003) Fault Branching Model

According to Kame et al (2003), branching of rupture from one fault to another can only occur under certain conditions. Poliakov *et al.* (2002) and Kame *et al.* (2003) have shown that the propensity of the rupture path to follow a fault branch is determined by the preexisting stress state, branch angle, and incoming rupture velocity at the branch location. The predictions of the Kame et al. (2003) model use the following three parameters:

Ψ = angle between the direction of maximum compressive stress (S_{max}) and the fault strike

φ = angle between the main fault and the branch fault

v_r = rupture velocity (expressed as a fraction of the shear wave velocity c_s)

The geometry of these parameters is shown in Figure 1.
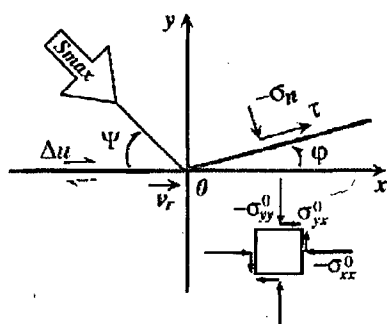

Figure 1. Configuration of a preexisting branched fault system and prestress state. Gray lines indicate potential rupture surface and black line indicates propagating rupture. Source: Kame et al. (2003).
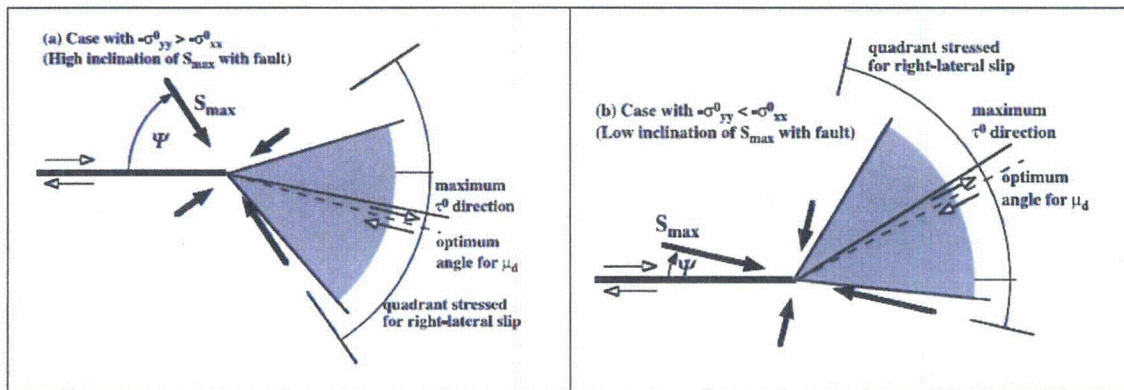
Figure 2. Qualitative prediction of the directions over which the larger scale prestress states favor right-lateral shear along bend paths. (a) Fault-normal precompression is dominant, $\Psi > 45°$, allowing rupture to continue along bend paths primarily to the extensional side. (b) Fault-parallel precompression is dominant, $\Psi < 45°$, allowing rupture to continue along bend paths primarily to the compressional side. The gray zones indicate the angle range where the initial shear stress is larger than the frictional resistance. Source: Kame et al. (2003).

As shown in Figure 2, values of $\Psi > 45°$ generally favor branch faulting on the extensional side of the main fault, while values of $\Psi < 45°$ generally favor branch faulting on the compressional side of the main fault. Figures 1 through 6 pertain to right-lateral faulting. For left-lateral faulting, these figures are rotated about the X axis.

The predictions of the model for four values of Ψ, namely $56°$, $45°$, $25°$ and $13°$, are shown in Figures 3 through 6. In each case, the predictions are shown for each combination of four values of φ and three values of rupture velocity c_s. The values of φ are $30°$, $15°$, $-15°$, and $-30°$, and the values of v_r are $0.6c_s$, $0.8\ c_s$, and $0.9\ c_s$. The branch fault is on the compressional side of the fault for positive values of φ, and on the extensional side of the fault negative values of φ. These figures show final rupture traces in the vicinity of the intersection of the main fault with the branch fault. L_{stop} indicates the length of arrested rupture, given in terms of the slip-weakening zone size R_0 for low speed rupture along the main fault. Arrested rupture is indicated by the lines that have been highlighted in pink.

Application to the Kame et al. (2003) model to the Hosgri – Shoreline Fault Branch

Using the Kame et al (2003) model, branching of rupture from the Hosgri onto the Shoreline fault is physically prohibited under the current stress regime. Taking the S_{max} (orientation of the maximum compressional stress) to be N15E (McLaren, 2001), and strike angles of N25W for the Hosgri and N50W for the Shoreline fault, we obtain $\Psi = 45°$ and $\varphi = +25°$. These conditions pertain to Figure 4, top row, which shows rupture continuing on the main fault (shown in black) and strongly inhibited on the branch fault (shown in pink) for all three values of rupture velocity.

The statistics of fault branching angles in California have been analyzed by Ando et al. (2009). They find that fault branching angles have a skewed distribution of values that is approximately symmetrical on the compressional and dilatational sides of the fault, with a peak at $17°$.

High Inclination of S_{max}, $\Psi = 56°$

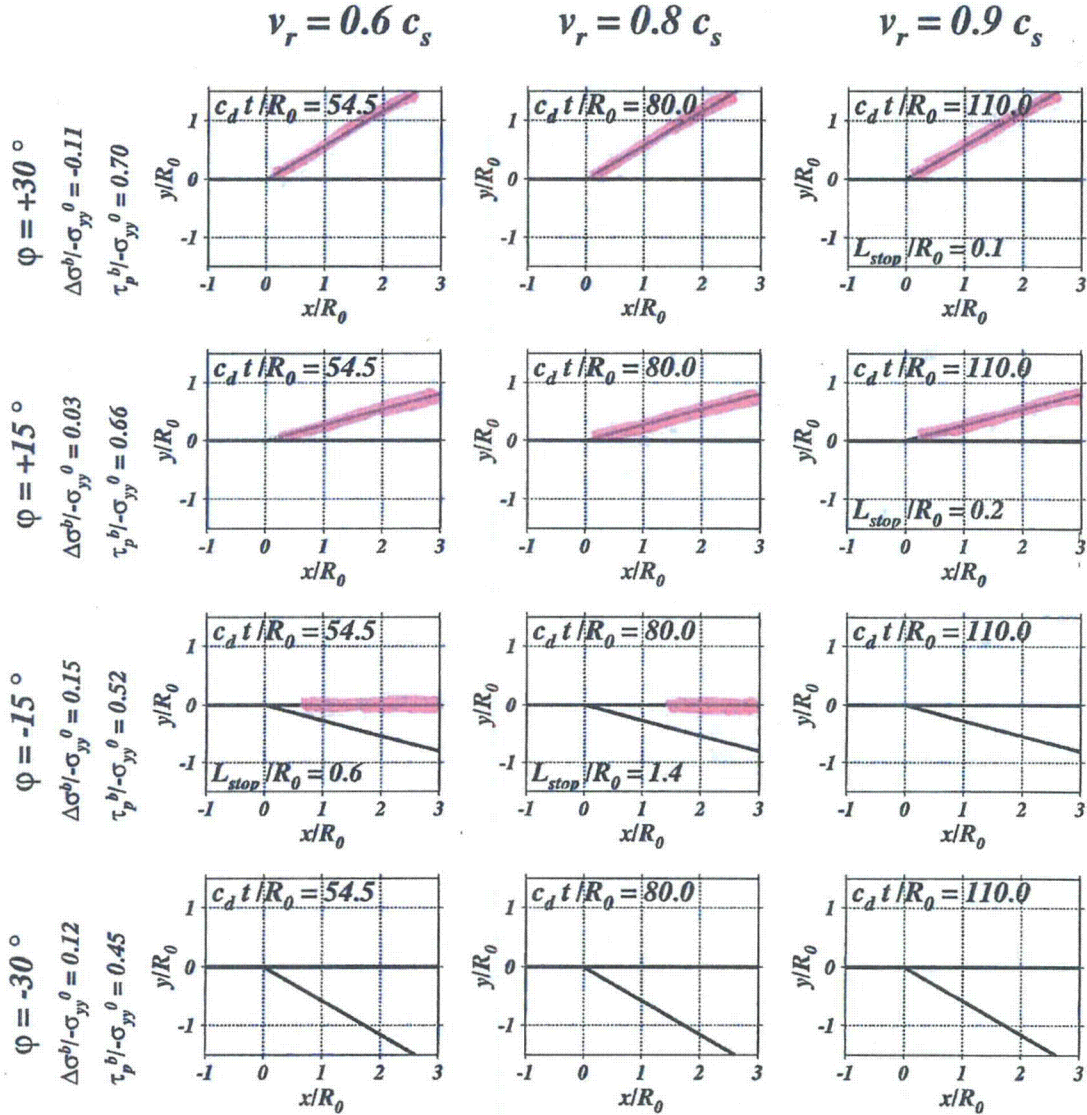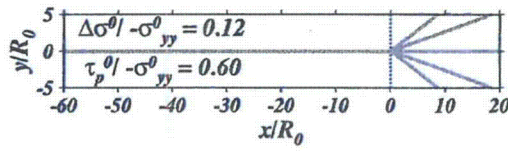**Figure 3.** Diagram of final rupture traces in the vicinity of the intersection for cases with high inclination of Smax, $\Psi = 56°$. L_{stop} indicates the length of arrested rupture once dynamically nucleated; those are given in terms of the slip-weakening zone size R_o for low-speed rupture along the main fault. Inhibition of fault rupture is shown by the pink highlighting. Source: Kame et al., 2003.
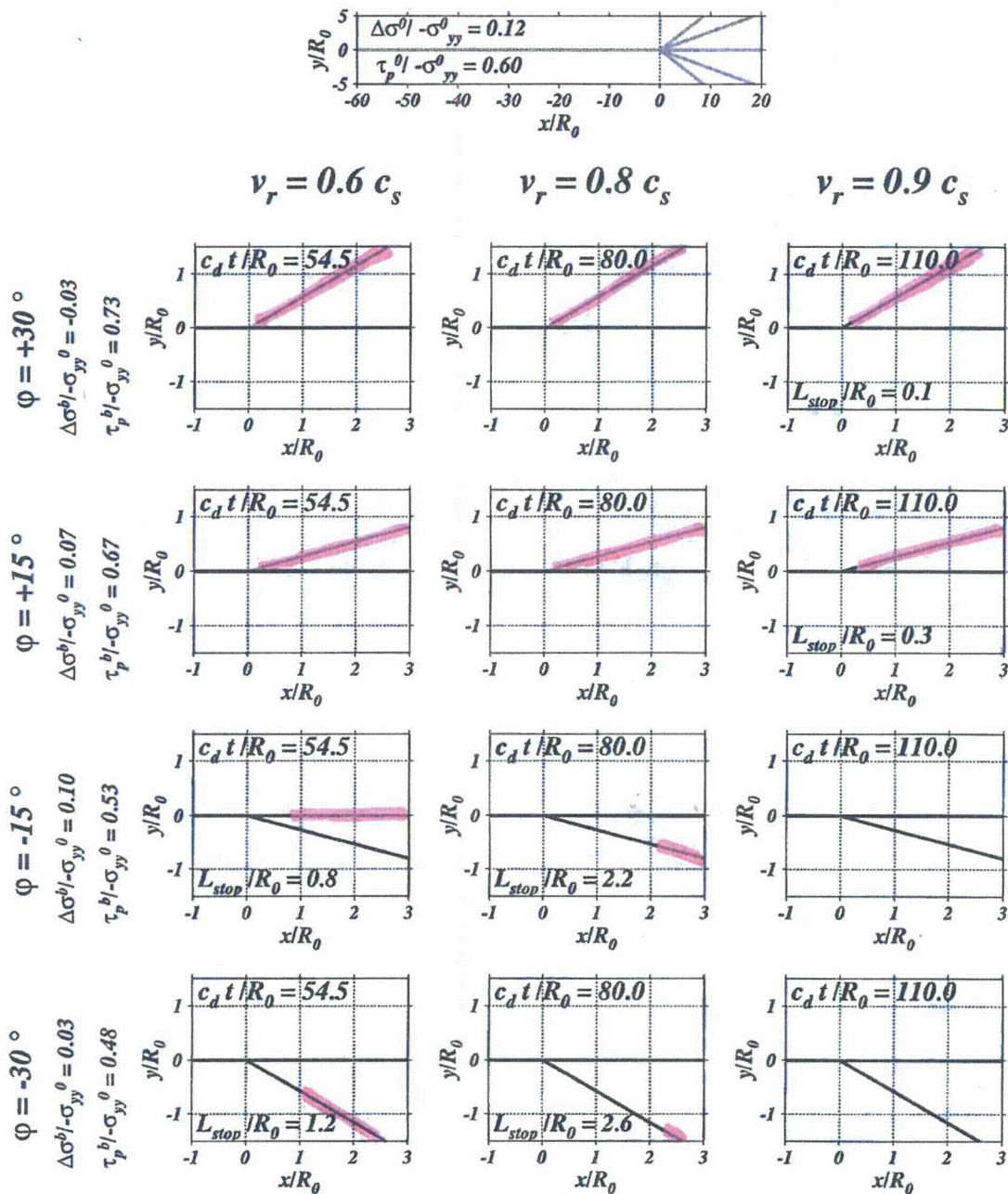
Figure 4. Diagram of final rupture traces in the vicinity of the intersection for cases with intermediate inclination of Smax, Ψ = 45°. L$_{stop}$ indicates the length of arrested rupture once dynamically nucleated; those are given in terms of the slip-weakening zone size R$_o$ for low-speed rupture along the main fault. Inhibition of fault rupture is shown by the pink highlighting. Source: Kame et al., 2003.
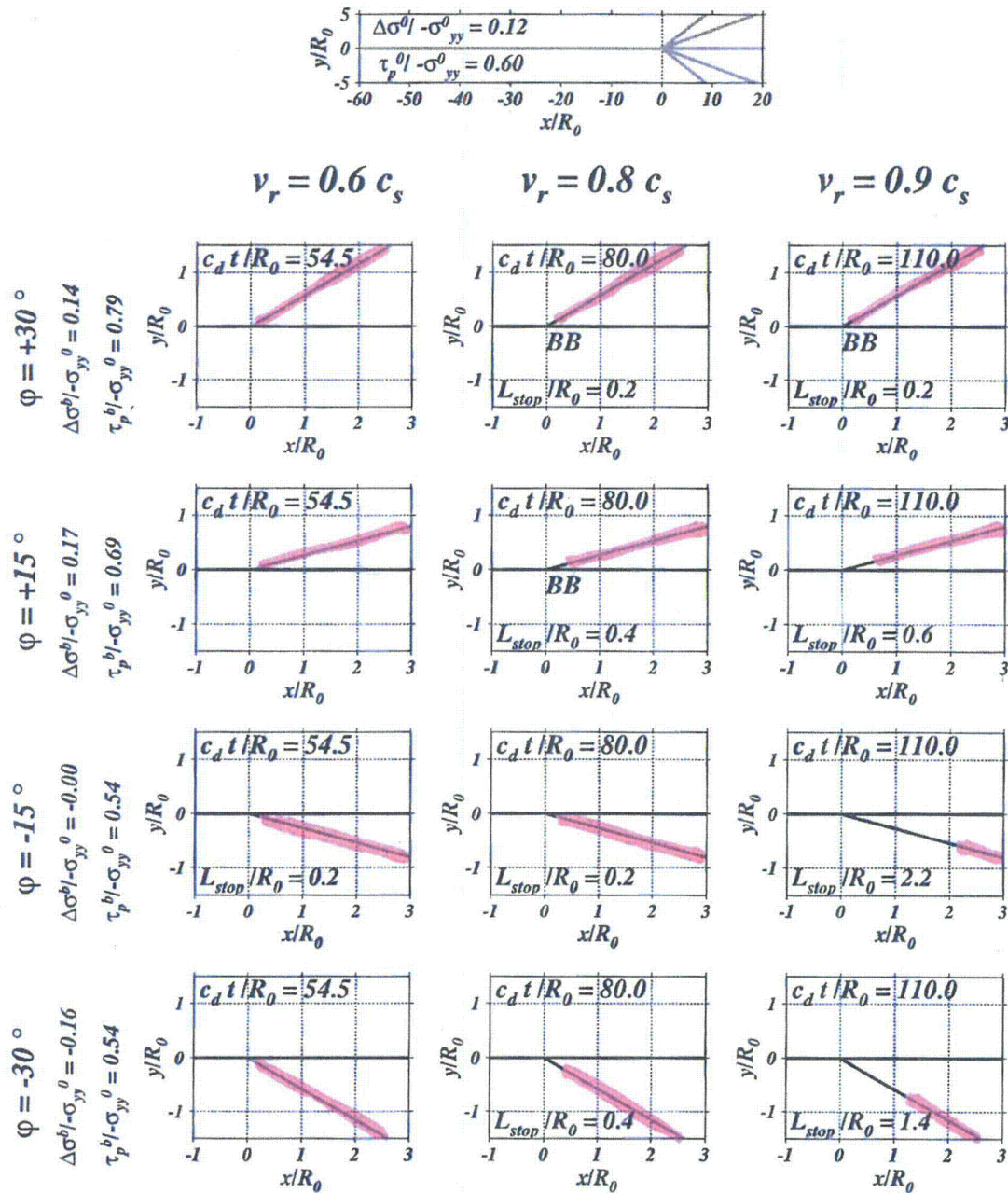
Figure 5. Diagram of final rupture traces in the vicinity of the intersection for cases with intermediately low inclination of Smax, Ψ = 25°. L$_{stop}$ indicates the length of arrested rupture once dynamically nucleated; those are given in terms of the slip-weakening zone size R$_o$ for low-speed rupture along the main fault. Inhibition of fault rupture is shown by the pink highlighting. Source: Kame et al., 2003.

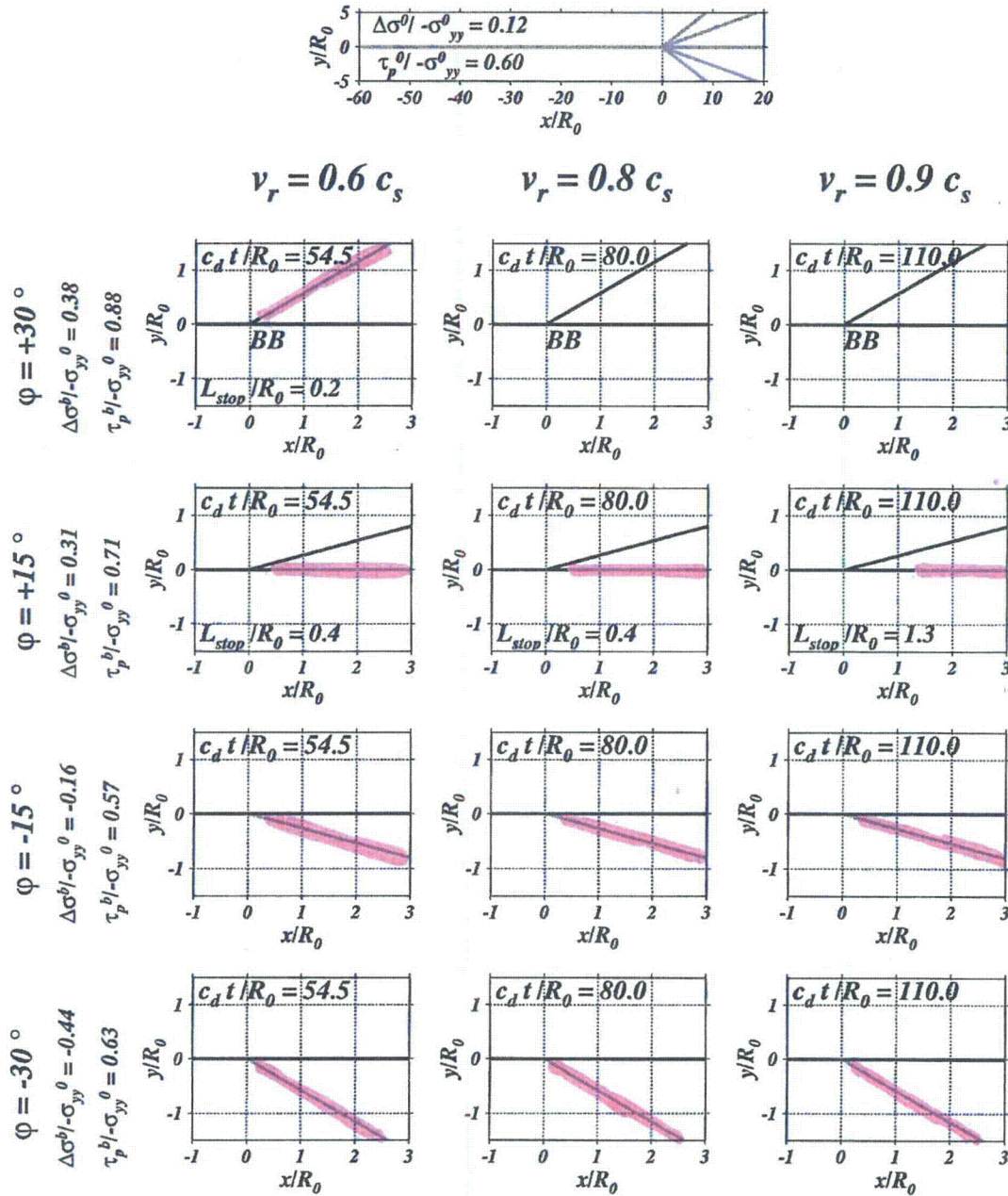**Figure 6.** Diagram of final rupture traces in the vicinity of the intersection for cases with low inclination of Smax, $\Psi = 13°$. L_{stop} indicates the length of arrested rupture once dynamically nucleated; those are given in terms of the slip-weakening zone size R_o for low-speed rupture along the main fault. Inhibition of fault rupture is shown by the pink highlighting. Source: Kame et al., 2003.

List of Fault Ruptures on Branched Faults

Wesnousky (2006; 2008) compiled information on the geometrical characteristics of a set of 37 earthquake surface rupture events, including 22 strike-slip events listed in Appendix 1. The main focus of these studies is on geometrical irregularities and their relationship to the termination of rupture. The focus of his studies was on stepovers, not on fault branching. The annotation of his fault maps states that adjacent and continuing traces of active faults that did not rupture during the earthquake are shown as dotted lines. However, this does not appear to consistently be the case, for example in the 1990 Luzon earthquake discussed further below. This limits the usefulness of his data compilation for the assessment of branch faulting in our study.

From the list of 22 strike-slip events in Appendix 1, we have selected six events involving rupture on branched faults, listed in Table 1. Bold fault names indicate that rupture proceeded on that fault past the branch point. All three possible modes of fault branching behavior are represented in these cases.

Mode 1. In three cases, including the 1979 Imperial Valley, 1995 Kobe, and 1992 Landers earthquakes, such rupture occurred on both the main fault and the branch fault (for the Kobe earthquake, the Gosukebashi segment represents the continuation of the Suwayama main fault segment).

Mode 2. In the 1990 Luzon and 2002 Denali earthquakes, rupture proceeded onto the branch fault but stopped on the main fault at the branch point.

Mode 3. In the 2001 Kokoxili (Kunlunshan) earthquake, the main fault continued to rupture without branching onto the Kitadan fault.

The mode 3 case is of most interest to Diablo Canyon, where we would like to know whether a southward rupture on the Hosgri fault would occur without branching onto the Shoreline fault.

Table 1. Earthquakes on branched faults

EVENT	MAIN FAULT	BRANCH FAULT	REFERENCE
1979 Imperial Valley	**Imperial**	**Brawley**	Kame et al., 2003
1990 Luzon	Philippine	**Digdig**	Rantucci, 1994
1995 Kobe	**Suwayama (Gosukebashi)**	**Okamoto**	Sekiguchi et al., 2000
1992 Landers	**Johnson**	**Kickapoo**	Kame et al., 2003
2001 Kokoxili (Kunlunshan)	**Kunlun**	Kitadan	Bhat et al., 2007
2002 Denali	Denali	**Totschunda**	Bhat et al., 2004

Comparison of Observations with Theoretical Models of Branch Faulting

1. 1979 Imperial Valley earthquake

Rupture in the 1979 Imperial Valley earthquake branched at the junction of the Imperial and Brawley faults, and surface and subsurface rupture proceed on both faults (Archuleta et al., 1984), as shown in Figure 7. The approximate S_{max} direction is poorly constrained but may be estimated to be approximately north-south, based on stress directions reported by Hardebeck and Hauksson (1999) along a profile somewhat to the northwest near the Salton Sea. That leads to $\Psi = 37°$ with the main fault (the Imperial fault), where it branched, on the extensional side, at approximately $\varphi = -34°$ onto the Brawley fault. This case corresponds to the results shown in Figure 4, last row, where the simulations show that progression of rupture on both the main fault as well as the branch is expected for all values of rupture velocity, and is enhanced by high values of rupture velocity. The model prediction is consistent with the observation that rupture continued on the main fault as well as branching onto the Brawley fault.
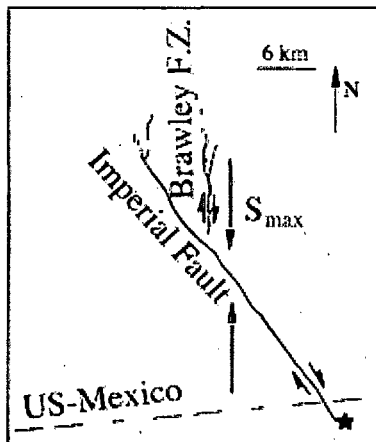

Figure 7. Fault geometry and maximum stress orientation, 1979 Imperial Valley earthquake. Source: Kame et al. (2003).

2. 1990 Luzon Earthquake

A location map of faults in Luzon is shown in Figure 8, and a rupture map of the 1990 Luzon earthquake is shown in Figure 9 (Rantucci, 1994). Rupture propagated northward on the Philippine fault and branched off that fault onto the Digdig fault near Rizal. The approximate S_{max} direction is poorly constrained in this region. Seno (1993) gives a value of about 300°, consistent with the overall relative direction of about 294° shown by Bird (2003), but measurements shown by Bird et al. (2003) on Luzon vary from 325° in southeastern Luzon to 294° in northwestern Luzon. Assuming a value of 294°, and a strike of 310° for the Philippine fault, we obtain $\Psi = 16°$. The Digdig fault branches from the Philippine fault at an angle $\varphi = +15°$ (the Philippine fault is a left-lateral fault, so the Dig-dig fault is on the compressional side). This case corresponds to the results shown in Figure 6, second row from the top, where the simulations show that progression of rupture only on the branch is expected for values of rupture velocity of $0.6c_s$ and $0.8c_s$. For these conditions, the model prediction is consistent with the observation that rupture branched onto the Digdig fault without continuing on the Philippine fault. For a rupture

velocity of $0.9c_s$, there is weak tendency for rupture to also propagate on the main fault. If the direction of is Ψ as much as 25°, which is within its range of uncertainty, then the Kame et al. (2003) model would predict rupture to continue on the Philippine fault without branching onto the Digdig fault.

The locations of previous earthquakes on the Philippine fault are shown in Figure 9. The segment of the Philippine fault south of Rizal broken by the 1990 earthquake previously broke in 1645, whereas segments of the Philippine fault north of Rizal, which did not break in 1990, previously ruptured more recently, in 1796 and 1892 earthquakes. This suggests that branching off the Philippine fault onto the Digdig fault in the 1990 earthquake may also have been influenced by the preexisting stress state on the Philippine fault.
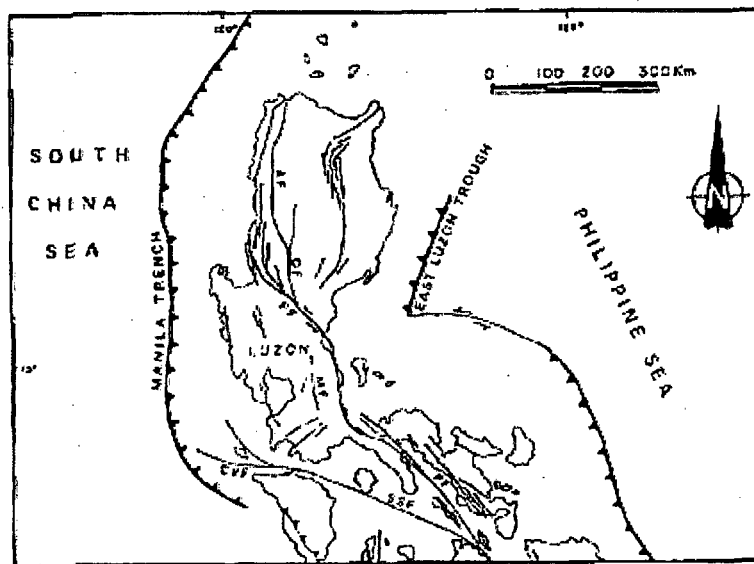

Fig. 8 *Major tectonic lineaments in Luzon (PF = Philippine Fault, DF = Digdig Fault, AF = Abra Fault, MF = Manila Fault), from Punongbayan and Umbal (1990).*

Figure 8. Location map of the 1990 Luzon earthquake. Rupture propagated northward on the Philippine fault (PF) and branched onto the Digdig fault (DF). Source: Rantucci (1994).
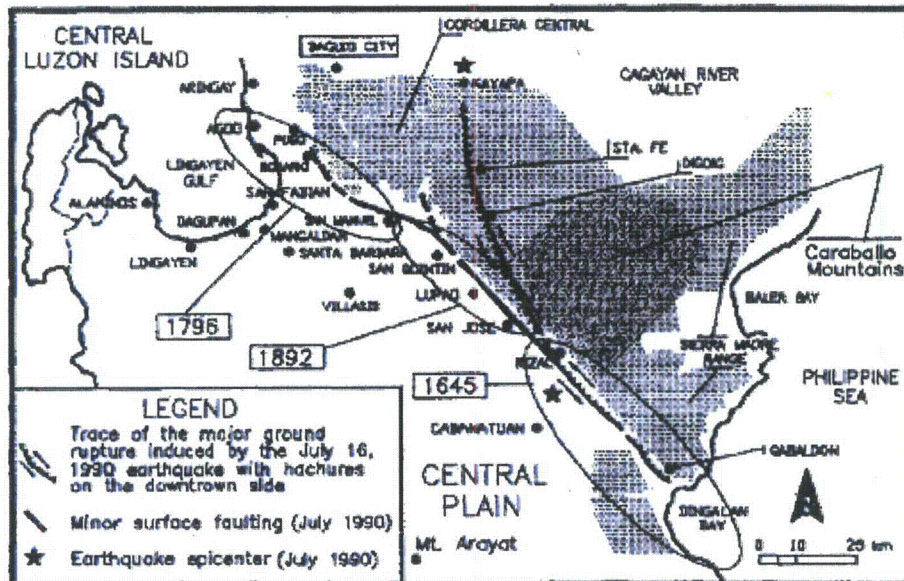
Fig. 4.9 – *Location of the Major Ground Rupture and minor surface faultings in Central Luzon associated with the July 1990 earthquake and the areas affected by the 1645, 1796, 1892 earthquakes.*

Figure 9. Rupture map of the 1990 Luzon earthquake. Rupture propagated northward on the Philippine fault and branched off that fault onto the Digdig fault near Rizal. The locations of the 1645, 1796 and 1892 earthquakes are also shown. Source: Rantucci (1994).

3. 1995 Kobe earthquake

A fault model of the 1995 Kobe earthquake was developed by Sekuguchi et al. (2000), shown in Figures 10 and 11. The fault model is divided into four main segments, A, B, C, and D (respectively corresponding to the Nojima, Suma, Suwayama, and Gosukebashi faults), and a branch segment, E, corresponding to the Okamoto fault. Of these five fault segments, only the Nojima fault (on Nojima Island) had surface faulting. Rupture of the remaining segments is inferred from aftershock locations, geodetic data, and the constraints on the location of the intersection of the causative fault planes and the earth surface in the Kobe City area obtained by Sekiguchi *et al.* (1996a, b). Sekiguchi et al. (2000) showed that inclusion of rupture on the branching Okamoto fault provided an improved fit to seismological and geodetic data.
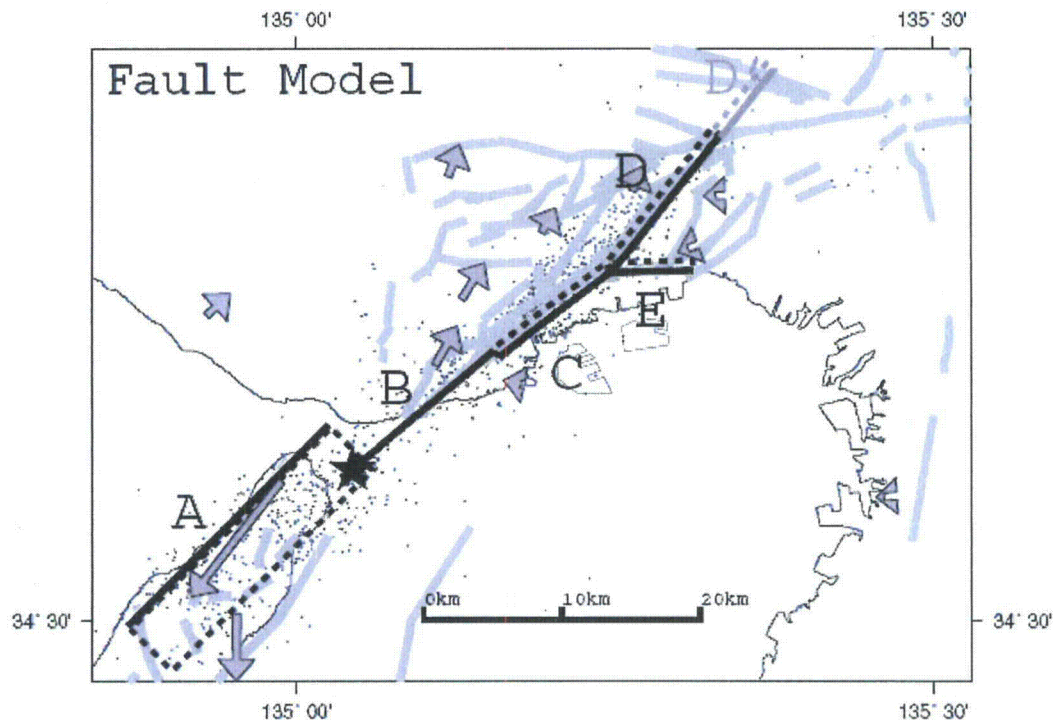
Figure 10. Fault-plane model (with segments A, B, C, D, and E). Black and gray lines show the active-fault traces reported by Ishihara *et al.* (1991). The black lines are those estimated to be causative faults. Vectors show static displacements during 1984 and 1995 after the earthquake, as determined by Hashimoto et al. (1996) from GPS data. Epicenters of the mainshock and aftershocks during the day of the mainshock are those determined by Nemoto et al. (1996, 1997). Dots are epicenters of aftershocks that occurred within 18 hours after the mainshock. Source: Sekiguchi et al., 2000.
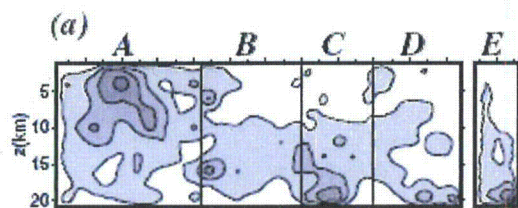

Figure 11. Final moment release distribution for the fault model with segments A, B, C, D, and E. Source: Sekiguchi et al., 2000.

The fault geometry of the branching fault is shown in Figure 10 (Sekiguchi et al., 1984). The approximate S_{max} direction is east-west, based on stress directions reported by Seno (2002). That leads to $\Psi = 37°$ with the main fault (taken as the Suwayama segment), where it branched on the extensional side onto the Okamoto fault. Measured with respect to the strike of the Suwayama fault, the branching angle φ is -35°, but measured with respect to the Gosukebashi fault, the branching angle $\varphi = -50°$. The change in strike of the main fault (between the Suwayama and Gosukebashi faults) at the fault branch is 35°. The model of Kame et al. (2003) assumes that the main fault is straight, so their calculations may not be completely applicable to the Kobe earthquake. This case

corresponds approximately to Figure 4, last row, where the simulations show that progression of rupture on both the main fault as well as the branch is expected for all values of rupture velocity, and is enhanced by high values of rupture velocity. The model prediction is consistent with the inference by Sekiguchi et al. (2000) that rupture branched onto the Okamoto fault as well as continuing on the Gosukebashi fault.

4. 1992 Landers earthquake

The fault geometry of the Landers earthquake, based on Sowers et al. (1994), is shown in Figure 12. S_{max} is taken from stress orientations in the Landers region determined by Hardebeck and Haukkson (2001) to be at approximately $\Psi = 60°$ with the trace of the Johnson Valley fault where it branched to the extensional side onto the Kickapoo fault, with the angle $\varphi = -30°$. The rupture also continued a few kilometers on the main (Johnson Valley) fault. This case corresponds to the results shown in Figure 3, last row, where the simulations show that progression of rupture on both the main fault as well as the branch is expected for all values of rupture velocity. The model prediction is consistent with the observation that rupture continued on the main fault as well as branching onto the Kickapoo fault.

Rupture died out on the Johnson Valley Fault a short distance after branching, which remains unexplained by the model. However, Kame et al. (2003) cited King et al.'s (1994) finding that a region of negative stress change occurs on the northwest continuation of the Johnson Valley Fault. The dynamic rupture was arrested shortly after propagating into that region of negative stress change. The negative stress changes are modest, of the order of 0.1 MPa, but may be related to why the rupture arrested.
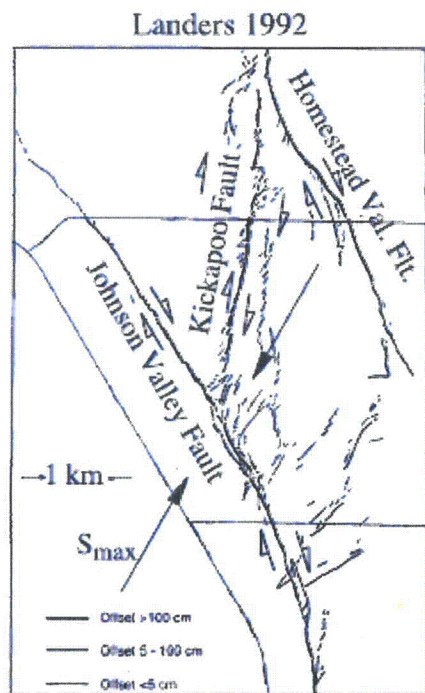

Figure 12. Fault geometry and maximum stress orientation, 1992 Landers earthquake. Source: Kame et al. (2003).

5. 2001 Kokoxili (Kunlunshan) Earthquake

Rupture propagated eastward on the Kunlun fault past its junction with the Kitadan fault, without branching onto the Kitadan fault (Xu et al., 2002; Bhat et al., 2007; Figure 13). The stepover of a few km between the Kunlun and Kitadan fault is considered to be insufficient to have hindered branching. The maximum compression direction Ψ with respect to the strike of the Kunlun fault near the junction was estimated by Bhat et al. (2007) to range from approximately $30°$ to $45°$. The branching angle of the Kitadan fault is $\varphi = -10°$. This case corresponds to Figure 4 or 5, third row from top. In Figure 5, for $\Psi = 25°$, rupture on the branch fault is inhibited for $Vr = 0.6c_s$ and $0.8c_s$, and partly inhibited for $Vr = 0.9c_s$. In Figure 4, for $\Psi = 45°$, rupture on the branch is inhibited only for partly and only for $Vr = 0.8c_s$. The model prediction may be consistent with the observation that rupture continued on the main fault without branching onto the Kitadan fault. It is also possible that the rupture velocity was supershear at the fault branching point (Bouchon and Vallee, 2003). More information about this case is needed to obtain a definitive conclusion.
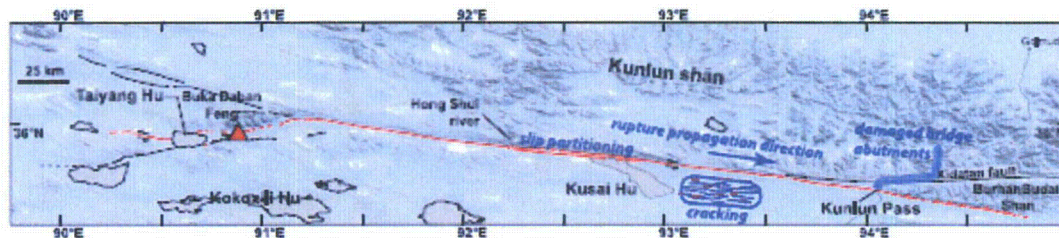

Figure 13. Simplified map of the surface rupture (red line) for the 2002 Kokoxili earthquake (adapted from Klinger et al. [2005]). Epicenter is indicated by a red triangle so that rupture propagated mainly to the east

6. 2002 Denali earthquake

Bhat et al. (2004) analyzed the observed dynamic slip transfer from the Denali to Totschunda faults during the Mw 7.9 3 November 2002 Denali fault earthquake, Alaska (Figure 14). They used 2D numerical simulations of the rupture processes in the vicinity of the branch junction. The angle Ψ between the maximum compression direction and the strike of the Denali fault near the junction was estimated to be $70°$ and $80°$ for their numerical simulations. The rupture velocity at branching is not well constrained but has been estimated to average about $0.8c_s$ throughout the event. They used values of $0.6c_s$ $0.8c_s$, $0.9c_s$ and $1.4\ c_s$ in their simulations. The assumed branching angle of the Totschunda fault was $\varphi = 15°$. Except for $70°$ and $0.9c_s$, all of their simulations predicted that the rupture path branches off the Denali fault onto the Totschunda fault. For all of these conditions, the model prediction is consistent with the observation that rupture branched onto the Totschunda fault without continuing on the Denali fault. For $70°$ and $0.9c_s$, rupture continued on the Denali fault as well as branching onto the Totschunda fault, but the rupture speed on the Denali fault was slower than that along the Totschunda fault and the slip was less.

The calculations of Kame et al. (2003) do not cover angles Ψ as large as $70°$ and $80°$. The Denali case corresponds most closely to the results for $\Psi = 54°$ shown in Figure 3,

third row from the top, where the simulations show that progression of rupture mainly on the branch is expected for values of rupture velocity of $0.6c_s$ and $0.8c_s$, with a weak tendency for rupture to propagate on the main fault. For these conditions, the model prediction is consistent with the observation that rupture branched onto the Totschunda fault without continuing on the Denali fault. For a rupture velocity of $0.9c_s$, there is weak tendency for rupture to also propagate on the main fault.
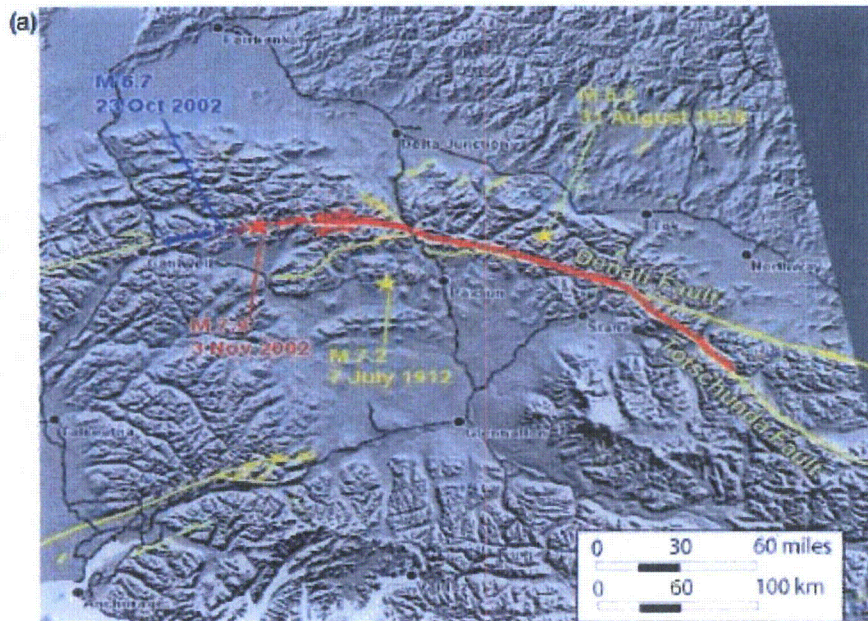

Figure 14. Rupture path, shown as a solid red line, of the *Mw* 7.9 Denali fault earthquake. The star near the western end of the rupture marks the epicenter. Source: Bhat et al. (2004).

Impacts of Fault Branching on Ground Motions

1. 1979 Imperial Valley Earthquake, Brawley Fault

Although the Brawley fault contributes only about 4% of the total seismic moment, it has a marked effect on the ground motion of nearby stations. Figure 15 shows the calculated contributions from the Brawley fault at stations of the El Centro array. At station E05, the 53° component was most affected, whereas the 323° component at E06 was most affected. This was explained as resulting from radiation pattern effects by Archuleta (1984). Figure 16 illustrates the contribution of the Brawley fault to the total motion at stations E06 and E07. The total synthetic seismogram is divided into the contributions from the Imperial fault and from the Brawley fault. The Brawley fault made a large contribution to the peak velocity on the 323° component at E06, and to the 53° component at E05 (not shown in Figure 16, but indicated in Figure 15).
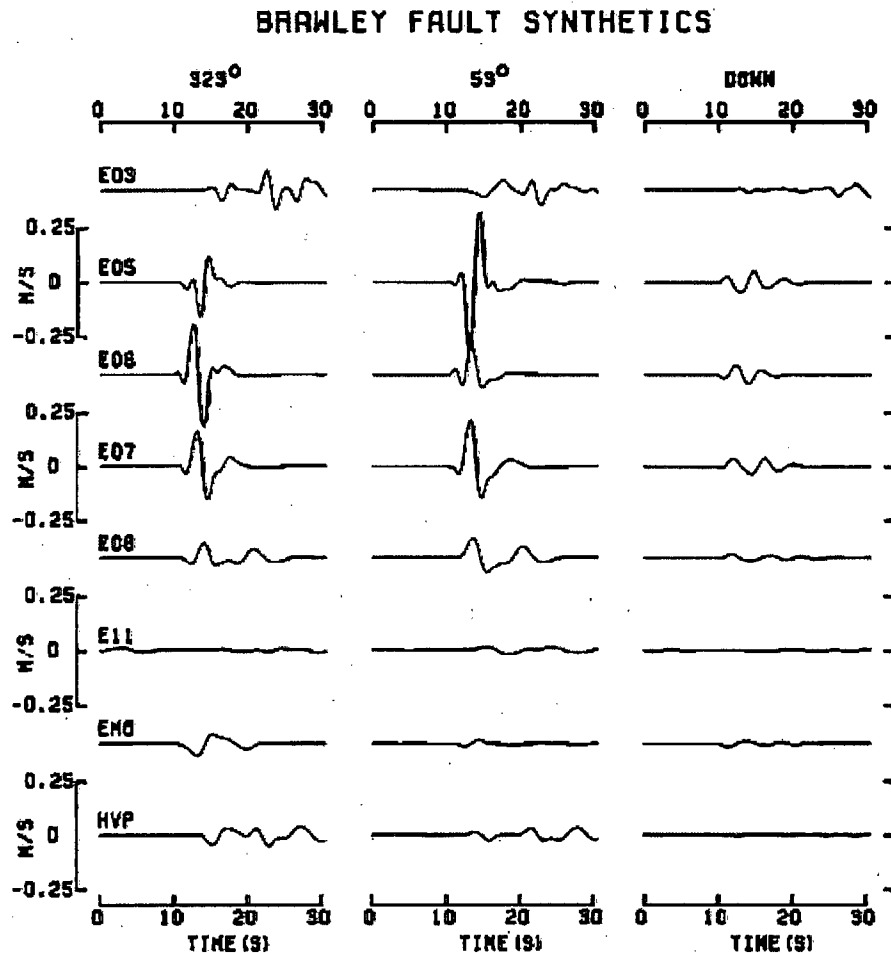

Figure 15. Calculated contributions of the Brawley fault to the ground velocity recorded at strong motion recording stations of the El Centro array. Source: Archuleta (1984).
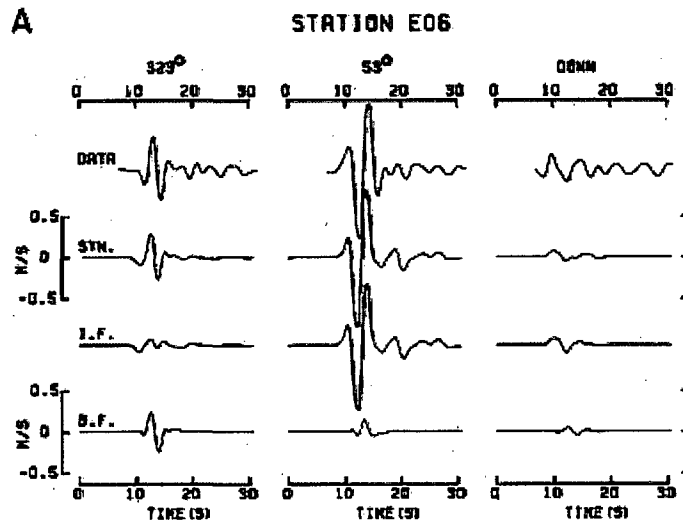
A   STATION E06

Figure 16. Calculated contributions of the Brawley and Imperial faults to the ground velocity recorded at station E06. Source: Archuleta (1984).

2. Kobe Earthquake – Okamoto fault

Sekiguchi et al. (2000) simulated the near-source ground motion using 3-D FDM (Pitarka et al., 1998) to estimate the effect of slip on the Okamoto fault on the ground motions, based on Iwata et al. (1999). The slip on the Okamoto fault affected the ground motion in the eastern part of Kobe (Nada and Higashi-Nada wards), Ashiya, and Nishinomiya cities, but its contribution was not dominant, even in those regions, constituting about 30 to 50% of the maximum velocity at 0.1 to 1.0 Hz. Figure 17 shows the contribution of the Okamoto fault (segment E) to the total synthetic ground velocities at station KBU. The contribution is about 30% on the North component, and very small on the east component. The contributions of each fault segment to the calculated peak velocity throughout the region is shown in Figure 18.
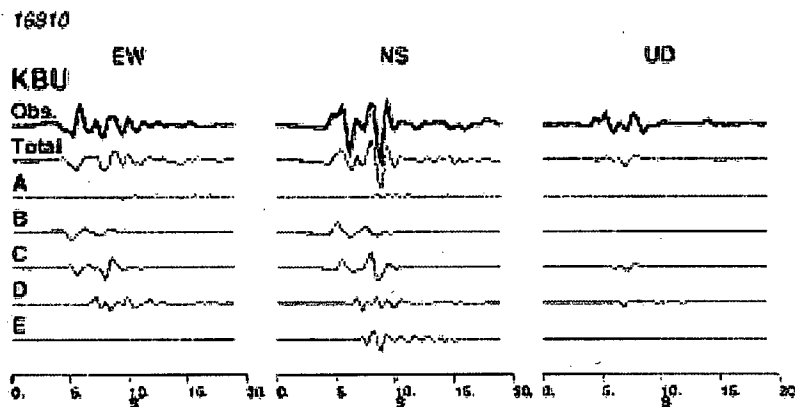

Figure 17. Observed (bold line) and synthetic (thin line) waveforms at KBU station. From the top: observed, synthetics for all 5 segments (ABCDE), and synthetics from segments A, B, C, D, and E (Okamoto segment). Source: Sekiguchi et al. (2000).
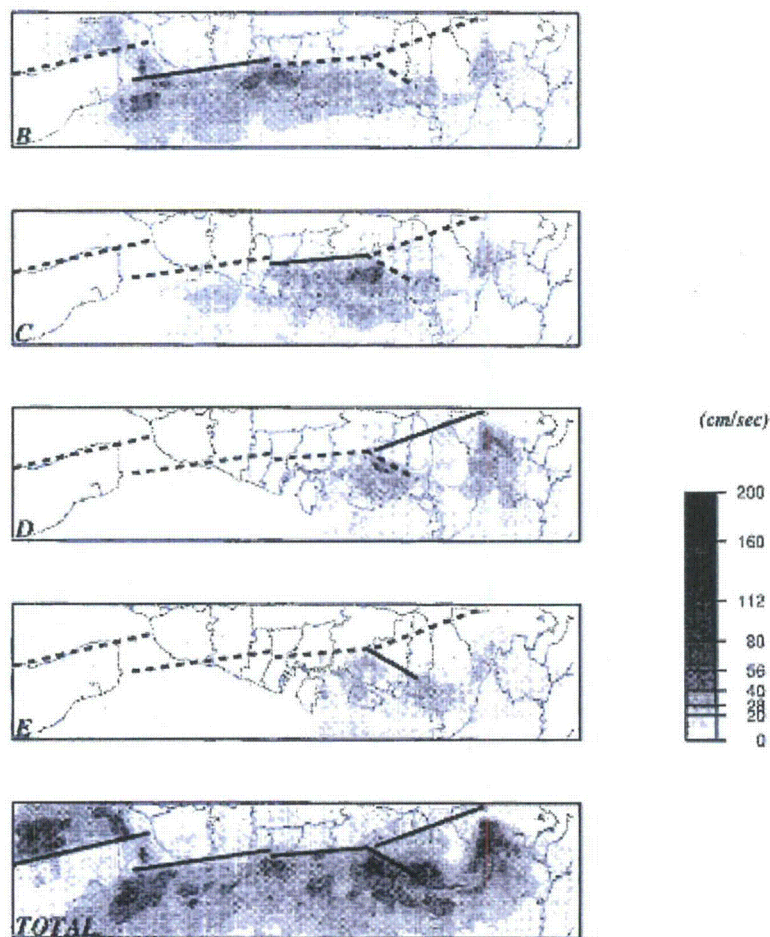
Max. Horizontal Vel. Distribution (0.1-1.0 Hz)

Figure 18. Distribution of the maximum horizontal velocity from each segment of the source. From top to bottom: distributions of maximum horizontal velocity caused by slip on Segments B, C, D, and E (Okamoto segment) and on the entire source. Source: Sekiguchi et al. (2000).

Conclusions

We have analyzed six events involving rupture on branched faults which represent three possible modes of fault branching behavior. In three cases, including the 1979 Imperial Valley, 1995 Kobe, and 1992 Landers earthquakes, such rupture occurred on both the main fault and the branch fault. In all three of these cases, the observations are consistent with the Kame et al. (2003) model. In the 1990 Luzon and 2002 Denali earthquakes, rupture proceeded onto the branch fault but stopped on the main fault at the branch point. The Denali earthquake observations are consistent with the Kame et al. (2003) model, and the Luzon earthquake observations are also potentially consistent, but the uncertainty in the stress field orientation renders this inconclusive with current data.

In the 2001 Kokoxili (Kunlunshan) earthquake, the main fault continued to rupture without branching onto the Kitadan fault. The Kokoxili earthquake observations are potentially consistent with the Kame et al. (2003) model, but the uncertainty in the stress field orientation renders this inconclusive with current data. The Kokoxili earthquake is the only case of the six that is directly relevant to the Hosgri – Shoreline branch, where we expect that rupture will continue on the main fault and be inhibited on the branch fault.

In the cases of the Imperial Valley and Kobe earthquakes, the contribution of the branch fault to the ground motions of the earthquake as a whole appear to have been locally fairly large, up to about one-half the overall ground motion level.

References

Ando, R., B.E. Shaw and C.H. Scholz (2009). Quantifying natural fault geometry: statistics of splay fault angles. *Bull. Seism. Soc. Am.*, 99, 389-395.

Archuleta, R.J. (1984). A faulting model for the 1979 Imperial Valley earthquake, *J. Geoph. Res.*, 89, 4559-4585.

Bhat, H.S., R. Dmowska, G.C.P. King, Y. Klinger, and J.R. Rice (2007). Off-fault damage patterns due to supershear ruptures with application to the 2001 M_w 8.1 Kokoxili (Kunlun) Tibet earthquake, *J. Geoph. Res.*, 112, B06301, doi:10.1029/2006JB004425.

Bhat, H.S., R. Dmowska, J.R. Rice, and N. Kame (2004). Dynamic slip transfer from the Denali to Totschunda Faults, Alaska: testing theory for fault branching, *Bull. Seism. Soc. Am.*, 94(6B), S202-S213.

Bhat, H.S., M. Olives, R. Dmowska, and J.R. Rice (2007). Role of fault branches in earthquake rupture dynamics, *J. Geoph. Res.*, 112, B11309, doi:10.1029/2007JB005027.

Bird, P. (2003) An updated digital model of plate boundaries, *Geochemistry Geophysics Geosystems*, 4(3), 1027, doi:10.1029/2001GC000252.

Bouchon, M. and M. Vallee (2003). Observation of long supershear rupture during the magnitude 8.1 Kunlunshan earthquake. Science 301, 824-826.

Fliss, S., H.S. Bhat, R. Dmowska, and J.R. Rice (2005). Fault branching and rupture directivity, *J. Geoph. Res.*, 110, B06312, doi:10.1029/2004JB003368.

Hardebeck, J. L., and E. Hauksson, Crustal stress field in southern California and its implications for fault mechanics, J. Geophys. Res., 106, 21,859–21,882, 2001.

Hardebeck, J. L., and E. Hauksson, Role of fluids in faulting inferred from stress field signatures, Science, 285, 236– 239, 1999.

Iwata, T., H. Sekiguchi, A. Pitarka, and K. Irikura (1999). Ground motion simulations in the Kobe area during the 1995 Hyogoken-Nanbu earthquake, in *The Effects of Surface Geology on Seismic Motion,* Irikura K., K. Kudo, H. Okada, and T. Sasatani (Editors), Vol. 3, BALKEMA, Rotterdam, 1295–1310.

Kame, N., J.R. Rice and R. Dmowska (2003). Effects of prestress state and rupture velocity on dynamic fault branching. J. Geophys. Res. 108, ESE 13-1 – 13-21.

McLaren, M.K. and W.U. Savage (2001). Seismicity of south-central coastal California: October 1987 through January 1997. *Bull. Seism. Soc. Am.*, 91(6), 1629-1658

Pitarka, A., K. Irikura, T. Iwata, and H. Sekiguchi (1998). Three-dimensional simulation of the near-fault ground motion for the 1995 Hyogoken Nanbu (Kobe), Japan, earthquake, *Bull. Seism. Soc. Am.* **88,** 428– 440.

Poliakov, A. N. B., R. Dmowska, and J. R. Rice, Dynamic shear rupture interactions with fault bends and off-axis secondary faulting, J. Geophys.Res., 107(B11), 2295, oi:10.1029/2001JB000572, 2002.

Rantucci, Giovanni (1994). Geological disasters in the Philippines : The July 1990 earthquake and the June 1991 eruption of Mount Pinatubo. Rome, Italy.

Sekiguchi, H., K. Irikura, and T. Iwata (2000). Fault geometry at the rupture termination of the 1995 Hyogo-ken Nanbu earthquake, *Bull. Seism. Soc. Am.*, 90(1), 117-133.

Seno, T. (2002). Synthesis of the regional stress fields of the Japanese islands. *Island Arc*, 8, 66-79.

Seno, T., S. Stein and A. Gripp (1993). A model for the motion of the Philippine Sea Plate consistent with NUVEL-1 and Geological data. J. Geophys. Res. 98, 17,941-17,948.

Sowers, J.M., J.R. Unruh, W.R. Lettis, and T.D. Rubin (1994). Relationship of the Kickapoo fault to the Johnson Valley and Homestead Valley faults, San Bernardino County, California, *Bull. Seism. Soc. Am.*, 84, 528-536.

Thio, H.K. (1995). Source complexity of large strike-slip earthquakes. PhD Thesis, Caltech.

Wesnousky, S.G. (2008). Displacement and geometrical characteristics of earthquake surface ruptures: issues and implications for seismic-hazard analysis and the process of earthquake rupture, *Bull. Seism. Soc. Am.*, 98(4), 1609-1632, doi:10.1785/0120070111.

Wesnousky, S.G. (2006). Predicting the endpoints of earthquake ruptures. Nature 444, 358-360, doi:10.1038.

Xu Xiwei Xu,1 Guihua Yu,1 Y. Klinger,2 Paul Tapponnier,2 and Jerome Van Der Woerd (2006). Reevaluation of surface rupture parameters and faulting segmentation of the 2001 Kunlunshan earthquake (Mw7.8), northern Tibetan Plateau, China. J. Geophysical Research, 11, B05316, doi:10.1029/2004JB003488.

APPENDIX 1. FAULT RUPTURE MAPS OF LARGE STRIKE-SLIP EARTHQUAKES

Source: Wesnousky (2006)

No.	Date	Location	Type	Length (km)	M_w	Ref
1	1857-Jan-9	San Andreas, CA	ssr	360	7.9	1
2	1891-Oct-28	Neo-Dani, JPN	ssl	80	7.3	2
3	1930-Nov-2	Kita-Izu, JPN	ssl	35	6.7	3
4	1939-Dec-25	Erzincan, TUR	ssr	300	7.7	4
5	1940-May-19	Imperial, CA	ssr	60	6.9	5
6	1942-Dec-20	Erbaa-Niksar, TUR	ssr	28	6.8	4
7	1943-Nov-26	Tosya, TUR	ssr	275	7.5	4
8	1943-Sep-10	Tottori, JPN	ssl	10.5	6.2	6
9	1944-Feb-01	Gerede-Bolu, TUR	ssr	135	7.3	4
10	1967-Jul-22	Mudurnu, TUR	ssr	60	6.9	4
11	1968-Apr-8	Borrego Mtn, CA	ssr	31	6.1	7
12	1979-Oct-15	Imperial, CA	ssr	36	6.2-6.4	8,9
13	1981-Jul-29	Sirch Iran	ss	64	6.2	10
14	1987-Nov-23	Superstition Hills, CA.	ssr	25	6.2-6.4	11
15	1990-Jul-16	Luzon, PHL	ssl	112	6.9	12,13
16	1992-Jun-28	Landers, CA	ssr	77	7.2	14
17	1998-Mar-14	Fandoqa, IRN	ssn	25	6.6	10
18	1999-Oct-16	Hector Mine, CA.	ssr	44	6.9	15
19	1999-Aug-17	Izmit, TUR	ssr	145	7.1	16
20	1999-Nov-12	Duzce, TUR	ssr	40	7.0	17
21	2001-Nov-14	Kunlun, China	ssl	421	7.8	18-20
22	2002-Nov-03	Denali, AK	ssr	302	7.6	21

References

1. Sieh, K. E. Slip along the San Andreas Fault associated with the great 1857 earthquake. Bulletin of the Seismological Society of America 68, 1421-1448 (1978).

2. Matsuda, T. Surface faults associated with Nobi (Mino-Owari) Earthquake of 1891, Japan. Bulletin of Earthquake Research Institute, University of Tokyo 13, 127-162 (1974).

3. Matsuda, T. in Izu Peninsula (eds. Hoshino, M. & Aoki, H.) 73-102. (Tokai University Press, Tokyo, 1972).

4. Barka, A. Slip distribution along the North Anatolian Fault associated with the large earthquakes of the period 1939 to 1967. Bulletin of Seismological Society of America 86, 1238-1254 (1996).

5. Trifunac, M. D. & Brune, J. Complexity of energy release during the Imperial Valley, California, earthquake of 1940. Bulletin of Seismological Society of America 60, 137-160 (1970).

6. Kaneda, H. & Okada, A. Surface rupture associated with the 1943 Tottori earthquake: compilation of previous reports and its tectonic geomorphological implications. Active Fault Research 21, 73-91 (in Japanese with English Abstract) (2002).

7. Clark, M. M. (ed.) Surface rupture along the Coyote Creek fault, the Borrego Mountain Earthquake of April 9, 1968 (United States Geological Survey, 1972).

8. Johnson, C. E. & Hutton, L. K. Aftershocks and Preearthquake Seismicity in The Imperial Valley California, Earthquake of October 15, 1979. United States Geological Survey Professional Paper 1254, 59-76 (1982).

9. Sharp, R. et al. Surface faulting in the Central Imperial Valley in 'The Imperial Valley California, Earthquake of October 15, 1979. United States Geological Survey Professional Paper 1254 (1982).

10. Berberian, M. et al. The 1998 March 14 Fandoqa earthquake (Mw 6.6) in Kerman province, southeast Iran: re-rupture of the 1981 Sirch earthquake fault, triggering of slip on adjacent thrusts and the active tectonics of the Gowk fault zone. Geophy. J. Int. 146, 371-398 (2001).

11. Sharp, R. et al. Surface faulting along the Superstition Hills fault zone and nearby faults associated with the earthquakes of 24 November 1987. Bulletin of Seismological Society of America 79, 252-281 (1989).

12. Nakata, T. Surface faulting associated with the Philippine earthquake of 1990 (in Japanese). Journal of Geography 99, 95-112 (1990).

13. Yomogida, K. & Nakata, T. Large slip velocity of the surface ruptures associated with the 1990 Luzon earthquake. Geophysical Research Letters 21, 1799-1802 (1994).

14. Sieh, K. et al. Near-field investigations of the Landers earthquake sequence, April to July 1992. Science 260, 171-176 (1993).

15. Treiman, J., Kendrick, K. J., Bryant, W. A., Rockwell, T. K. & McGill, S. F. Primary surface rupture associated with the Mw 7.1 16 October 1999 Hector Mine earthquake, San Bernardino County, California. Bulletin of the Seismological Society of America 92, 1171-1191 (2002).

16. Barka, A. et al. The surface rupture and slip distribution of the 17 August 1999 Izmit Earthquake (M 7.4), North Anatolian Fault. Bulletin of Seismological Society of America 92, 43-60 (2002).

17. Akyuz, H. S. et al. Surface rupture and slip distribution of the 12 November 1999 Duzce Earthquake (M 7.1), North Anatolian Fault, Bolu, Turkey. Bulletin of Seismological Society of America 92, 61-66 (2002).

18. Klinger, Y. et al. High-resolution satellite imagery mapping of the surface rupture and slip distribution of the Mw ~7.8, 114 November 2001 Kokoxili earthquake, Kunlun fault, northern Tibet, China. Bulletin of the Seismological Society of America 95, 1970-1987 (2005).

19. Lin, A. et al. Co-seismic strike-slip and rupture length produced by the 2001 Ms 8.1 central Kunlun earthquake. Science 296, 2015-2017 (2002).

20. Xu, X., Chen, W., Ma, W., Yu, G. & Chen, G. Surface rupture of the Kunlunshan earthquake (Ms 8.1), northern Tibetan plateau, China. Seismological Research Letters 73, 884-892 (2002).

21. Haeussler, P. J. et al. Surface rupture and slip distribution of the Denali and Totschunda faults in the 3 November 2002 M7.9 earthquake, Alaska. Bulletin of the Seismological Society of America 94, S23-252 (2005).

Appendix K

Update of the Abrahamson (2000) Directivity Model for Strike-Slip Earthquakes

K-1 Introduction

Somerville et. al (1997) derived directivity scale factors based on the within-event residuals of Abrahamson and Silva (1997) model. To facilitate combining the residuals from different earthquakes, the directivity model used a normalized directivity parameter, X, given by the ratio of the length of the rupture toward the site, S, to the total rupture length, L, as shown in Figure K-1.

Somerville et al. (1999) used the following functional form for the directivity effect for the average horizontal component:

$$\ln(Dir\,Factor) = c_1 + c_2\,X\cos(\theta) \tag{K-1}$$

A short-coming of the Somerville et al. (1997) model is that is did not include saturation (with X) that was observed in numerical simulations conducted as part of the Bay Bridge hazard studies. Abrahamson (2000) developed an update to the Somerville et al. (1997) model that was set to include saturation effects constrained for M7.5 earthquakes for a spectral period of 3 seconds.

The Abrahamson (2000) model used the following functional form for the base directivity model:

$$\ln(Dir\,Factor) = \begin{cases} C_1(T) + 1.88\,C_2(T)X & for\,X \le 0.4 \\ C_1(T) + 1.88\,C_2(T)\,0.4 & for\,X > 0.4 \end{cases} \tag{K-2}$$

where $C_1(T)$ and $C_2(T)$ are the coefficients from the Somerville et al. (1999) model. In addition, Abrahamson (2000) introduced a magnitude-dependent and a distance-dependent taper to the directivity factor:

$$T_d(R_{rup}) = \begin{cases} 1 & for\,R_{rup} \le 30\,km \\ 1 - (R_{rup} - 30)/30 & for\,30 < R_{rup} < 60\,km \\ 0 & for\,R_{rup} \ge 60\,km \end{cases} \tag{K-3}$$

$$T_m(M) = \begin{cases} 1 & for\,M \ge 6.5 \\ 1 - (R_{rup} - 30)/30 & for\,6.0 < M < 6.5 \\ 0 & for\,M < 6.0 \end{cases} \tag{K-4}$$

While the Abrahamson (2000) model captured saturation effects, it did not work well for magnitudes that were not close to M7.5 or for periods not close to 3 seconds.

Recently, as part of the NGA project, a new directivity model was developed by Spudich and Chiou (2008) based on the residuals from Next Generation Attenuation Ground

Shoreline Fault Zone, Appendix K, Update of the Abrahamson (2000) Directivity Model for Strike-Slip Earthquakes

Motion Prediction Equations (NGA GMPEs). As part of the NGA project, this model was reviewed by the NGA developers in terms of its applicability to the NGA GMPEs. The Spudich and Chiou (2008) directivity model is more general in that it includes a radiation pattern term. An issue with this model is that it is not centered on zero for average directivity conditions, implying a change in the median ground motion for average directivity conditions. The NGA developers were unsure of the cause for this shift and how the models should be applied.

Watson-Lamprey (2007) evaluated the within-event residuals from the NGA GMPEs following the same approach as used by Somerville et al. (1999). She found that the directivity effect was about one-half as strong as in the Somerville et al. (1999) model. This was not consistent with the strong directivity effects given in the Spudich and Chiou (2008) model.

As a result, the NGA developers did not make a recommendation with regard to the applicability of the new directivity model to the NGA GMPEs. Rather, a follow-on project to further evaluate the directivity effect was recommended. This follow-on project began in 2010 and is scheduled to be completed in 2012. As part of this follow-on project, Abrahamson and Watson-Lamprey developed an update of the Abrahamson (2000) model based on numerical simulations conducted as part of the NGA project. This updated model is described in this appendix.

K-2. Numerical Simulations Conducted for the NGA Project

To support the NGA ground motion model developers, a large set of 1-D finite-fault kinematic simulations were run for magnitudes 6.5 to 8.2 for strike-slip earthquakes. The simulations were conducted by three modeling groups: URS, UNR, and Pacific Engineering and Analysis. Descriptions of the simulation methods used by these three groups are given in Somerville et al. (2005). The URS and UNR simulations for are the fault normal and fault parallel components and the PEA simulations are for the average horizontal component. In developing the directivity model, only the URS simulations are used.

K-2.1 Simulation Cases

The simulation cases are listed in Table K-1. The ground motions were computed for a minimum of 20 realizations of the source for each scenario. One realization of the source includes a slip distribution – hypocenter combination. For two ruptures (SC and SD), the minimum number of realizations was increased to 30 because the slip models for these two scenarios includes both deep and shallow ruptures to allow an evaluation of the effect of asperity depth. Shallow rupture is defined as having the center of at least one asperity at a depth of 5 km or less.

The hypocenters were constrained to be located in the upper half (positive Y values in Figures 1 and 2) of the rupture with no less than 6 distinct hypocenter locations. The depth distribution of the hypocenters includes both shallow and deep events.

The station locations for the strike-slip are shown in Figures K-2. The stations are located on just one side of the rupture due to symmetry for a vertical strike-slip fault.

Shoreline Fault Zone, Appendix K, Update of the Abrahamson (2000) Directivity Model for Strike-Slip Earthquakes

K-3 Residuals from Simulations

The finite-fault simulations lead to a large data set of simulated ground motions. For the evaluation of directivity effects, a regression analysis using a simplified model is conducted and the within-event residuals computed.

The directivity scaling from the residuals for T=3 sec for the M7.5 strike-slip scenario (SE) is shown in Figure K-3. The three simulation models show very different directivity effects: the UNR simulations show no directivity effects, the PEA simulations show some directivity effects, and the URS simulations show large directivity effects. The UNR and PEA simulations include randomness in the source that works well for on average, but tends to break up the directivity. Therefore, only the residuals from the URS model are used for this study.

The T=2 second residuals from the URS model are shown in Figures K-4a-d for magnitudes 6.5, 7.0, 7.5, and 7.8, respectively. These plots show that the directivity factor saturates at about 10 km for all four magnitudes. Similar plots of the T=5 seconds residuals are shown in Figures K-5a-d. For the longer period, the directivity factor saturates at about 40 km for all four magnitudes.

K-4 Directivity Model

The within-event residuals, were to the following functional form using ordinary least-squares:

$$\ln(DirFac) = [b_2(T)\, s\cos(\theta) - b_1(T)]\, T_1(R_{rup})\, T_2(M)$$

(K-5)

where M is the moment magnitude, R_{Rup} is the rupture distance, s and θ are the length and angle for segments of the rupture between the site and the hypocenter as described below.

The s and θ terms are computed from the geometry of the site, rupture, and hypocenter. First, the closest point on the rupture to the site is found. The surface projection of this point is called P_1. Next, move along the rupture segments toward the epicenter until either the length of the rupture reaches the saturation distance, s_0, or the epicenter is reached. This point is called P_2.

The s term is the length of rupture between points P_1 and P_2 measured along strike, not just the distance between P_1 and P_2; and θ is the angle between the line P_2-Site and P_1-P_2 (see Figures K-5 and K-6). The saturation distance, s_0, is given by

$$s_0 = MIN\big(c_1, 10 + 20(M - 6.0)\big)$$

(K-6)

Distance and magnitude tapers are applied to limit the directivity effect. The tapers are given by:

$$T_1(R_{rup}) = \begin{cases} 1 & \text{for } R_{rup} \leq 10km \\ (R_{rup}-10)/30 & \text{for } 10km < R_{rup} < 40km \\ 0 & \text{for } R_{rup} \geq 40km \end{cases}$$

(K-7)

$$T_2(M) = \begin{cases} 1 & \text{for } M \geq 6.5 \\ 2(M-6) & \text{for } 6.0 < M < 6.5 \\ 0 & \text{for } M \leq 6.0 \end{cases}$$

(K-8)

This model provides a good fit to the directivity effect seen in the URS residuals, but it has the same issue as seen in the Spudich and Chiou (2008) model: the mean of the model is not zero over uniformly distributed stations. If this model is applied to the NGA models, then in addition to capturing the directivity effects, there is a shift in the average ground motion.

The goal of this study is to develop directivity factors that can be applied to the NGA GMPEs without changing the median ground motion for average directivity conditions. To meet this goal, the directivity model derived from the simulation residuals was adjusted to remove the mean value for randomly located sites. The directivity model was applied to a uniform grid of sites within 40 km of the rupture, spaced 1 km apart and the mean of the model predictions was computed. The mean was then fit to the following functional form:

$$Mean = \left[\exp\!\left(a_1 + a_2(8.5-M)^2\right) + b_1 \right] T_1(R_{rup}) T_2(M)$$

(K-9)

The resulting directivity model, centered on zero, has the following form:

$$\ln(DirFac) = \left[b_2 \, s \cos(\theta) - \exp\!\left(a_1 + a_2(8.5-M)^2\right) \right] T_1(R_{rup}) T_2(M)$$

(K-10)

The coefficients of the model are listed in Table K-2.

The directivity model, given by equation K-10 is compared to the Somerville et al. (1999) and Abrahamson (2000) directivity models in for M6.5 earthquakes Figures K-7a-c for spectral periods of 1, 3, and 5 seconds, respectively. Similar plots are shown in Figures K-8a-c for M7.5 earthquakes for spectral periods of 1, 3, and 5 seconds, respectively. These figures show that the main difference between the new model and the Abrahamson (2000) model is that the saturation distance in the new model varies as a function of period.

The period dependence of the directivity models is compared in Figure K-9. This figure shows that the new model has a peak in the directivity effect as different periods depending on the magnitude. For the larger magnitude earthquakes the peak in the directivity factor is at longer periods than for moderate magnitudes.

REFERENCES

Abrahamson, N. A. (2000). Effects of rupture directivity on probabilistic seismic hazard analysis, Proc Microzonation Conference, Palm Springs.

Hanks, T. C. and W. H. Bakun (2002). A bilinear source-scaling model for M0log A observations of continental earthquakes, Bull. Seism. Soc. Am., 92, 1841-1846.

Spudich, P., and N. Chiou (2008). Directivity in NGA ground motions: Analysis using isochrone theory, *Earthq. Spectra* **24**, no. 1, 299-318.

Somerville, P. G., N. F. Smith, R. W. Graves. and N. A. Abrahamson (1997). Modification of empirical strong ground motion attenuation relations to include the amplitude and duration effects of rupture directivity, Seism. Res. Let, Vol. 68, 199-222.

Watson-Lamprey, J. (2007). In search of directivity, Seism. Soc. Am. Annual Meeting, (Abstract)

Wells, D. and K. Coppersmith (1994). Updated empirical relationships among magnitude, rupture length, rupture area, and surface displacement, Bull Seism. Soc. Am., Vol. 84, 974-1002.

Table K-1. Sources for Strike-Slip Simulations

Event Name	Mag	Area (km²)	W (km)	L (km)	Dip	Top of Rupture (km)
SA	6.5	325	13	25	90	0
SB	6.5	480	15	32	90	0
SC	6.5	210	10	21	90	0
SD	7.0	1005	15	67	90	0
SE	7.5	3150	15	210	90	0
SF	7.5	4800	15	320	90	0
SG	7.5	2100	15	140	90	0
SH	7.8	6300	15	420	90	0
SI	7.8	3525	15	235	90	0
SJ	8.2	7050	15	470	90	0

Table K-2. Directivity Model Coefficients for Strike-Slip Earthquakes

Period (sec)	c_1 (km)	b_2 (1/km)	a_1	a_2
1	10	0.018	-2.07	-0.061
2	20	0.041	-0.27	-0.201
3	30	0.044	0.32	-0.303
4	40	0.037	0.43	-0.371
5	50	0.034	0.42	-0.391
7	50	0.028	0.22	-0.380
10	50	0.023	0.04	-0.392
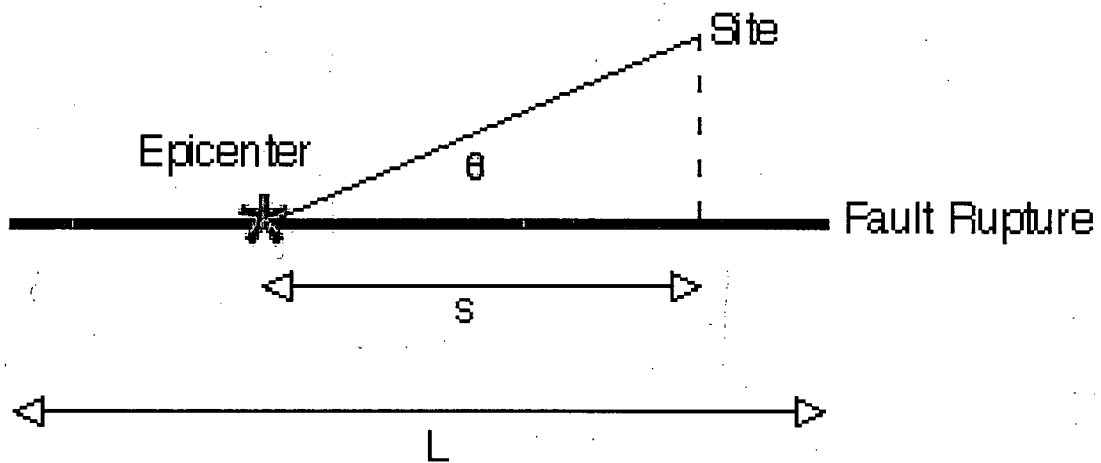
$$X = s/L$$

Figure K-1. Directivity parameters for strike-slip earthquakes used by the Somerville et al. (1999).
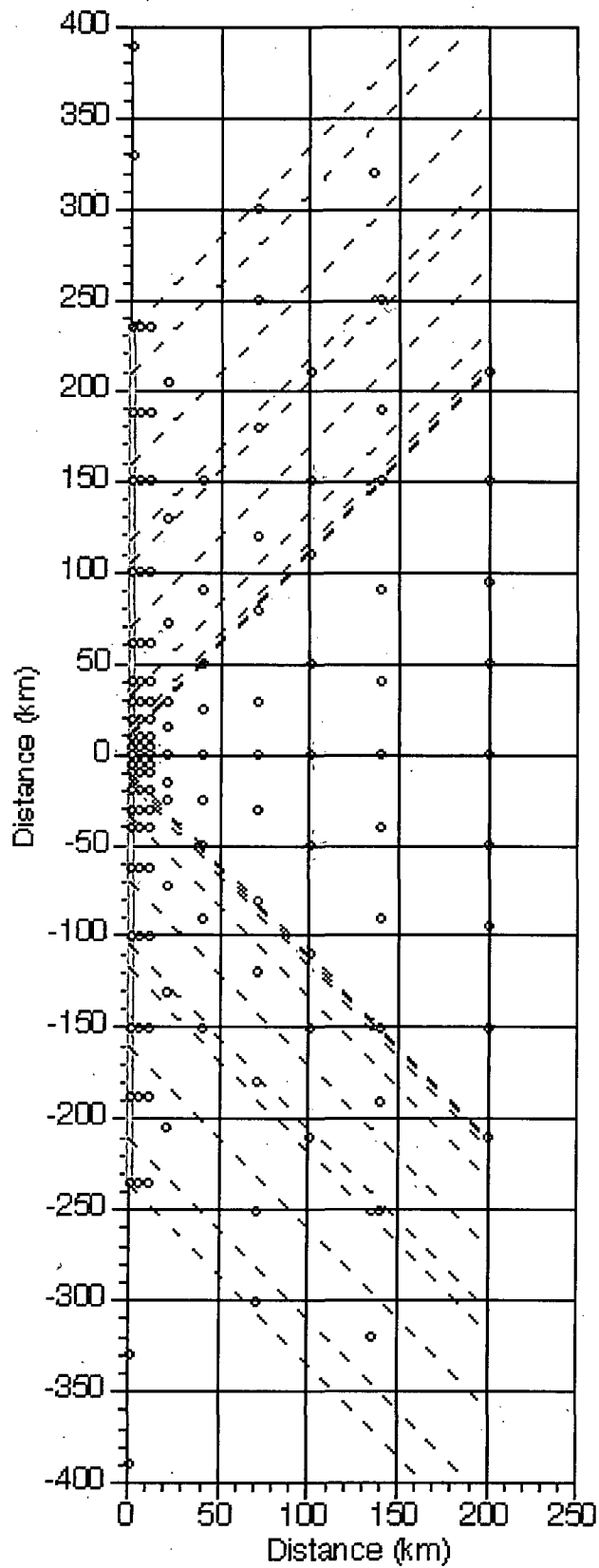
Figure K-2. Station locations for strike-slip simulations.

Shoreline Fault Zone, Appendix K, Update of the Abrahamson (2000) Directivity Model for Strike-Slip
Earthquakes
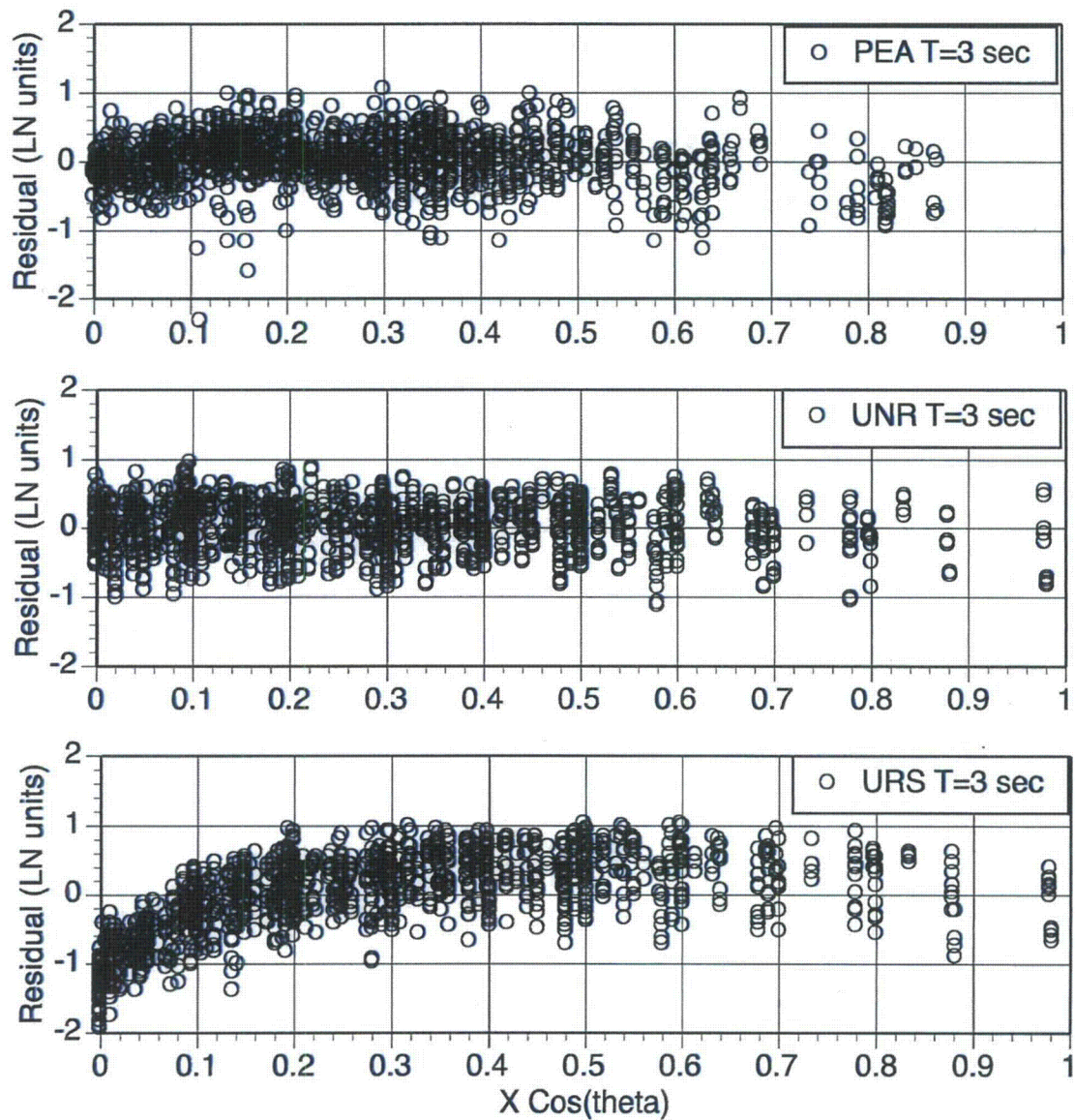
Figure K-3. Comparison of directivity scaling for M7.5 strike-slip (Scenario SE) for T=3 sec for the three different simulation methods.
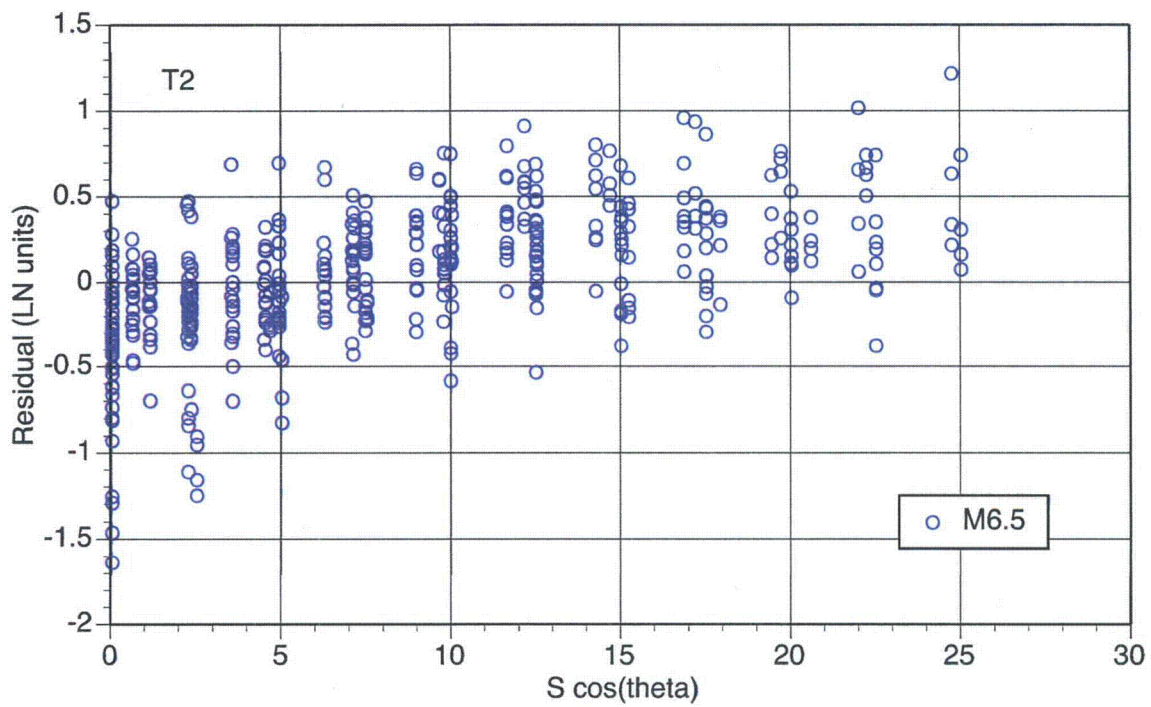
Figure K-4a. Residuals for period T=2 sec and M6.5.
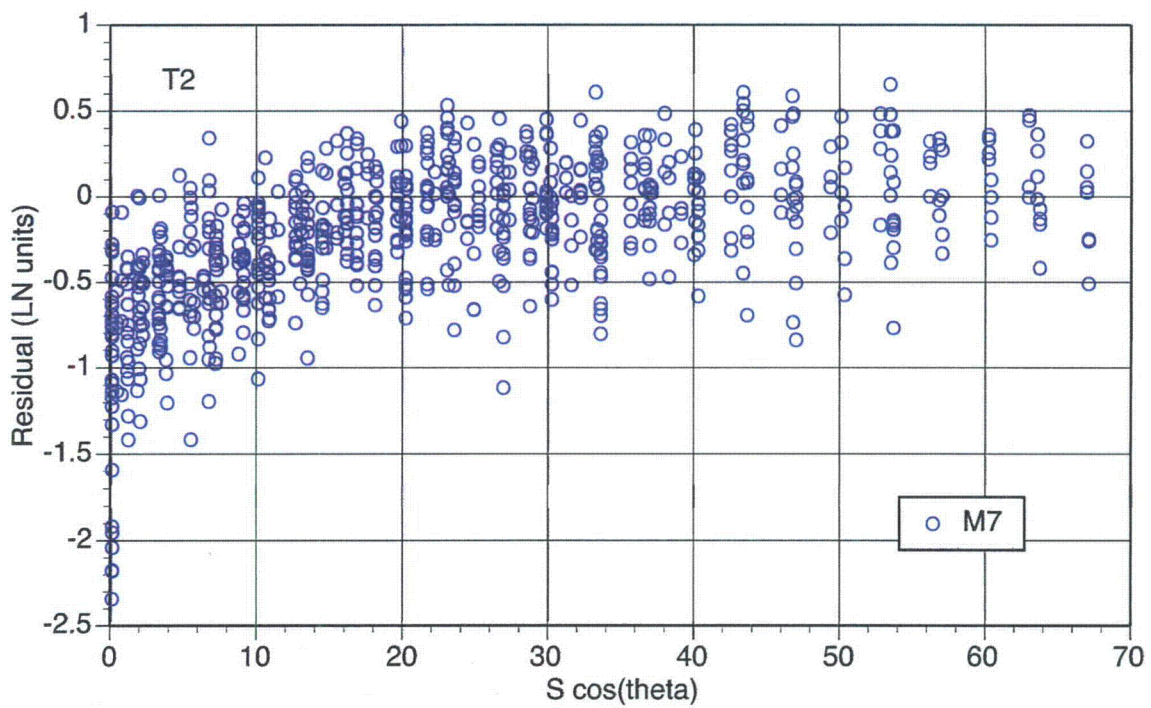
Figure K-4b. Residuals for period T=2 sec, and M7.0.

Shoreline Fault Zone, Appendix K, Update of the Abrahamson (2000) Directivity Model for Strike-Slip Earthquakes
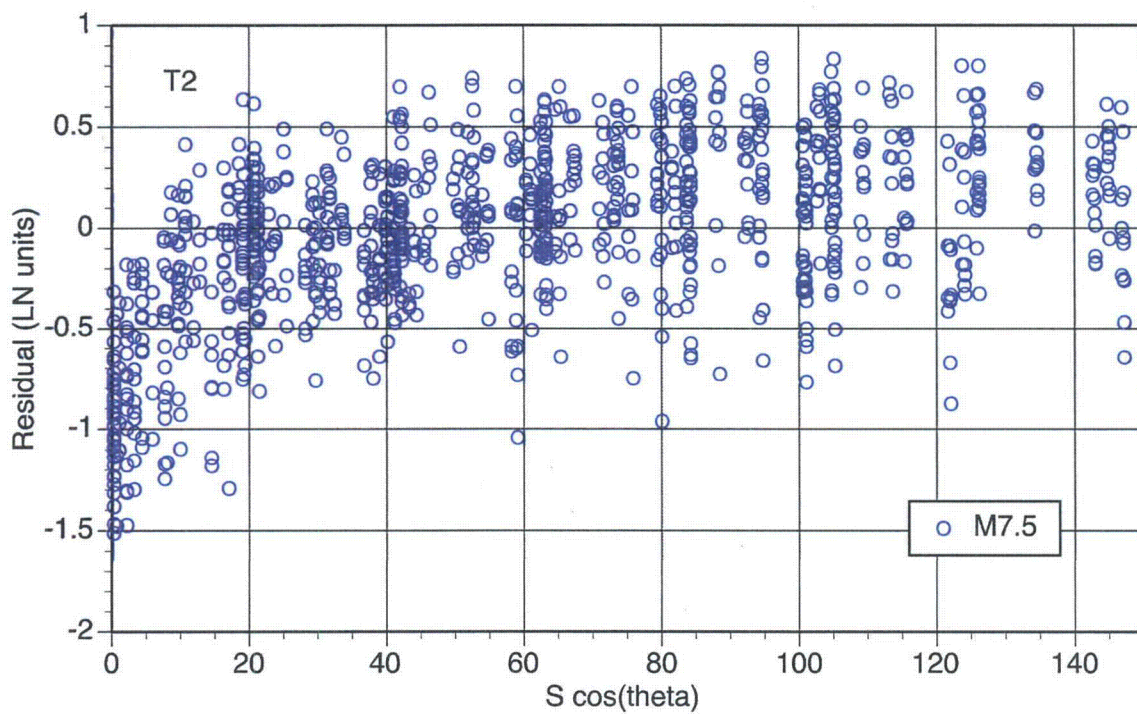
Figure K-4c. Residuals for period T=2 second and M7.5.
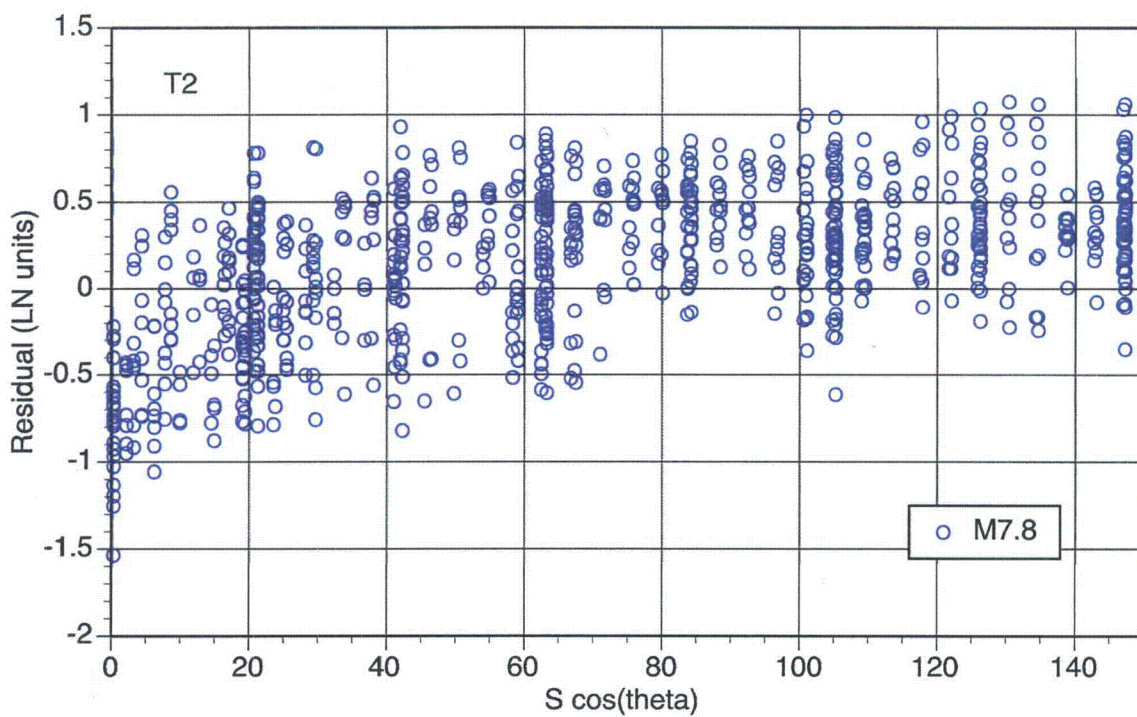
Figure K-4d. Residuals for period T=2 seconds and M7.8.

Shoreline Fault Zone, Appendix K, Update of the Abrahamson (2000) Directivity Model for Strike-Slip Earthquakes
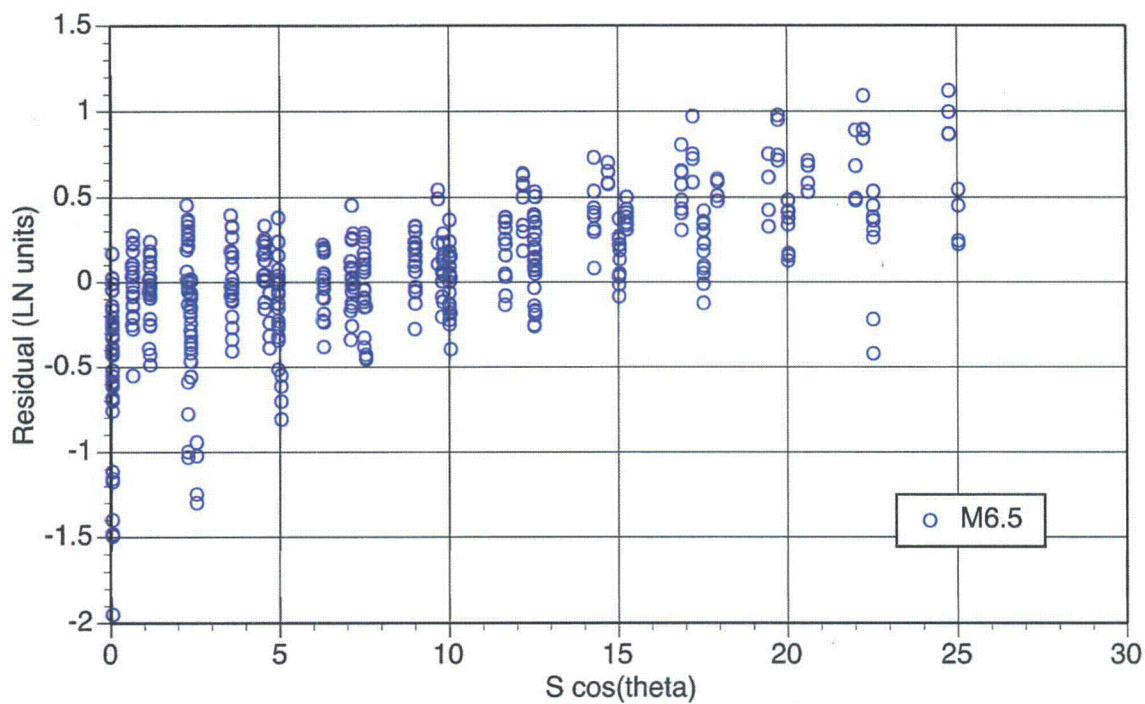
Figure K-5a. Residuals for period T=5 seconds and M6.5.
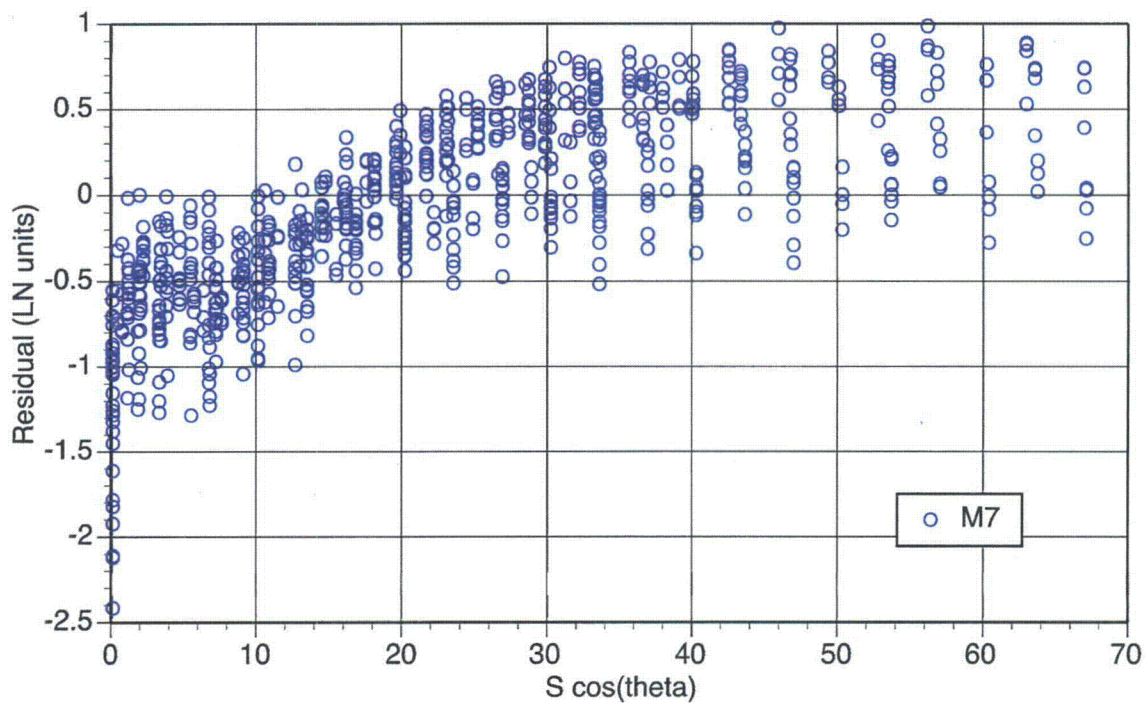
Figure K-5b. Residuals for period T=5 seconds and M7.0.

Shoreline Fault Zone, Appendix K, Update of the Abrahamson (2000) Directivity Model for Strike-Slip Earthquakes
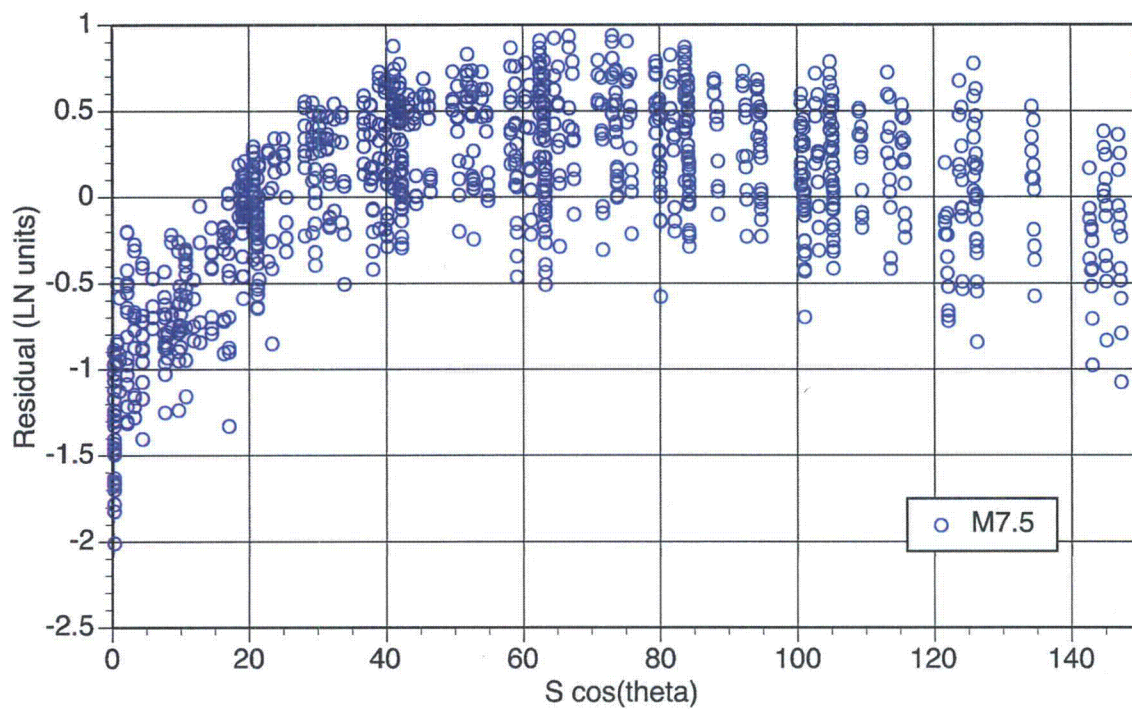
Figure K-5c. Residuals for period T=5 seconds and M7.5.
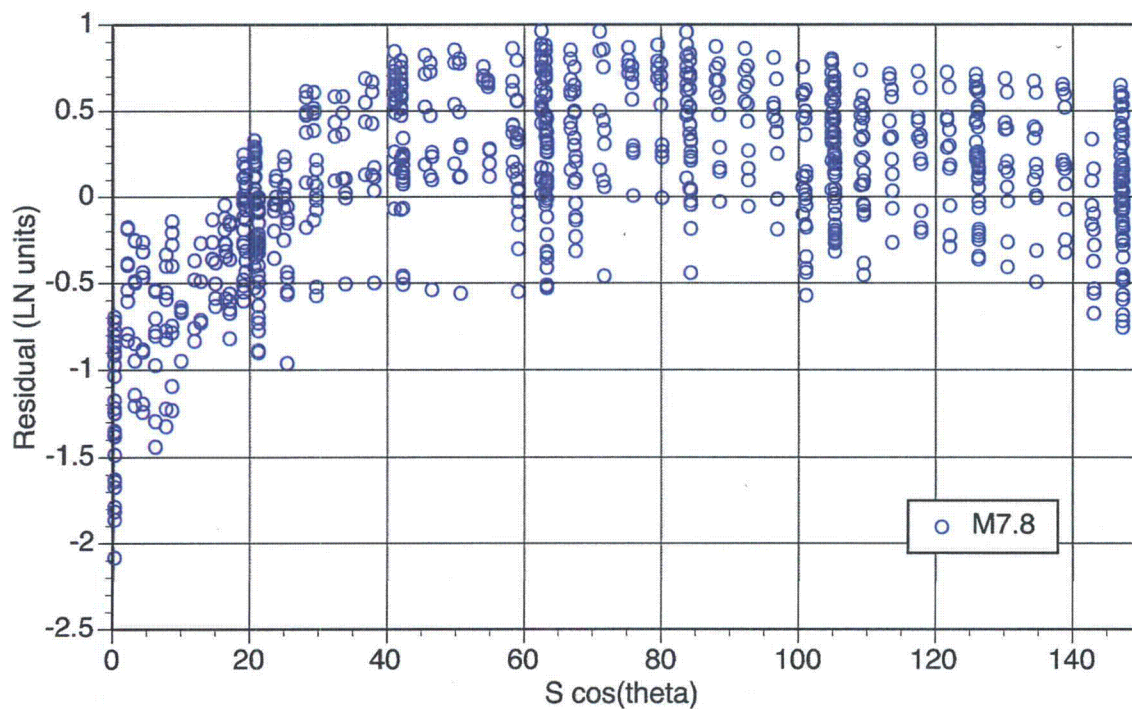
Figure K-5d. Residuals for period T=5 seconds and M7.8.

Shoreline Fault Zone, Appendix K, Update of the Abrahamson (2000) Directivity Model for Strike-Slip Earthquakes
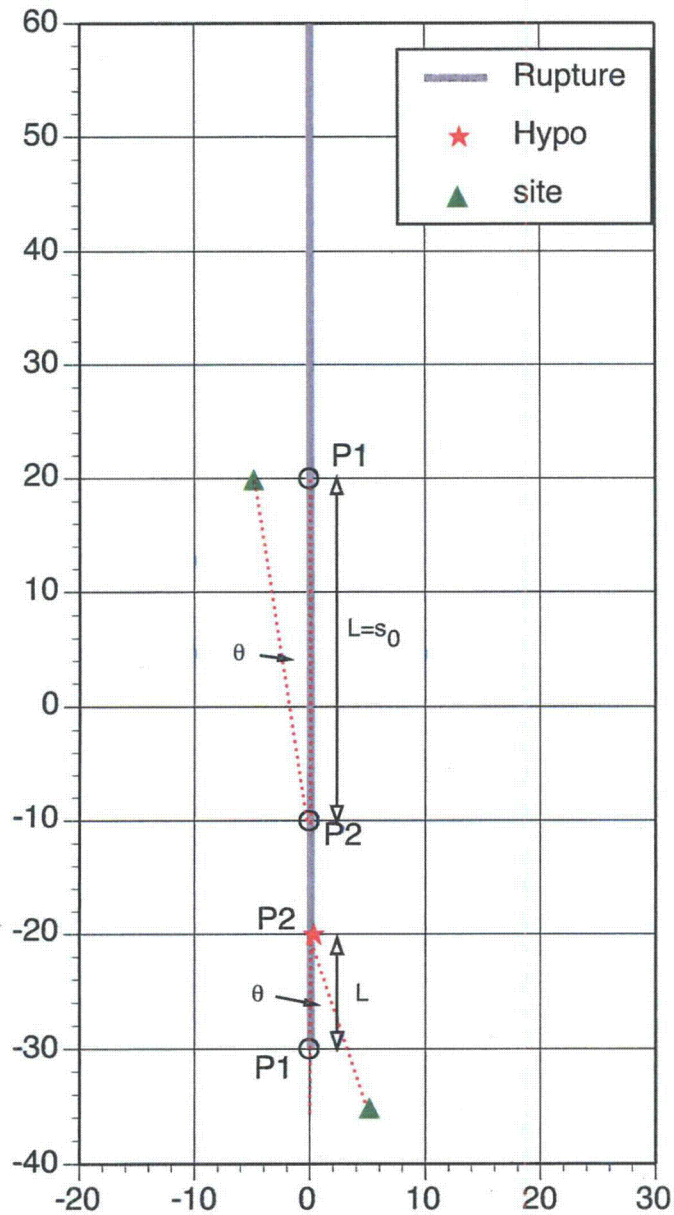
Figure K-6. Examples of the definitions of the segment length and angle for a straight vertically dipping fault. Here, $s_0 = 30$ km.
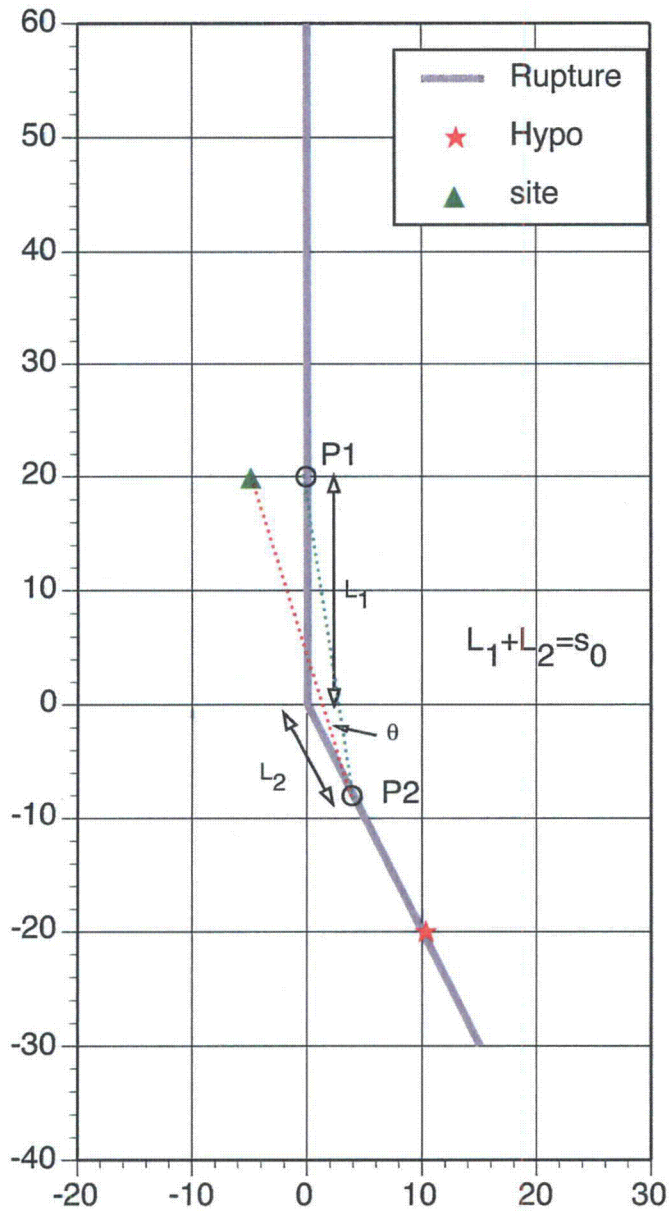
Figure K-7. Example of the definitions of the segment lengths and angle for a bending vertically dipping fault. Here, $s_0 = 30$ km.
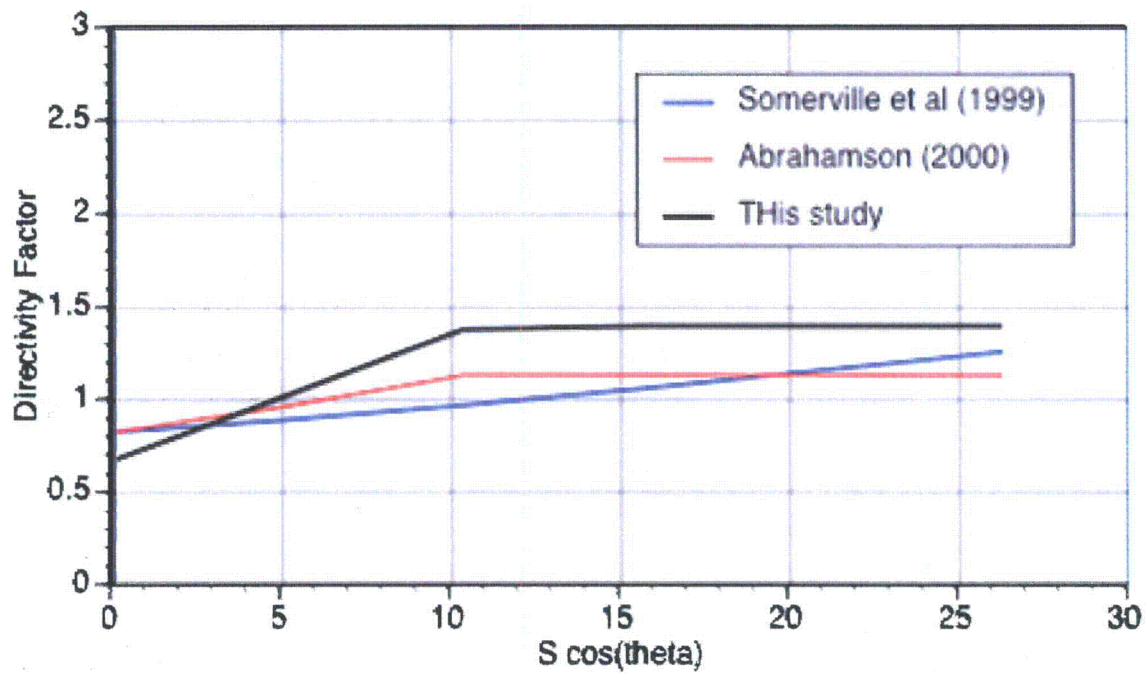
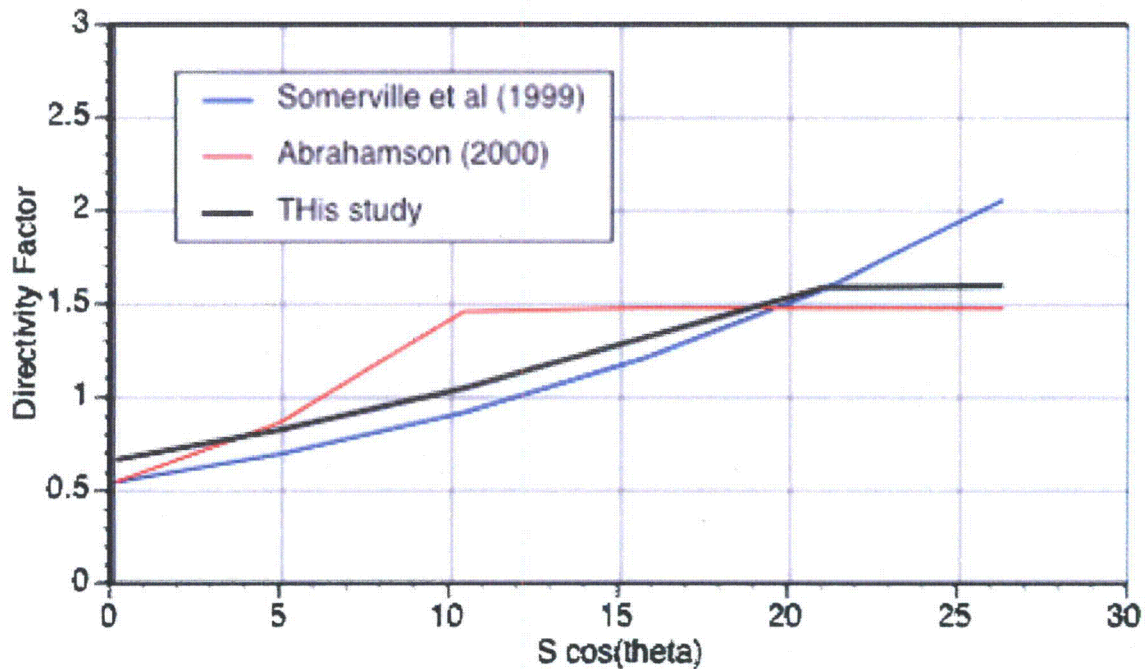Figure K-8a. Comparison of directivity models for T=1 second period and M6.5.

Figure K-8b. Comparison of directivity models for T=3 seconds period and M6.5.
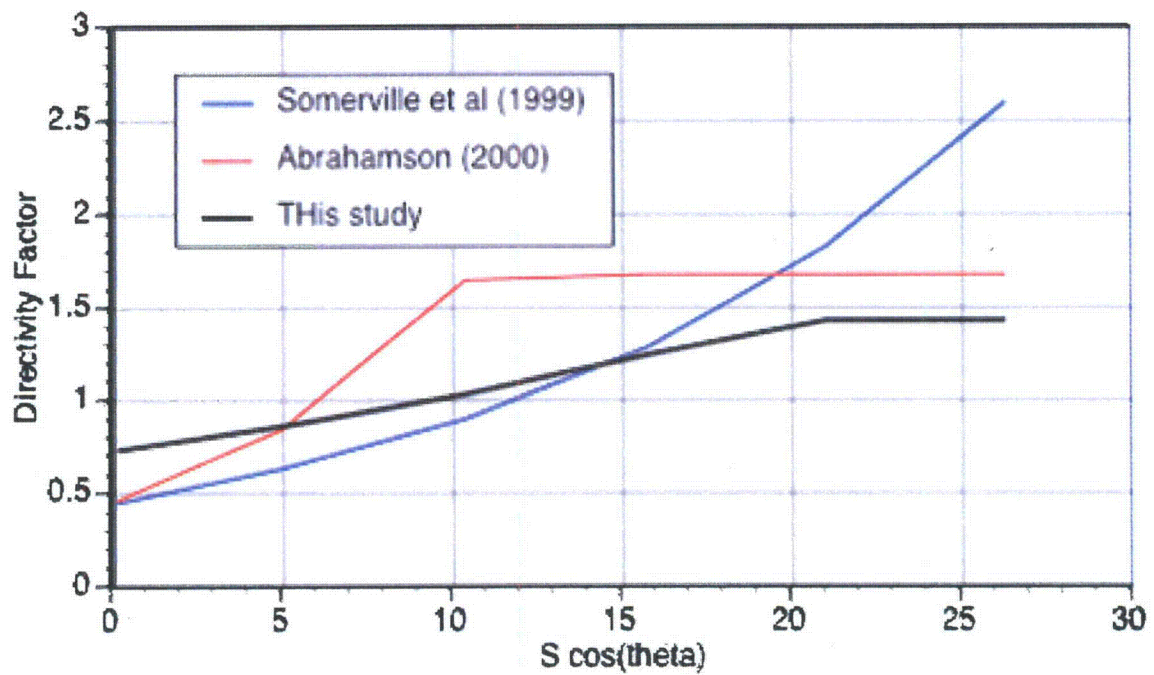
Figure K-8c. Comparison of directivity models for T=5 seconds period and M6.5.
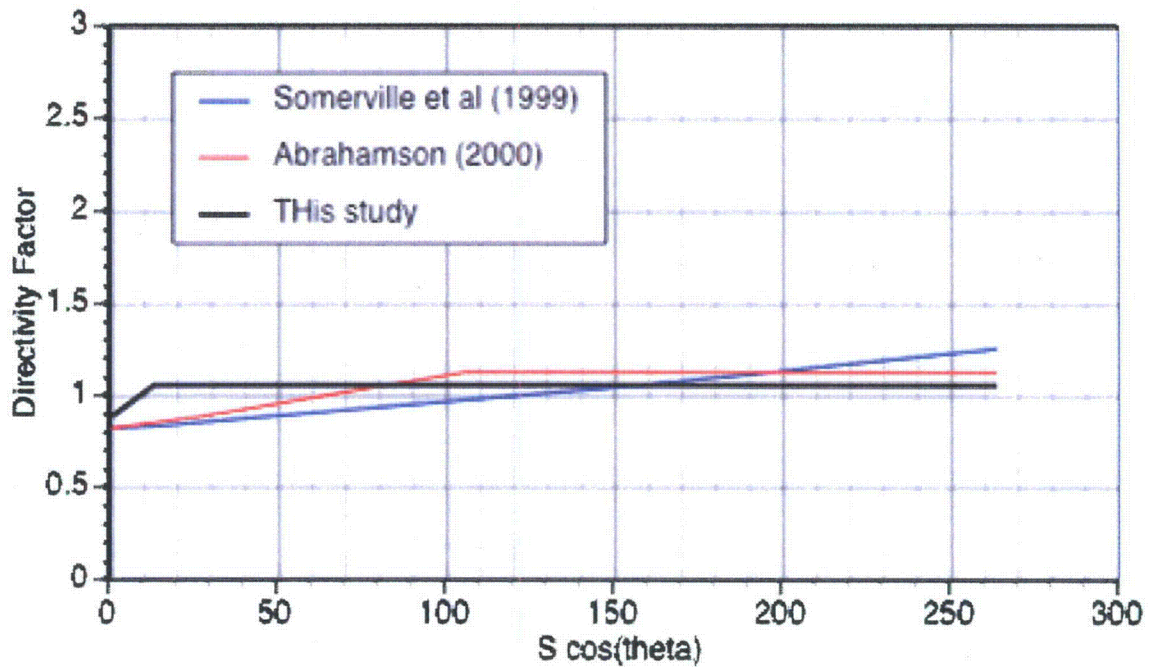
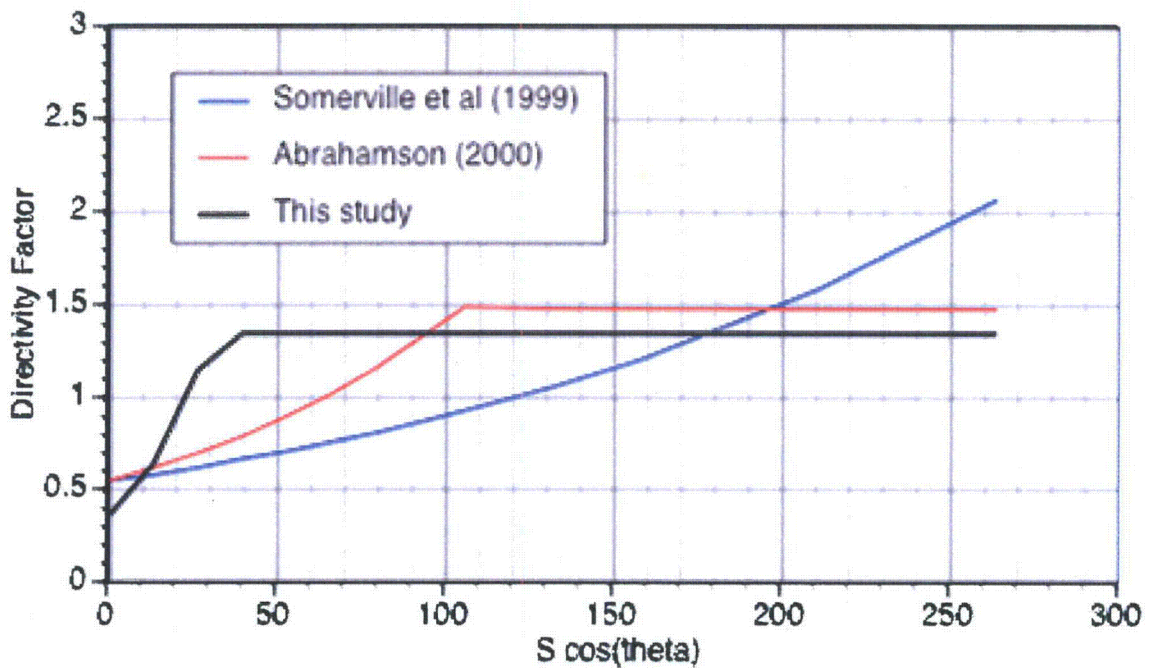Figure K-9a. Comparison of directivity models for T=1 second period and M7.5.

Figure K-9b. Comparison of directivity models for T=3 seconds period and M7.5.

Shoreline Fault Zone, Appendix K, Update of the Abrahamson (2000) Directivity Model for Strike-Slip Earthquakes
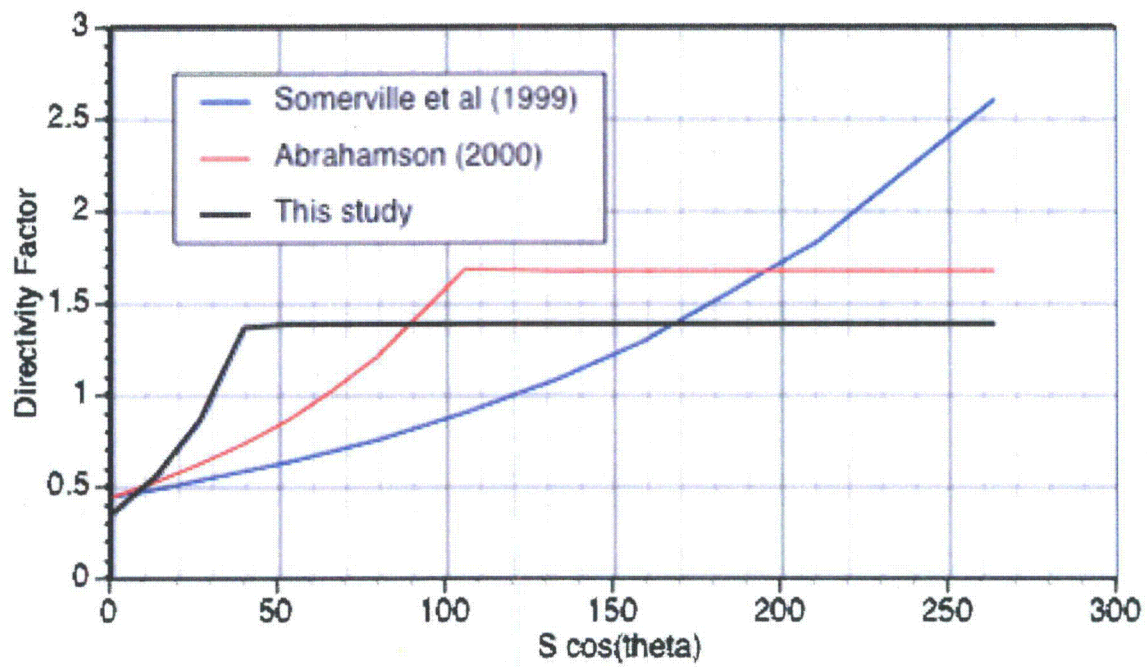
Figure K-9c. Comparison of directivity models for T=5 seconds period and M7.5.
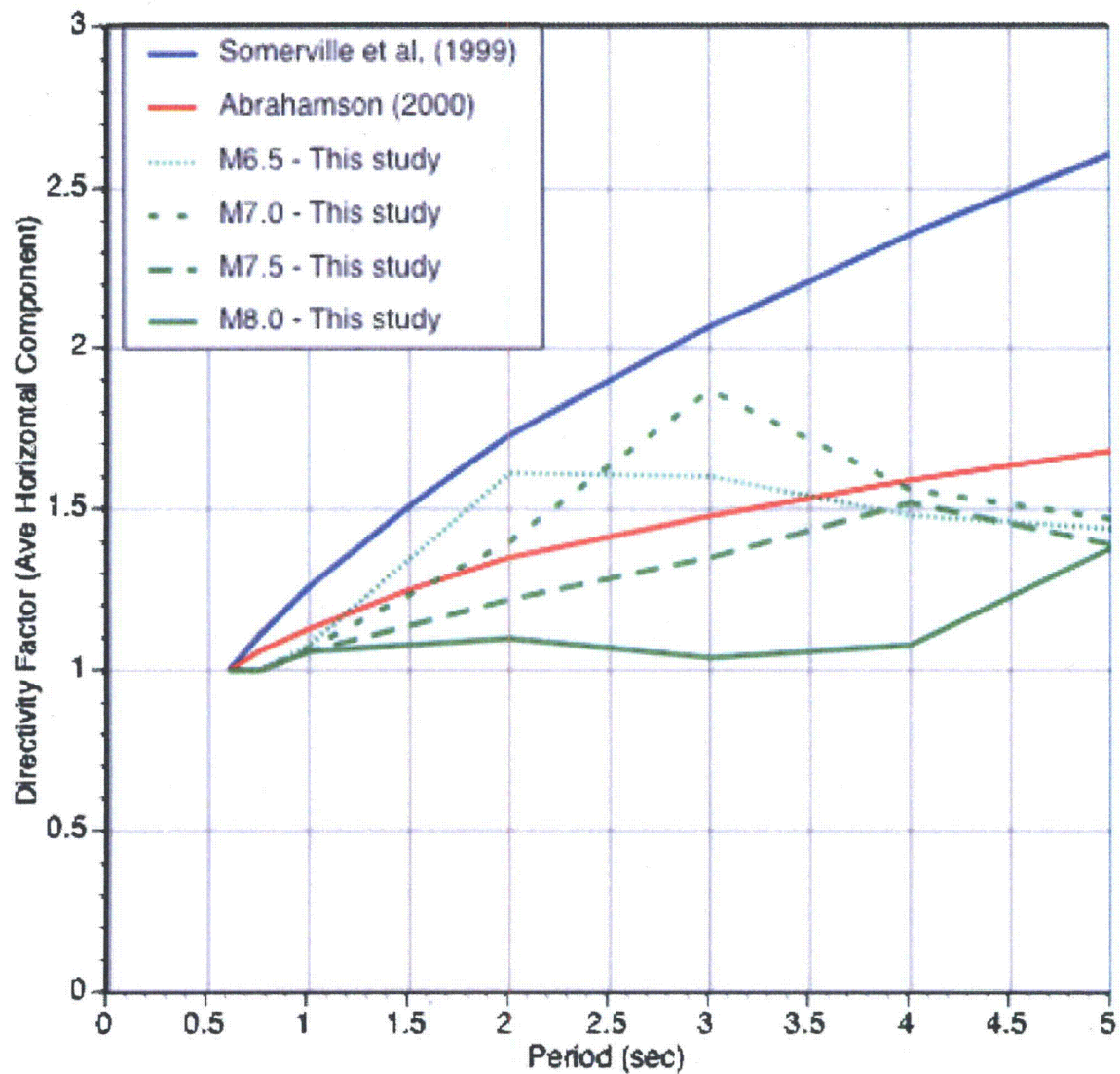
Figure K-8. Comparison of directivity factors for the average horizontal for full directivity (full rupture toward the site) for a site at 1 km distance.

Appendix L

Regional Earthquake Reports
PG&E Geosciences Department

L-1: Deer Canyon Earthquakes of October 18, 2003

L-2: San Simeon Earthquake of December 22, 2003

L-3: Mw 6.0 Parkfield Earthquake of September 28. 2004

Appendix L-1

Deer Canyon Earthquakes of October 18, 2003

Diablo Canyon Power Plant
Deer Canyon earthquakes of October 18, 2003

Two small (M_L 3.4) earthquakes occurred on October 18, 2003 at 12:27 and 12:38 AM PDT (07:27 and 07:38 GMT). The events are located approximately 4 km east of Diablo Canyon Power Plant (DCPP), in the region northwest of Deer Canyon. Both earthquakes were felt in the Unit 1 control room; the second event triggered strong motion instruments at the plant site. The earthquakes are part of a sequence of 14 small earthquakes that occurred between October 12 and October 24, 2003. The following is a report describing the earthquake sequence and strong motion recordings from the plant.

Earthquake Sequence

The Deer Canyon earthquakes were recorded by the PG&E Central Coast Seismic Network (CCSN). The CCSN has operated since 1987 as part of the PG&E Long Term Seismic Program. The CCSN data are augmented by recordings from the U.S. Geological Survey's (USGS) Northern California Seismic Network (NCSN). The CCSN consists of 20 seismographic stations, including five dual-gain 3-component stations (large triangles in inset to Figure 1). The addition of the CCSN, including the three-component stations greatly improves the accuracy of the earthquake locations in the region around DCPP.

The earthquakes are located using the velocity model and station corrections from McLaren and Savage (2000). Duration magnitudes (M_D) also are estimated from the CCSN data. The earthquake location parameters for the 14 events in the sequence are listed in Table 1. Events 1, 4, 5, 11, 12, and 13 (Table 1) were recorded by both the CCSN and NCSN; the combined data from the two networks were used in the locations for these six events.

The Deer Canyon earthquake locations generally are well constrained. Except for event 6, all of the events have small (<1 km) horizontal and vertical depth errors and all have low (<.20 sec) Root Mean Square (RMS) residuals. Except for event 14, all have at least 1 S-wave reading from a station that is at about 1 focal depth distance from the epicenter, providing good depth control.

Figure 1 shows the Deer Canyon sequence with previous earthquakes for the period 1987 to the present. The previous earthquakes were located using the same velocity model and station corrections as the current sequence.

The two magnitude 3 earthquakes of October 18 have similar characteristics. The USGS local magnitude (M_L) for both events is 3.4 (http://usgs.wr.gov); the duration magnitudes (M_D) from the CCSN for the two events are 3.4 and 3.3 for the 12:27 AM and 12:38 AM events, respectively. The earthquake depths also are similar: 6.5 and 6.7 km. (The USGS website reports depths of 2.3 and 2.5 km, respectively, however, due to the better coverage of the combined network and S-wave data, our depths are more accurate.)

Lastly, the focal mechanisms of the two events (events 4 and 5 of Figure 2) both show normal oblique slip.

The Deer Canyon sequence consists of 14 earthquakes with magnitudes ranging from 0.4 to 3.4. Three small earthquakes preceded the October 18 magnitude 3 mainshocks: two on October 12 with magnitudes of 2.3 and 0.5, and one magnitude 1.7 event on October 17. Nine aftershocks have occurred up through October 24 with magnitudes less than M2.6. The first preshock (event 1 of Table 1) occurred in the same depth range (6.5 km) as the two magnitude 3 earthquakes. The second two preshocks and nearly all of the aftershocks are located in a narrow depth range at about 3.7 km; the exception is event 11 that was located at a depth of 8.9 km. This deeper event was located away from the other aftershocks, about 7 km NW of the mainshocks (Figure 1).

The Deer Canyon earthquakes occurred within the San Luis/Pismo structural block. The San Luis/Pismo structural block is one of three distinct uplifting structural blocks of the Los Osos domain (Lettis et al, 2001). The block is bounded on the west by the Hosgri fault zone and on the northeast and southwest by west-northwest-trending, high-angle reverse Quaternary faults (Los Osos and Southwest boundary fault zones of Figure 1); crustal shortening is accommodated primarily by reverse faulting along the northwest trending block margins (Lettis, et al. 2001).

The San Luis/Pismo block is highly fractured. Figure 1 shows the Deer Canyon sequence and the previous earthquakes. The previous seismicity shows scattered activity across the San Luis/Pismo block; the Deer Canyon earthquakes locate within this region of previous activity.

Cross section AA' perpendicular to the long axis of the block (Figure 1) shows that the previous seismicity is approximately uniformly distributed in depth. The depth range of the main Deer Canyon sequence, from 3.4 to 6.7 km, is consistent with the depth range of the previous seismicity.

Earthquakes occurring within the block generally have had a variety of focal mechanisms (Figure 2). The normal oblique mechanisms for the magnitude 3 events on October 18 and the reverse mechanisms of aftershocks 11 and 13 are consistent with the mechanisms of past earthquakes in this region.

Strong ground motion

Both earthquakes were felt in the Unit 1 control room; the operators reported that the second event was the stronger. The first event did not trigger the seismic instruments. The second event did not trigger the Basic Seismic System analog recorder (Kinemetrics SMA) in the control room, however the Kinemetrics digital recorders (SSA) at the Unit 1 containment base, top of containment, the auxiliary building, and the free-field pit location (near the fitness trailer) did trigger on the second event. According to David Castleman of Kinemetrics, Inc., the SMA system worked properly; however, the system did not trigger because the containment base ground motions contained significant energy

outside the 1.0 to 10.0 Hz bandwidth of the SMA trigger. The Supplemental System was inoperable at the time of the earthquakes; however, three temporary accelerometers (TerraTech GSR-18), located in the Auxiliary and the Turbine buildings, recorded the second event. The peak accelerations are listed in Table 2.

The earthquake force monitor (EFM) located in the control room measured 0.02g on the vertical component. The EFM measurement is from the sensor at the Unit 1 Containment base and does not have the DC offset removed. If the DC offset is removed, the peak acceleration on the vertical component is 0.011g.

The ground motions from the free-field and containment base were corrected by removing the DC offset, filtering the long period noise, and removing the baseline drift. First, the DC offset was removed using the average of the first 50 samples from the pre-event part of the accelerogram. Next, the accelerograms were high-pass filtered using a 4-pole Butterworth filter with a corner-frequency at 1 Hz. This corner-frequency was selected by evaluating the Fourier spectrum of the unfiltered accelerations which indicated noise at periods greater than 1 second. Finally, the baseline drift was removed using a high-order polynomial (without the constant and linear terms) fit to the displacement waveform. The corrected acceleration, velocity, and displacement time seismograms for the three components of motion at the free-field stations are shown in Figures 3a, 3b, and 3c. Similar plots of the acceleration, velocity, and displacement seismograms for the Unit 1 containment base are shown in Figures 4a, 4b, and 4c. These seismograms show that the shaking at the DCPP site had a duration of strong shaking of 3 seconds. The containment base recordings appear to still have long period noise at a frequency of about 1 Hz that was not completely removed by the filtering (see displacement seismograms in Figures 4a, 4b, and 4c). Additional filtering could remove this noise, but it would also begin to affect the part of the ground motion that is not noise (e.g. at the S-wave arrival). This noise does not affect the peak values.

Table 3 lists the peak accelerations, peak velocities, and peak displacements of the free-field and Unit 1 containment base ground motions after the filtering and baseline corrections are applied. The peak accelerations range between about 1 to 2% g with the largest peak acceleration on the vertical component.

The response spectra were computed for the free-field and Unit 1 containment base recordings. The 5% damped spectra for the free-field and Unit 1 containment base recordings are shown in Figure 5 and 6, respectively. The response spectra for this earthquake show very high frequency content that is typical for an earthquake of this magnitude. For the free-field, the horizontal spectra peak at about 12 Hz and the vertical spectrum peaks at about 20 Hz. For the Unit 1 containment base, the peaks are shifted to slightly smaller frequencies. This shift to lower frequencies is an expected effect of the large foundation. The ratio of the average horizontal response spectrum from the containemt base to the free-field station is shown in Figure 7. This response spectral ratio shows the reduction in high frequency content on the containment base compared to the free-field recording.

The magnitude of the earthquake is too small to reliably use standard empirical attenuation relations to evaluate the strength of the ground motion. As an alternative to empirical attenuation relations, the ground motion can be evaluated using the stochastic point source model (Boore, 2000). The stochastic model is used to estimate the ground motion expected for a (moment) magnitude 3.4 earthquake at a hypocentral distance of 7.8 km for typical rock site conditions in California. The response spectrum computed for a stress-drop of 120 bars and a kappa of 0.042 seconds is compared to the average horizontal spectrum from the free-field recording in Figure 8. This comparison shows that the frequency content of the free-field ground motion is consistent with the expected frequency content for a magnitude 3.4 earthquake with a kappa value that is typical of California rock sites. The level of shaking is consistent with a stress-drop of 120 bars. A stress-drop of 120 bars is higher than average for California earthquakes, but it is within the range of observed stress-drops for small magnitude events. The underestimation of the ground motion at frequencies less than 3 Hz may indicate that the moment magnitude is greater than 3.4 (e.g. the M_L may be underestimating the moment magnitude for this event). If the moment magnitude is 3.5, then the fit to the lower frequencies is improved and the stress-drop is reduced to 85 bars which is close to the average stress-drop for small earthquakes in California.

Conclusions

The occurrence, location, and magnitude of the October 18, 2003 Deer Canyon earthquakes is not a surprise as the sequence of earthquakes is consistent with our understanding of the tectonic framework in the region around DCPP. The events occurred in the San Luis/Pismo block, which is a region of previous seismicity. Additional small earthquakes are expected to occur in this block.

The ground motions from the second event (12:38 AM) are typical for ground motions from a magnitude 3.4 earthquake at a distance of 7.8 km on a rock site condition.

<u>References</u>

Boore, D. M (2000). SMSIM – Fortran programs for simulating ground motions from earthquakes: version 2.0 – a revision of OFR 96-80-A, U.S. Geological Survey OFR 00-509.

Lettis, W. R., Hanson, K. L., Unruh, J. R., McLaren, M. K., and Savage, W. U. (2001) Quaternary tectonic setting of south-central coastal California, in *Evolution of Sedimentary basins/onshore oil and gas investigations- Santa Maria Province*, M. A. Keller (Editor), *U. S. Geol. Survey Bull.* (in press)

McLaren, M. K. and Savage, W. U. (2000). Seismicity of South-Central Coastal California: October 1987 through January 1997, *Bull Seism. Soc. Am.* **91**, no. 6, pp. 1629-1658.

Pacific Gas and Electric Company (1988), Final report of the Diablo Canyon long term seismic program, U.S. Nuclear Regulatory commission docket Nos. 50-75 and 50-23.

Report prepared by Ms. Marcia McLaren and Dr. Norman Abrahamson of the PG&E Geosciences Dept.

Date: November 5, 2003

Table 1: Earthquake location parameters for the Deer Canyon sequence, 10/12/03 to 10/24/03.
Felt events are highlighted in gray.

No.	Date	Time (UTC)	Lat	Lon	Depth	No. P- & S-wave readings	Gap btwn stas. (deg)	Dist. to nearest station (km)	RMS (sec)	*M$_D$	No. S-wave readings	Horiz. Error (km)	Vert. Error (km)	No. P-wave first motions
1	10/12/2003	13:32 28.54	35 11.97	-120 48.83	6.6	52	145	3	0.13	2.3	2	0.41	0.39	43
2	10/12/2003	16:57 37.60	35 12.28	-120 47.59	3.8	6	137	3	0.07	0.5	1	0.66	0.33	5
3	10/17/2003	13:19 14.33	35 12.49	-120 47.88	3.6	34	123	3	0.14	1.7	4	0.37	0.17	30
4	10/18/2003	07:27 18.37	35 12.23	-120 48.53	6.5	57	125	3	0.12	3.4	2	0.23	0.39	101
5	10/18/2003	07:38 59.14	35 12.15	-120 48.52	6.7	60	127	3	0.12	3.3	2	0.25	0.35	112
6	10/18/2003	07:40 49.52	35 12.10	-120 47.81	3.7	6	149	4	0.05	0.4	1	3.09	1.79	5
7	10/18/2003	07:41 43:44	35 12.18	-120 47.92	3.7	9	147	4	0.09	1.1	1	0.85	0.44	8
8	10/18/2003	07:55 18.96	35 12.13	-120 47.88	3.7	16	132	4	0.12	1.3	3	0.52	0.21	11
9	10/20/2003	10:38 21.93	35 12.24	-120 47.97	3.6	9	146	4	0.07	1.1	1	0.61	0.31	7
10	10/20/2003	18:22 37.72	35 12.35	-120 48.05	3.8	9	142	3	0.07	0.9	1	0.67	0.33	8
11	10/20/2003	19:28 31.85	35 15.05	-120 44.37	8.9	46	50	4	0.10	1.5	3	0.43	0.61	15
12	10/21/2003	08:35 40.18	35 12.43	-120 48.00	3.6	24	125	3	0.11	1.2	2	0.54	0.25	12
13	10/21/2003	13:43 36.44	35 12.65	-120 48.20	3.7	37	119	3	0.12	2.6	3	0.36	0.17	41
14	10/24/2003	23:30 52.84	35 12.06	-120 47.73	3.4	6	147	4	0.07	0.7	0	0.52	0.33	6

*M$_D$ = duration magnitude

Table 2. Digital peak acceleration recordings from the Basic and temporary Supplemental systems (DC offset removed, prior to filtering and baseline correction)

Instrument type	Instrument location	Peak Accelerations (g)		
		Channel 1 (Horiz 1)	Channel 2 (Vertical)	Channel 3 (Horiz 2)
Kinemetrics SSA	Free field pit (near admin bldg)	-0.020	-0.022	0.011
Kinemetrics SSA	Unit 1 Containment base, 89' elev.	-0.008	-0.011	-0.009
Kinemetrics SSA	Unit 1 top of Containment	-0.032	0.14	-0.024
Kinemetrics SSA	Auxiliary Bldg, 64 ' elev.	0.005	0.010	0.006
Terratech GSR-18	Auxiliary Bldg, 64' elev.	0.009	0.021	-0.011
Terratech GSR-18	Turbine Bldg Unit 1, 85' elev.	0.013	0.024	0.009
Terratech GSR-18	Turbine Bldg Unit 2, 85' elev.	0.010	0.024	-0.014
Terratech GSR-18	500 KV switchyard control room basement	0.025	0.013	0.014

Table 3. Peak ground motions values from the Basic Seismic System digital recorders (after filtering and baseline correction)

Instrument type	Instrument location	Component	Peak Acceleration (g)	Peak Velocity (cm/s)	Peak Displacement (cm)
Kinemetrics SSA	Free field pit (near fitness trailer)	Horizontal 1 (Channel 1)	0.020	0.32	0.0100
		Vertical (Channel 2)	0.022	0.19	0.0042
		Horizontal 2 (Channel 3)	0.011	0.19	0.0068
Kinemetrics SSA	Unit 1 Containment base, 89' elev.	Horizontal 1 (Channel 1)	0.008	0.16	0.0077
		Vertical (Channel 2)	0.012	0.16	0.0060
		Horizontal 2 (Channel 3)	0.009	0.22	0.0094
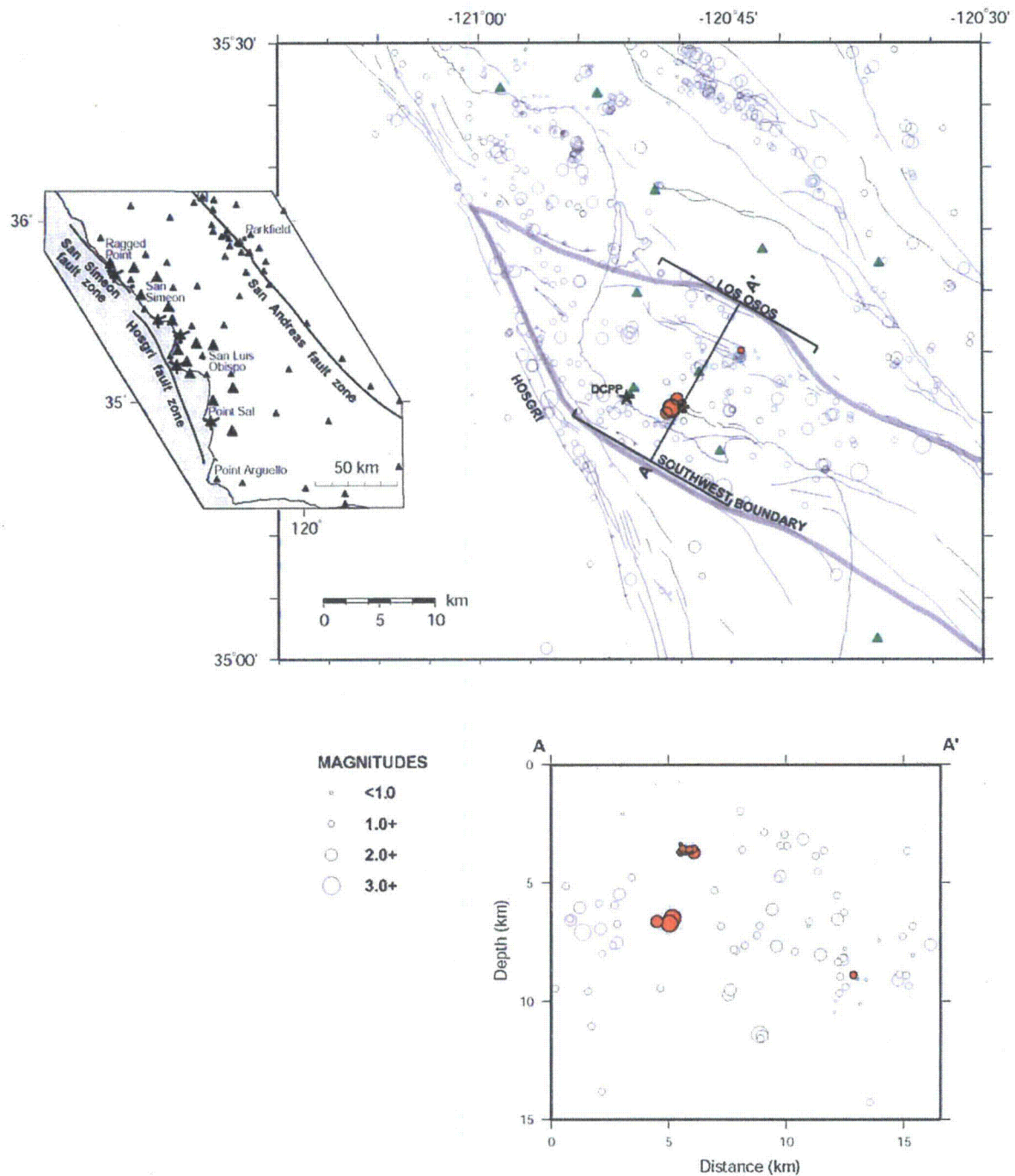
Figure 1. Map and seismic cross section showing the Deer Canyon sequence (orange circles) from October 12 through October 24, 2003 with previous earthquakes (grayed circles) from October 1987 to October 11, 2003. The data were recorded by the PG&E Central Coast Seismic network (large triangles on top figure inset; triangles with tick marks are 3-component stations) and the Northern California Seismic network (small triangles on top figure inset). Seismic stations also are shown on larger map(green triangles). Location of seismic cross section AA' is shown on map with 8-km-wide bars to mark events projected on to the cross section in bottom figure. Quaternary faults are from PG&E (1988); selected faults are labeled. The thick gray line is the boundary of the San Luis/Pismo structural block (Lettis and others, 2001).
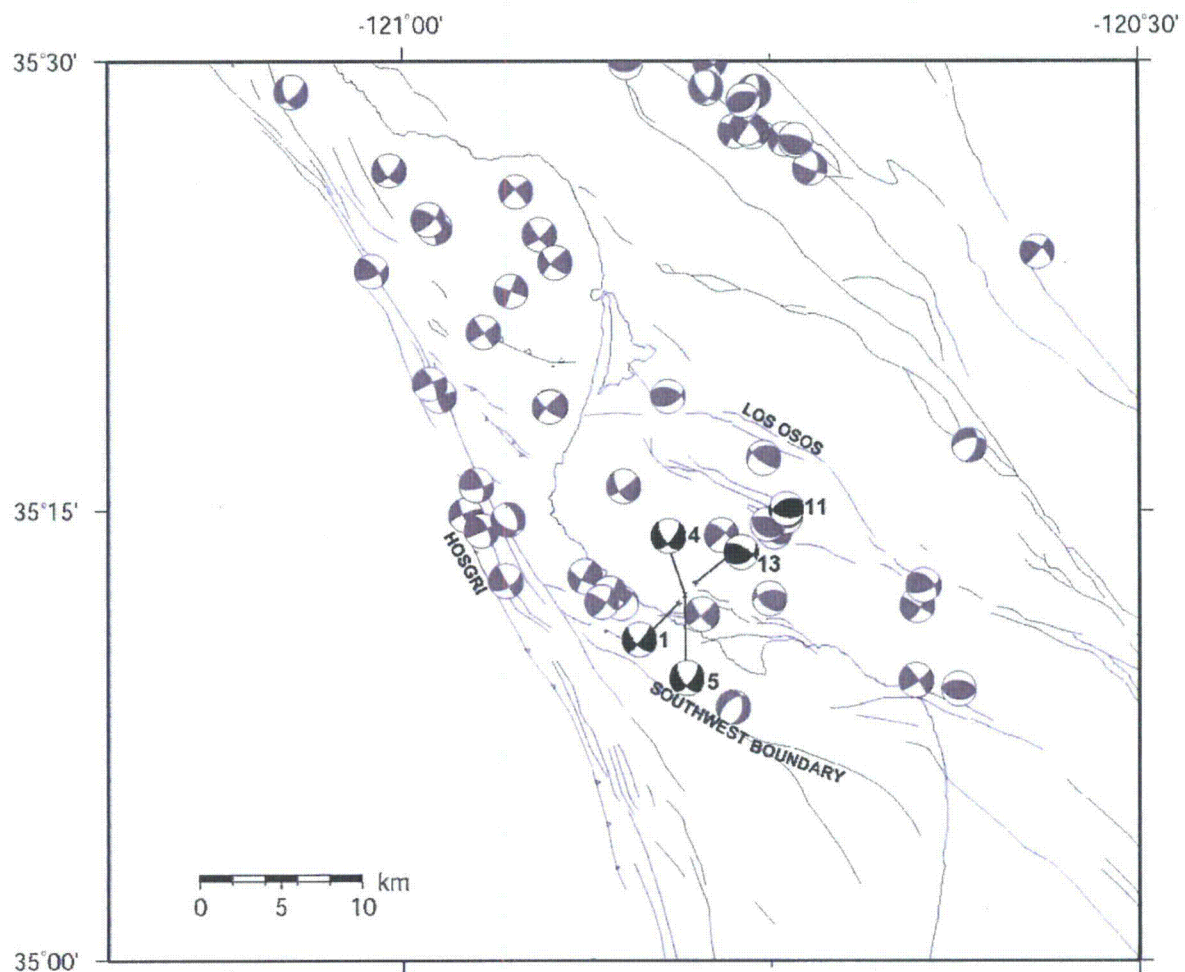
Figure 2. Lower hemisphere P-wave focal mechanisms. Grayed mechanisms are from McLaren and Savage (2000) for the time period October 1997 through January1997. Darker mechanisms are from the Deer Canyon sequence and are numbered according to Table 1. See Figure 1 for fault description.
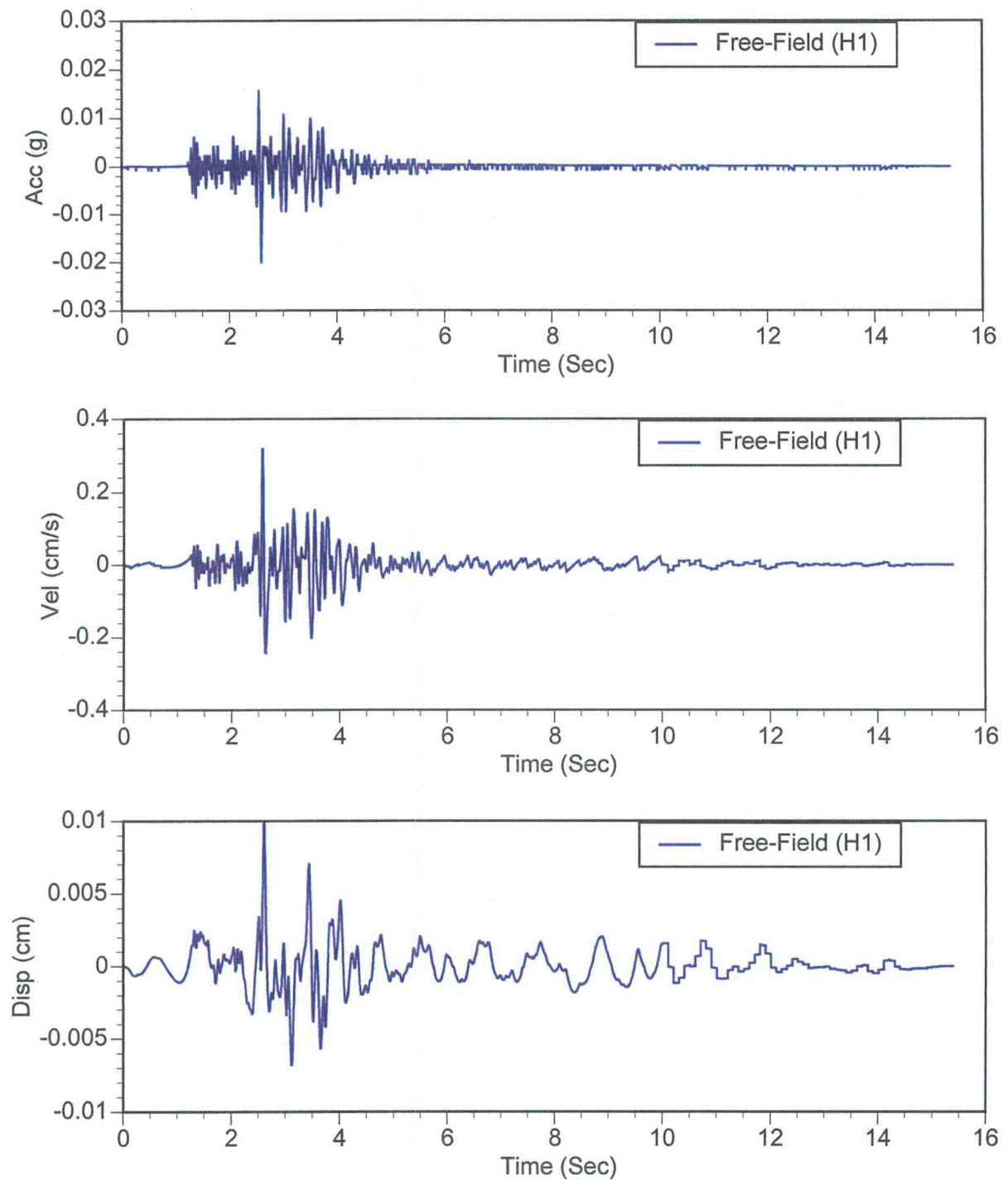
Figure 3a. Acceleration, velocity, and displacement for the horizontal 1 component (channel 1) of the free-field recording after filtering and baseline correction.
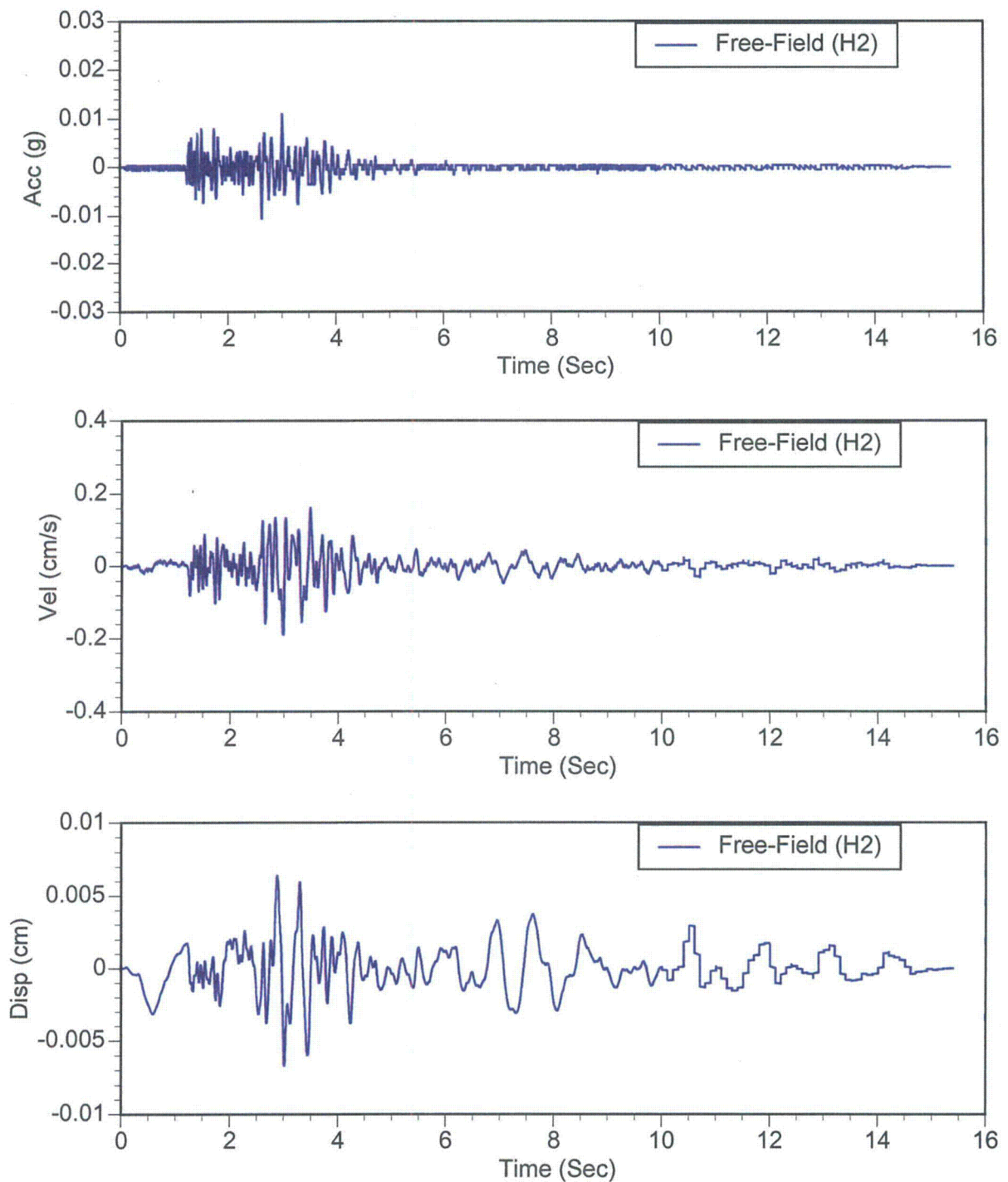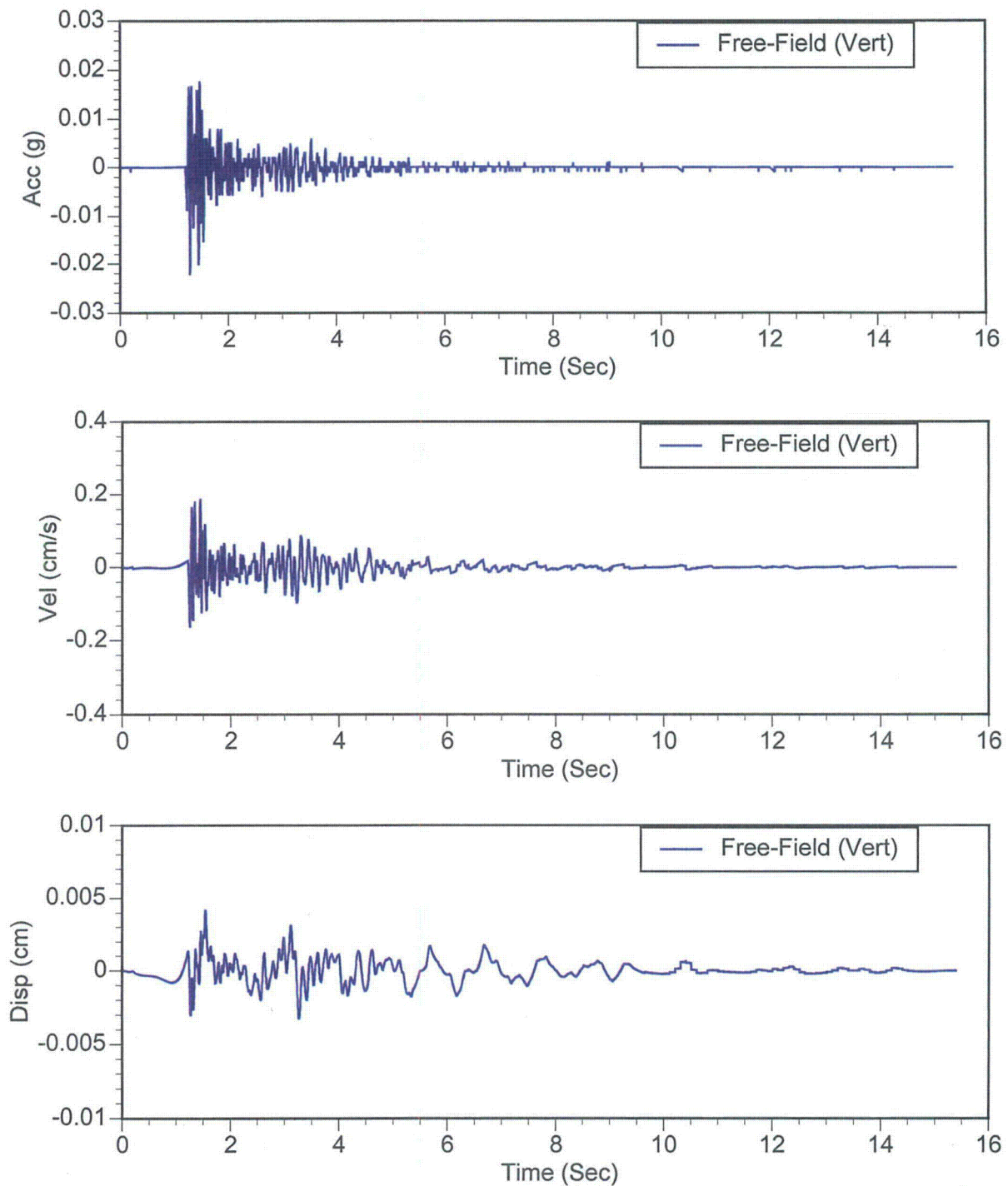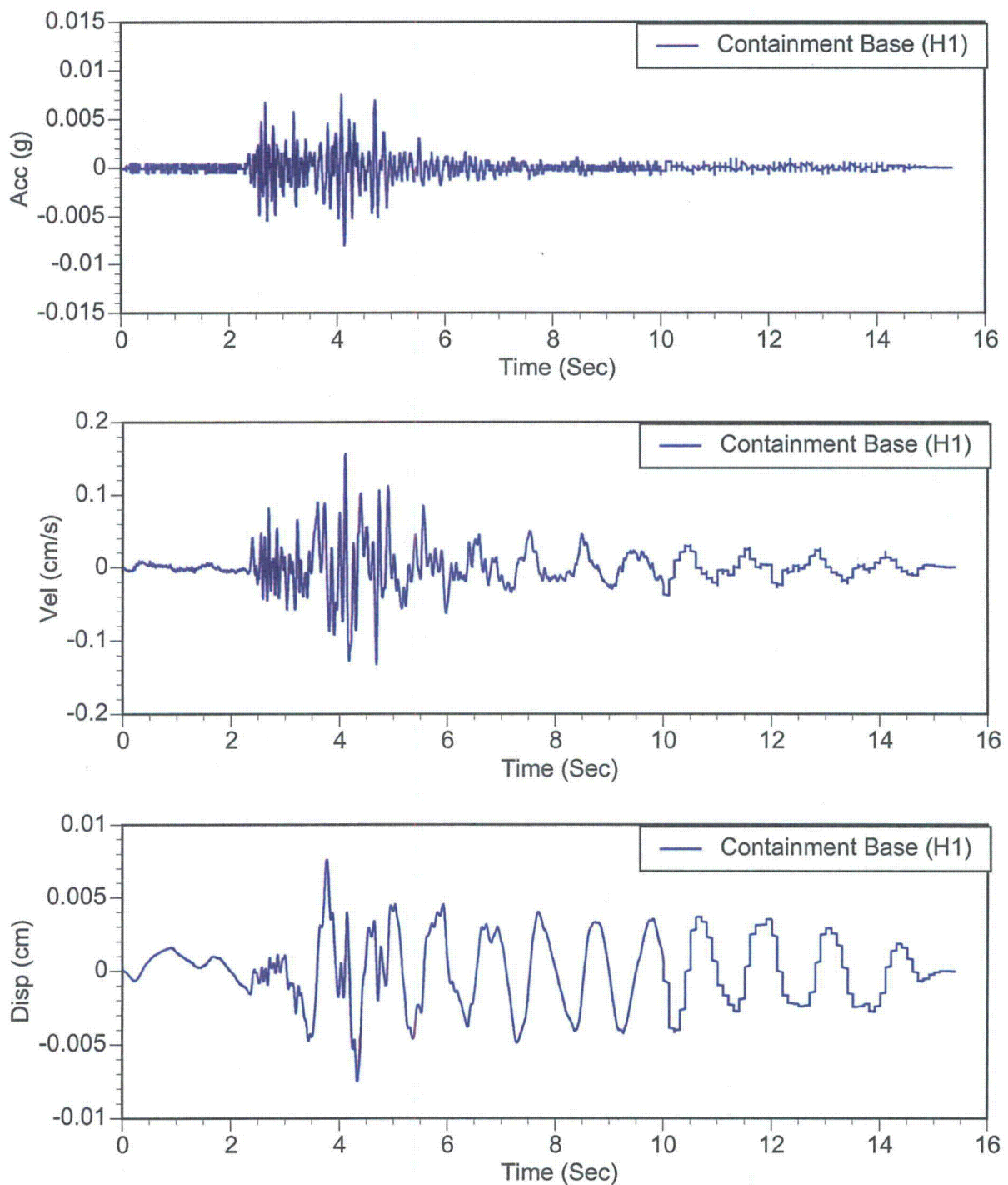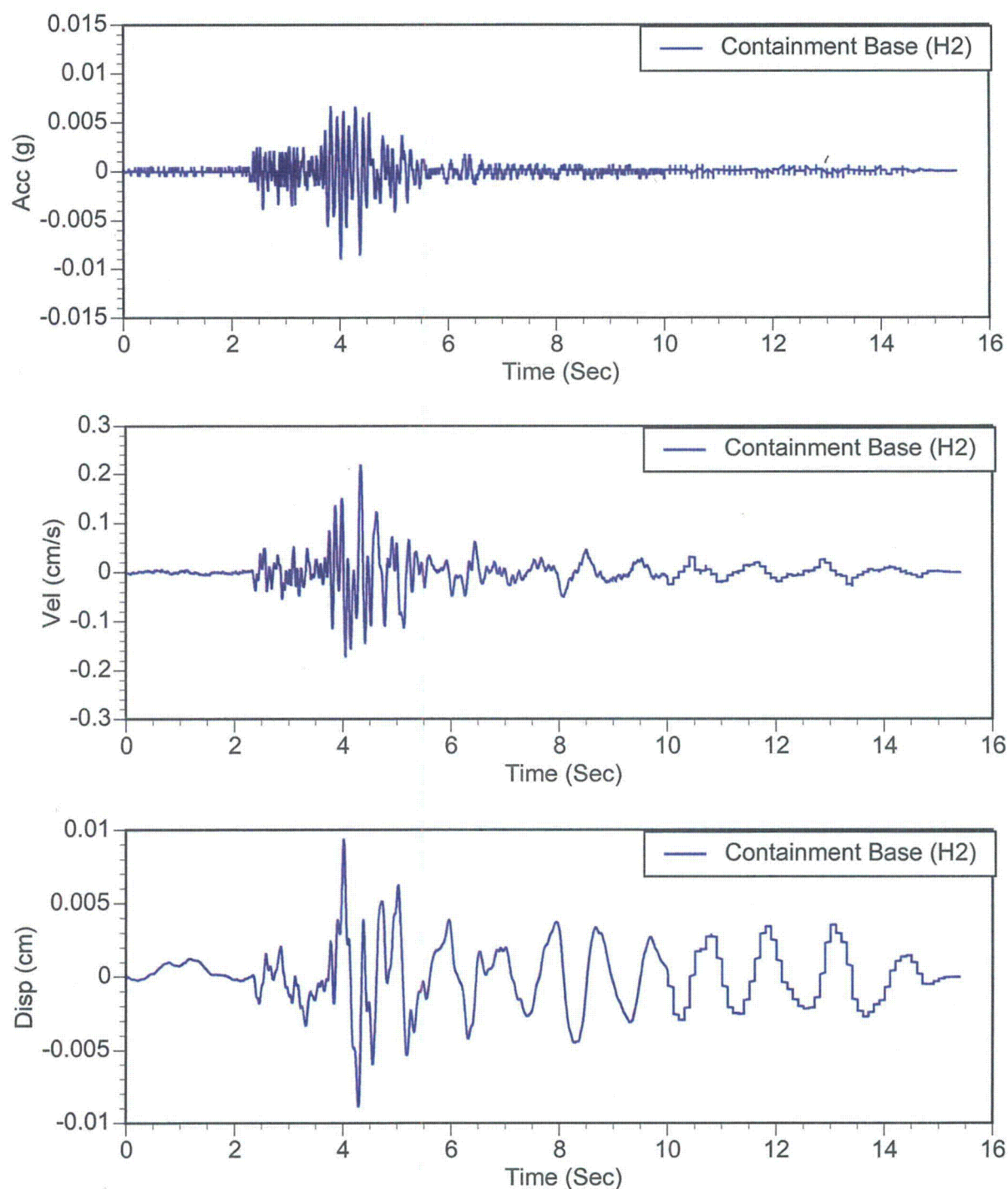
Figure 3b. Acceleration, velocity, and displacement for the horizontal 2 component (channel 3) of the free-field recording after filtering and baseline correction.
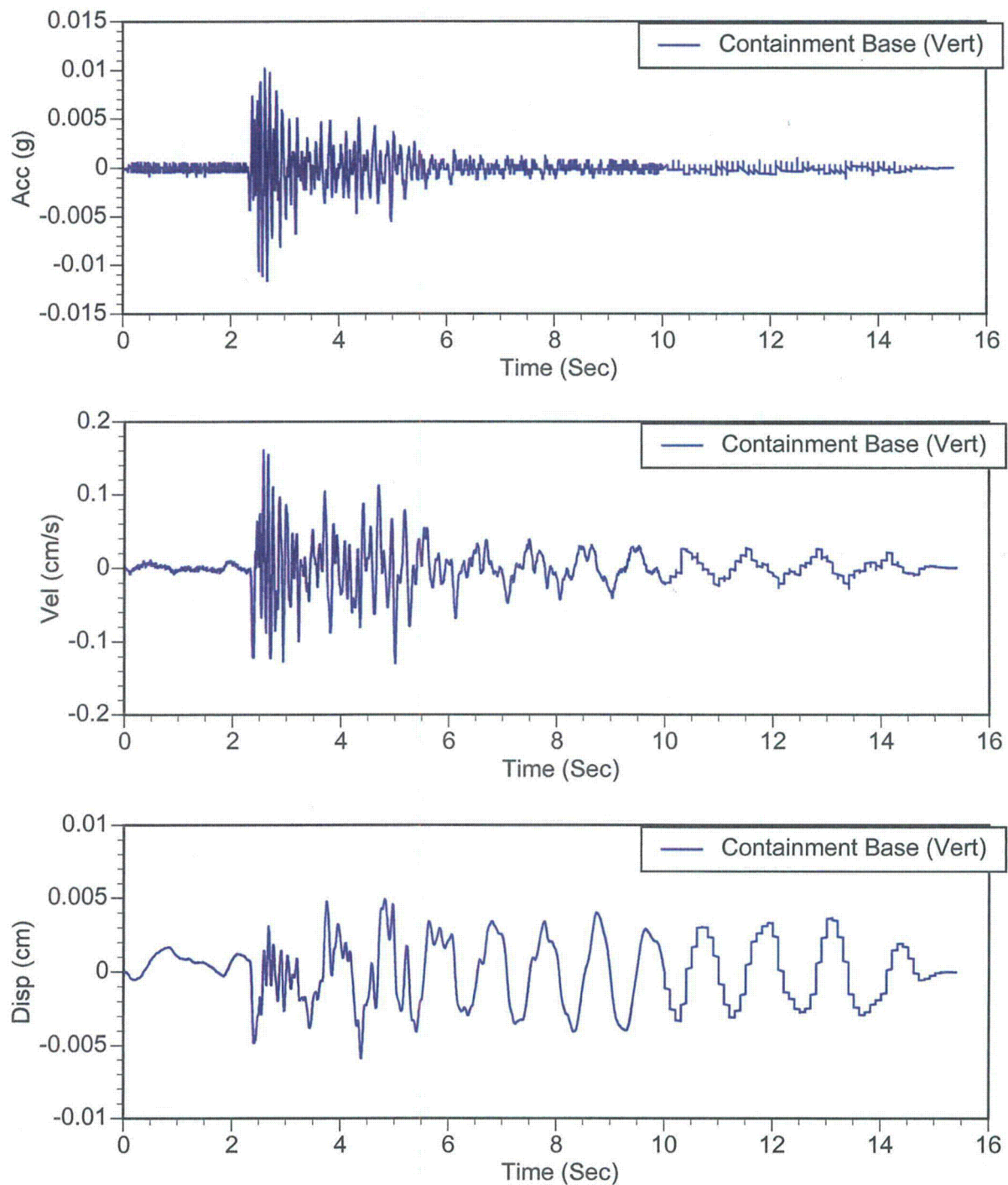
Figure 3c. Acceleration, velocity, and displacement for the vertical component (channel 2) of the free-field recording after filtering and baseline correction.

Figure 4a. Acceleration, velocity, and displacement for the horizontal 1 component (channel 1) of the unit 1 containment base recording after filtering and baseline correction. There is still some noise in the displacements at a frequency of about 1 Hz.

Figure 4b. Acceleration, velocity, and displacement for the horizontal 2 component (channel 3) of the unit 1 containment base recording after filtering and baseline correction. There is still some noise in the displacements at a frequency of about 1 Hz.

Figure 4c. Acceleration, velocity, and displacement for the vertical component (channel 2) of the unit 1 containment base recording after filtering and baseline correction. There is still some noise in the displacements at a frequency of about 1 Hz.
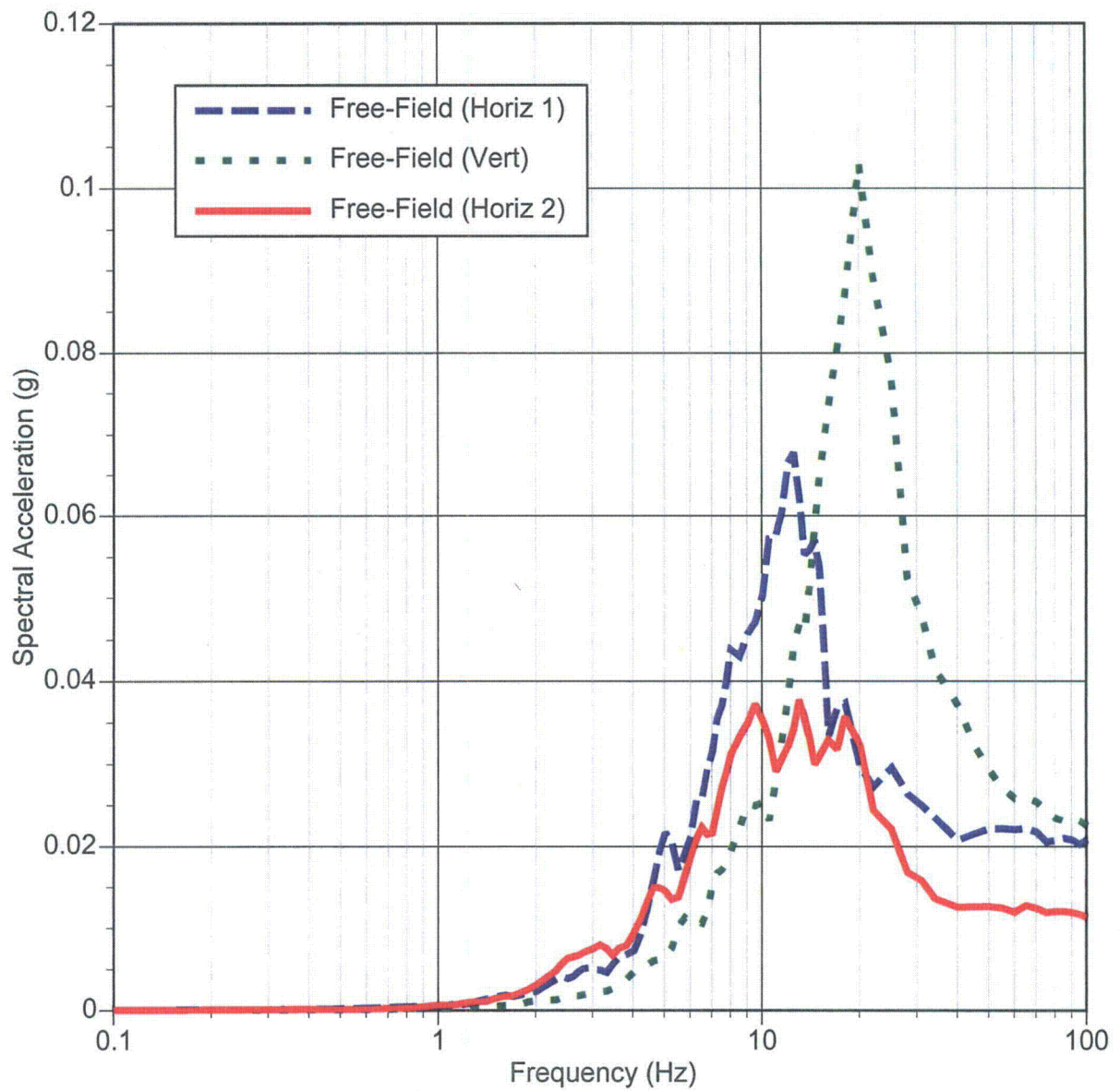
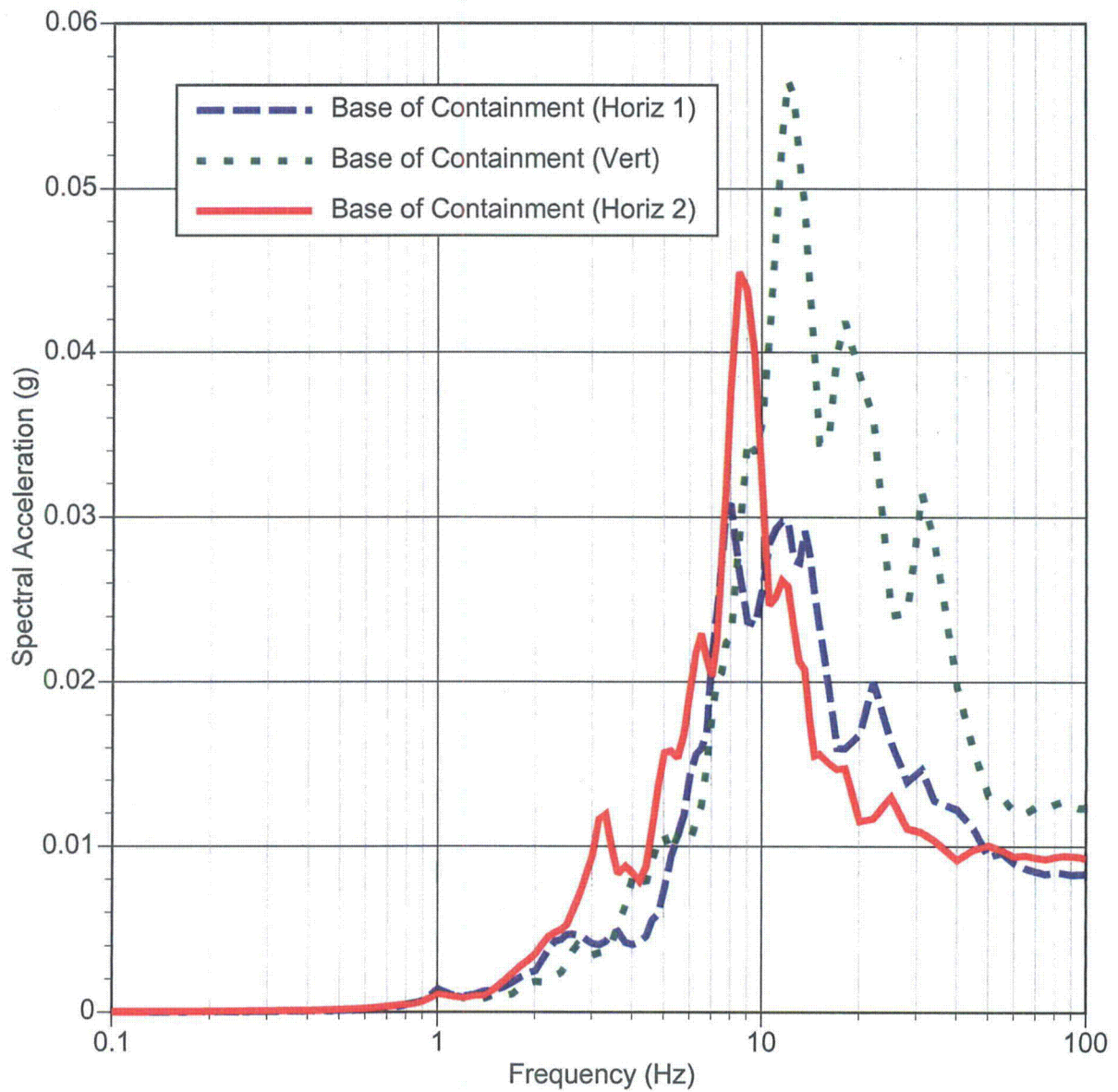Figure 5. Response spectra at 5% damping for the free-field ground motion.

Figure 6. Response spectra at 5% damping for the unit 1 containment base ground motion.
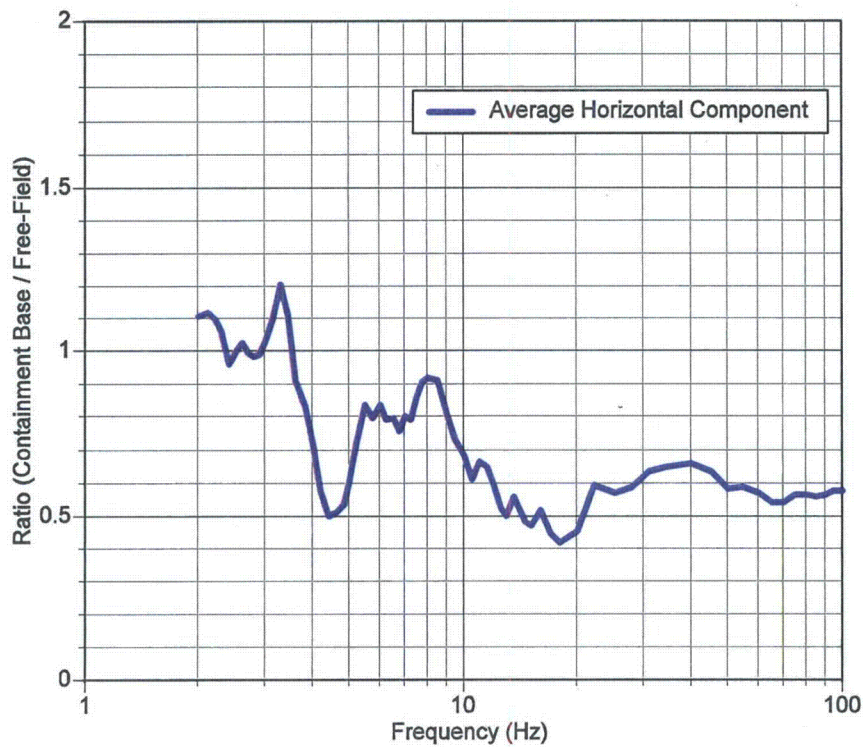
Figure 7. Response spectral ratio (5% damping) of the average horizontal component at at containment base of unit 1 to the free-field. The spectral ratio is only plotted for frequencies greater than 2 Hz because there is noise in the containment base recordings at frequencies less than 2 Hz.
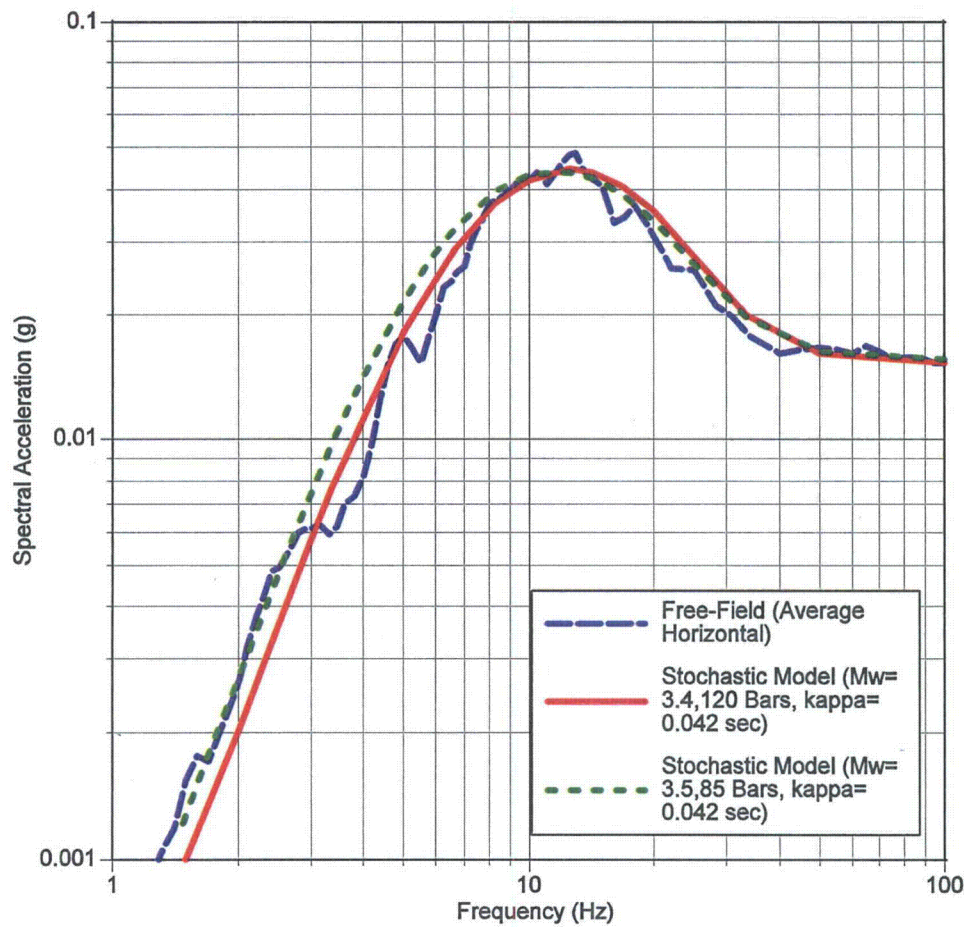
Figure 8. Comparison of the average horizontal response spectrum at 5% damping for the free-field recording with the expected California rock site spectrum from a moment magnitude 3.4 earthquake at a distance of 7.8 km with a stress-drop of 120 bars and kappa of 0.042 sec based on the stochastic point source model (red curve). The green curve shows the spectrum if the moment magnitude is 3.5 with a stress-drop of 85 bars.

Appendix L-2

San Simeon Earthquake of December 22, 2003

January 5, 2004

PG&E Letter No. DCL-03-184

U.S. Nuclear Regulatory Commission
ATTN: Document Control Desk
Washington, DC 20555-0001

Docket No. 50-275, OL-DPR-80
Docket No. 50-323, OL-DPR-82
Diablo Canyon Units 1 and 2
Special Report 03-04: San Simeon Earthquake of December 22, 2003

Dear Commissioners and Staff:

On December 22, 2003, at 1116 PST, with Unit 1 and Unit 2 operating at 100 percent power, a 6.5 magnitude earthquake occurred 11 km northeast of San Simeon, California. Ground motion was felt and recognized as an earthquake by the control room operators. The earthquake force monitor recorded greater than 0.01g for the seismic event. Operations personnel declared an Unusual Event at 1122 PST. (Reference NRC Event Notification Number 40408.) On December 23, 2003, at 1212 PST, the Unusual Event was terminated upon confirmation that no damage to the plant occurred.

This special report is submitted pursuant to Equipment Control Guideline (ECG) 51.1, "Seismic Instrumentation." This ECG requires the following actions for a seismic event: for seismic monitoring instruments actuated during a seismic event, "data shall be retrieved from actuated instruments and analyzed to determine the magnitude of the vibratory ground motion. A special report shall be prepared and submitted to the Commission … describing the magnitude, frequency spectrum, and resultant effect upon facility features important to safety."

Enclosure 1 describes the ground motion analysis including the magnitude and frequency spectrum of this event. Enclosure 2 provides an analysis of the resultant effect upon facility features important to safety.

As this event relates to the Diablo Canyon Power Plant, there was no adverse effect to public health and safety, or upon facility features important to safety.

If you have any questions, please contact me at 805-545-4600 or Mr. Lloyd Cluff at 415-973-2791.

A member of the STARS (Strategic Teaming and Resource Sharing) Alliance
Callaway • Comanche Peak • Diablo Canyon • Palo Verde • South Texas Project • Wolf Creek

Sincerely,

Lawrence F. Womack

SWH/A0597032
Enclosures

cc: Bruce S. Mallett, Region IV
David L. Proulx, Resident
Girija S. Shukla, NRR
Diablo Distribution

San Simeon Earthquake of December 22, 2003

Introduction

On December 22, 2003 at 1116 PST a strong earthquake of moment magnitude (M_W) 6.5 struck the central coast region. The earthquake, called the San Simeon Earthquake, was located approximately 50 km NNW of Diablo Canyon Power Plant (DCPP), in the region 11 km northeast of San Simeon, at a depth of about 7 km. The San Simeon Earthquake is the largest earthquake measured in the San Simeon region. The second largest earthquake in this region was the 1952 Bryson Earthquake of local magnitude (M_L) 6.2, approximately 8 km north of the 2003 epicenter. The San Simeon Earthquake was widely felt from Los Angeles to San Francisco. Earthquake ground effects included landslides and related ground failure near the epicenter, however no surface faulting was observed. Most of the damage occurred in Paso Robles, 39 km ENE of the epicenter. Two deaths have been confirmed due to a building collapse. The earthquake was also strongly felt at DCPP in the Administration Building and the Control Room. Strong motion instruments at the plant site were triggered.

The main shock initiated a rupture at a depth to the southeast and triggered a vigorous aftershock sequence that extends about 30 km southeast of the main shock. As of December 26, 2003, approximately 960 aftershocks have occurred, including about 120 magnitude (M) 3 events and 19 M 4 earthquakes. During the first 24 hours, the activity was about 50 percent higher than the average for a California sequence according to the US Geological Services online report, December 24, 2003, (http://www.usgs.gov/).

The San Simeon Earthquake was a reverse fault event beneath the Santa Lucia Mountains. It occurred along a NW-SE trending fault plane that dips either to the SW or NE. This is a common fault mechanism along this trend. (Reference 1).

Figure 1 shows the location of the main shock and first 20 hours of aftershocks. There is concentrated activity near the main shock and at the southeast end of the aftershock zone. Most of the aftershocks near the main shock are located between the Oceanic and Nacimiento fault zones, whereas the earthquakes to the southeast are not as constrained by the faults. It is not clear which fault, if either, was the cause of the earthquake. The aftershock patterns in depth view (Figure 1, cross sections AA' and BB') show diffuse activity above the main shock and no obvious fault plane. The closest distance from the aftershock zone to DCPP is about 38 km.

Strong Ground Motion

The main shock was felt in the Units 1 and 2 Control Room. It triggered the basic seismic system analog recorder (Kinemetrics SMA) in the Control Room and the Kinemetrics digital recorders (SSA) at the Unit 1 containment base, top of containment, the Auxiliary Building, and the free field pit locations (near the Fitness Trailer). The supplemental system was out of service at the time of the earthquake, however, three temporary accelerometers located in the Auxiliary and Turbine Buildings and a

1

permanent instrument in the basement of the 500 kV Switching Center triggered. The supplemental system is currently inoperable and replacement parts are obsolete; both the basic and supplemental systems are scheduled to be replaced in January 2004 with new instrumentation.

The earthquake force monitor (EFM) located in the control room measured 0.04g on the horizontal component. The EFM measurement is from the sensor at the Unit 1 containment base and does not have the baseline drift removed. With the baseline shift removed (but prior to filtering), the peak acceleration on the horizontal component is 0.042g. Table 1 lists the peak accelerations, peak velocities and peak displacements of the free-field and Unit 1 containment base ground motions after filtering and baseline corrections are applied. The peak accelerations range between 0.02g and 0.05g, with the largest peak acceleration in the free field, horizontal 2 direction.

Regarding the frequency spectrum, the response spectra were computed for the free-field and Unit 1 containment base recordings. The 5 percent damped spectra for the free-field and Unit 1 containment base recordings are shown in Figures 2 and 3, respectively. The response spectra for this earthquake show a typical spectral shape for rock sites.

For the free-field, both horizontal spectra and the vertical spectra peak at 4 to 5 Hz. These peaks of the free-field spectra are lower than expected for a magnitude 6.5 reverse earthquake recorded at 38 km distance. Current attenuation relations for rock site yield median horizontal spectral accelerations that are 1.5 to 2 times larger than the recorded free-field spectra. For the Unit 1 containment base, the spectra peak at 3 to 4 Hz for all three components. The containment base spectra show amplification in this 3 to 4 Hz range as compared to the free-field spectra. At short frequencies (< 2 Hz), the spectra from the containment base are similar to the free-field spectra. At high frequencies (e.g. 10 Hz), the horizontal spectra from the containment base are smaller than the free-field spectra.

Conclusions

The San Simeon Earthquake is the largest measured in the San Simeon region. The reverse fault motion of the main shock and aftershocks and the aftershock patterns are consistent with previous seismic activity in this region. The free-field ground motions recorded at DCPP are below then median ground motion estimated for this event using current attenuation relations for rock sites.

Dr. Norman Abrahamson and Ms. Marcia McLaren of PG&E Geosciences Department are preparing a detailed report of the San Simeon earthquake. The report will include analyses of the Kinemetrics SMA tape system. The detailed report will be available upon request

2

Reference

(1) McLaren, M. K. and Savage, W. U. (2000). Seismicity of South-Central Coastal California: October 1987 through January 1997, *Bull Seism. Soc. Am.* 91, no. 6, pp. 1629-1658.
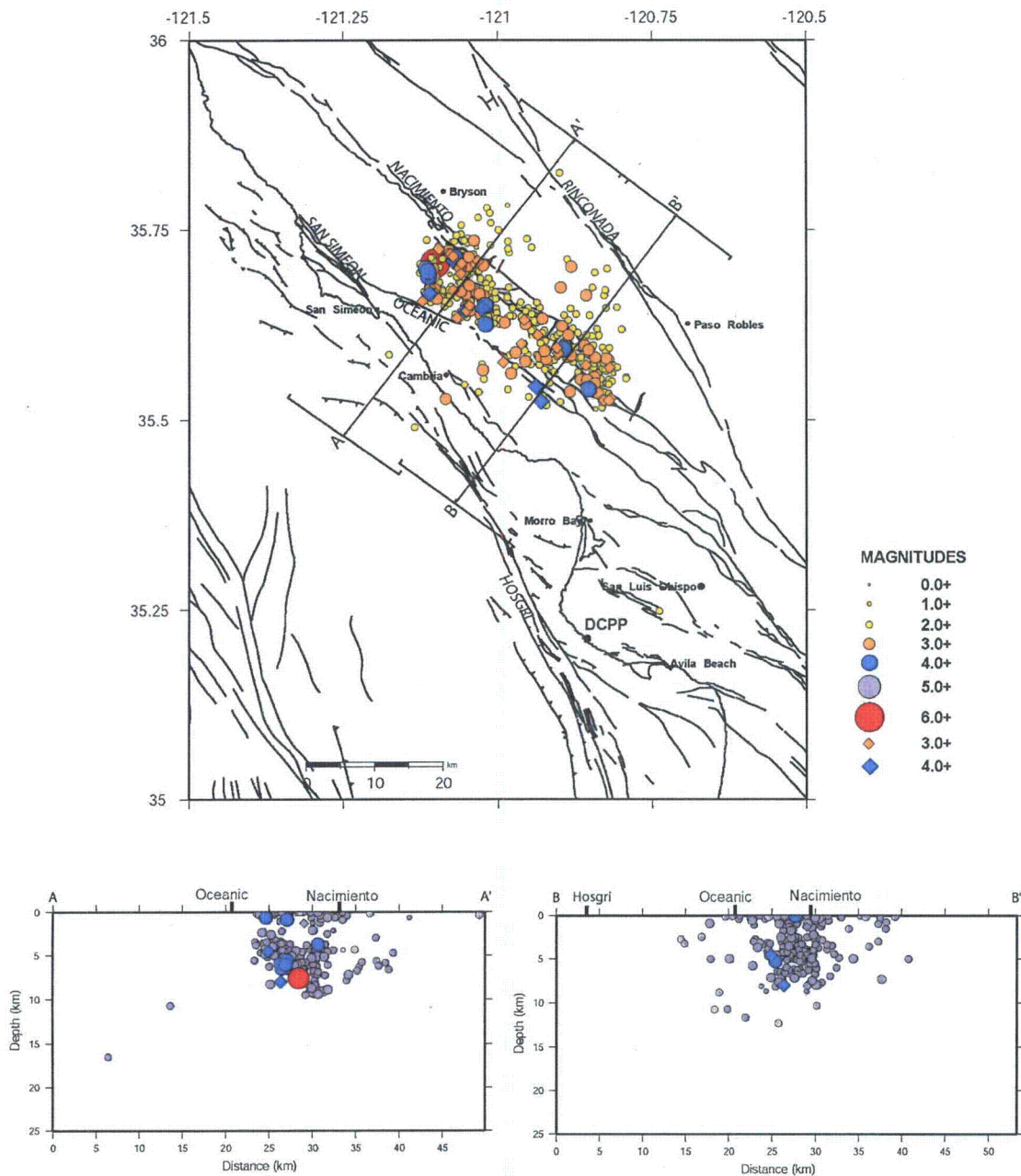
3

Figure 1. San Simeon Earthquake (large red circle) of 22 December 2003, 19:15 GMT, and aftershocks to 23 December 2003, 14:51 GMT. Nearby faults are labeled. Diamond earthquake symbols are preliminary locations form the USGS website; circles are events that have been reviewed by USGS seismologists NCEDC. Seismicity cross sections AA' and BB' are also shown.

4
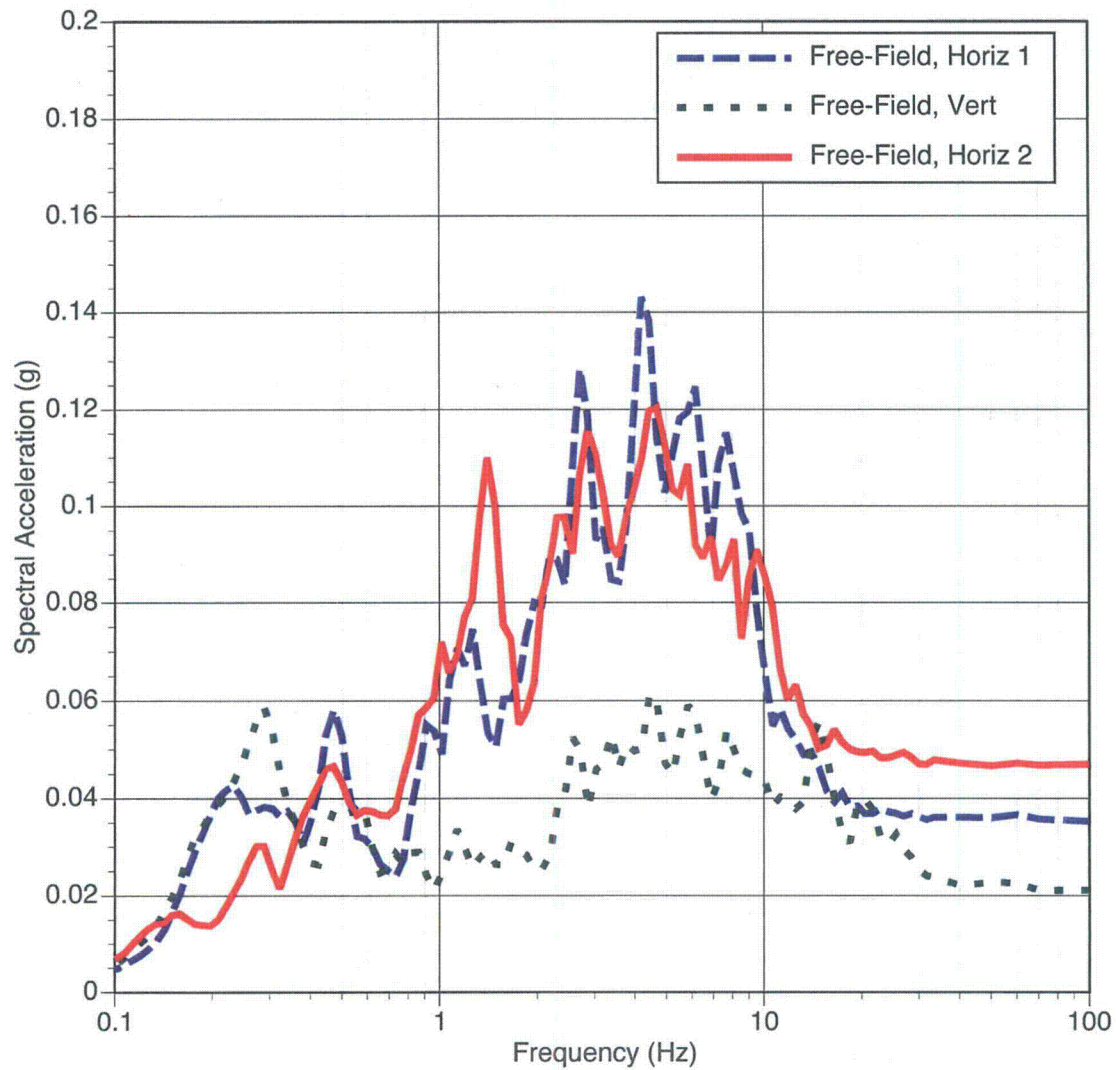
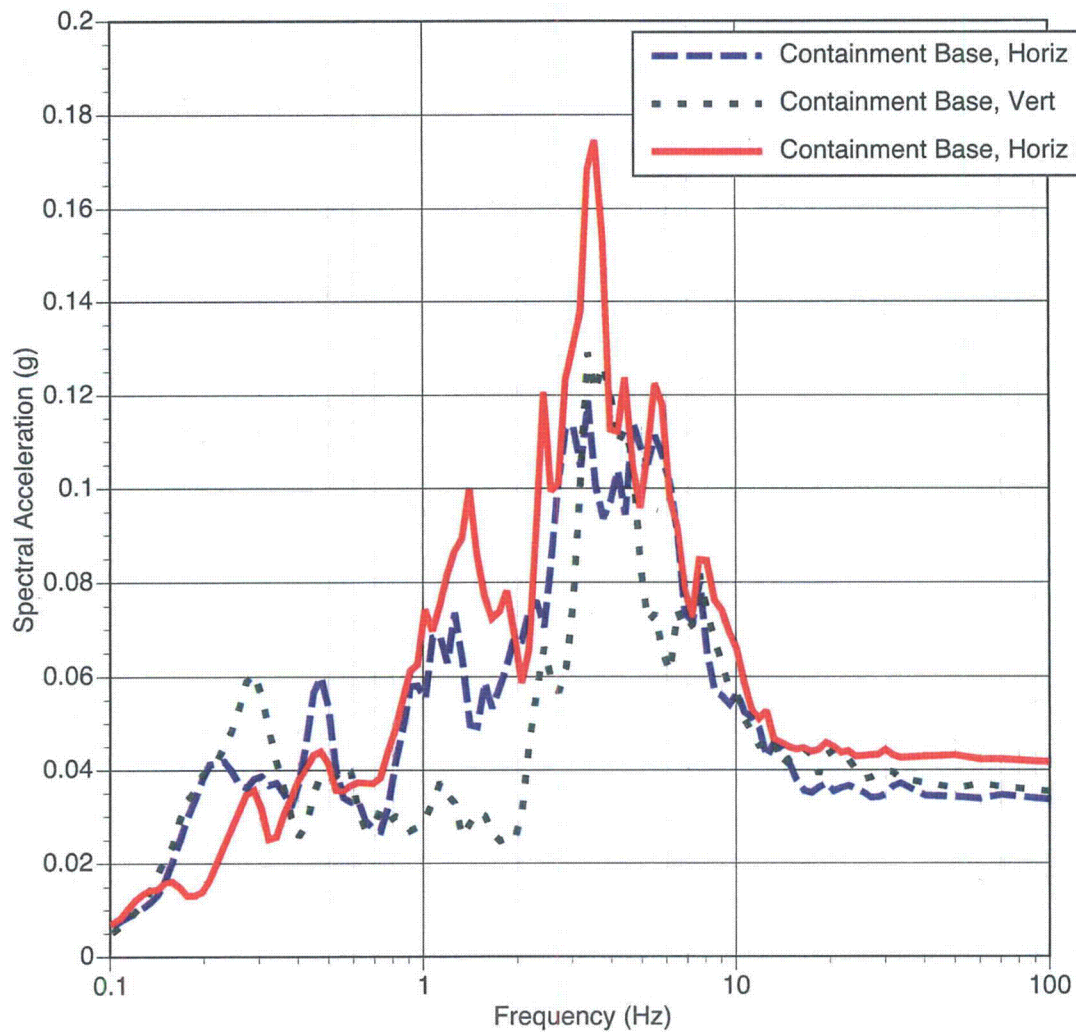Figure 2. Response spectra at 5% damping for the free-field ground motion.

Figure 3. Response spectra at 5% damping for the unit 1 containment base ground motion.

**Analysis of The Resultant Effect Upon Facility Features Important To Safety For
The San Simeon Earthquake of December 22, 2003**

Plant Systems Response:

The San Simeon Eearthquake registered 0.04g at the plant site, as read by the earthquake force monitor (EFM). The duration of the main shock was approximately 22 seconds. During this time, numerous alarms were received on both units. Many of the alarms were associated with movement of fluid levels in various systems. When the seismic activity stopped, the alarms that were received cleared and returned to normal. Operations responded by dispatching people into the power plant to visually verify systems that had received level alarms. Examples of the level alarms include; spent fuel pools, electro-hydraulic (EH) control system, and startup transformer 1-1. Operations took action to restore the operation of the Unit 2 EH pumps that had tripped off line due to a low-low system level lockout. This low-low system level lockout was due to the motion of the EH fluid; there were no leaks from the system. All other investigations to alarms revealed no leakage from systems and no damage caused by the earthquake. It was noted that the seismically-induced wave action in the Unit 1 spent fuel pool was of sufficient magnitude to cause a small amount of water to splash up onto the surrounding deck of the pool. Plant personnel were dispatched to clean this area.

Per Casualty Procedure (CP) M-4, "Earthquake," a walkdown of the facility was conducted. All systems continued to operate normally. No visible damage was discovered. Operations personnel performed inventory checks required by CP M-4; no systems were found to be leaking as a result of the earthquake. DCPP Fire Department personnel conducted plant walkdowns, including both containment structures to verify the continued integrity of fire protection features. No observable damage was discovered within the power plant and containment structures. No fire protection impairments were found. Operations personnel also performed an inventory of the diesel fuel oil storage tanks. No abnormalities were observed.

Seismic Monitoring Instrumentation Response:

The main shock triggered the basic seismic system analog recorder (Kinemetrics SMA) in the Control Room and the Kinemetrics digital recorders (SSA) at the Unit 1 containment base, top of containment, the Auxiliary Building, and the free-field pit locations (near the Fitness Trailer). The supplemental system was inoperable at the time of the earthquake, however, three temporary accelerometers located in the Auxiliary and Turbine Buildings and a permanent instrument in the basement of the control room at the 500 kV Switching Center triggered. The EFM located in the Control Room measured 0.04g on the horizontal component

All functional seismic monitoring instrumentation operated as designed.

1

OUTGOING CORRESPONDENCE SCREEN
(Remove prior to NRC submittal)

Document: PG&E Letter DCL-03-184

Subject: Special Report 03-04: San Simeon Earthquake of December 22, 2003

File Location: S:\RS\RA\Report\Specials\DCL03184 Special Report 12.22.2003
                Earthquake.doc

FSAR Update Review
Utilizing the guidance in XI3.ID2, does the FSAR Update need to be revised?   Yes [ ]   No [x] If "Yes", submit an FSAR Update Change Request in accordance with XI3.ID2 (or if this is an LAR, process in accordance with WG-9)

Commitment #1:   NONE

Clarification:

Appendix L-3

Mw 6.0 Parkfield Earthquake of September 28, 2004

Mw 6.0 Parkfield Earthquake of 28 September 2004
Preliminary Report by Geosciences Department, PG&E

A (Mw 6.0) earthquake occurred Tuesday, September 28, 2004 at 10:15:24 PDT at a depth of 8 km (5 miles) near Parkfield, California (Figure 1). This is the long-awaited Parkfield earthquake. It is the seventh in a series of repeating earthquakes that have occurred on the Parkfield section of the San Andreas fault at fairly regular intervals in 1857, 1881, 1901, 1922, 1934, and 1966. The first in 1857, was a foreshock to the great Fort Tejon earthquake (Mw 7.9), which ruptured the fault from Parkfield to the southeast for over 180 miles. In 1984 the USGS "predicted" the next Parkfield (M 6.0) earthquake would take place within the time window of 1988 to 1993, therefore, the September 28 earthquake was at least ten years behind the expected occurrence. The six (M6.0) earthquakes are termed "characteristic" because they all ruptured the same area on the fault and were about the same magnitude. This September 28 earthquake ruptured the same region as the 1966 event and fits the description of a characteristic Parkfield earthquake. Strong shaking lasted about 10 seconds. The aftershocks extend along the San Andreas fault from 5km SE of the epicenter to about 25 km NW of the epicenter, at the SE end of the creeping (aseismic) section of the fault.

The 2004 earthquake was located by the California Integrated Seismograph Network (CISN) at 35.815N, 120.374W. This location is 7 miles SSE of Parkfield, and 50 miles NE of DCPP (Figure 1 inset). As of October 5, over 900 aftershocks have been recorded, including two M5 and five M4 events. The two M5.0 events occurred on 9/29 at 10:19 PDT and on 9/30 at 11:54 PDT at about 10 km depth. Both locate to the northwest, 12 and 15 miles, respectively, from the main shock. The CISN focal mechanisms from the main shock and aftershocks indicate the events occurred on a northwest trending right-lateral strike-slip fault (Figure 2), consistent with motion along the San Andreas fault. Surface rupture of a few cms has been observed at various locations along the fault between the section of the fault 15 km SE of the epicenter to 20 km NW of the epicenter near the 9/29 M5.0 aftershock (Figure 1).

Figure 3 shows maps of the shear stress calculations for the 1983 Coalinga earthquake (Mw 6.2) and the 2003 San Simeon earthquake (Mw 6.5). These results suggest that the Coalinga earthquake may have retarded the Parkfield earthquake (Parkfield section in blue, low shear stress zone), while the San Simeon earthquake may have ratcheted up the stress at Parkfield 9 months ago (Parkfield section in red, high stress change zone; Ross Stein, personal communication).

The earthquake was strongly felt in the Parkfield area. No deaths or injuries have been reported to date. The San Miguel Substation was the closest PG&E facility to the event, 18 miles to the west. No damage was reported. Figure 1 shows that the 500 kV and 230 kV electric transmission lines and the line 306 Gas transmission line cross the fault within about 5 km of the epicenter. PG&E made field checks and no damage was reported. The earthquake was felt at DCPP (eg. the Administration building), but was not felt in the control room at the site. The newly installed Consolidated Seismic System

recorded the earthquake on all 19 instruments. The data are summarized below in the Strong Motion section.

Strong Ground Motion

In anticipation of the Parkfield earthquake, this part of the San Andreas fault is particularly well instrumented due to the presence of the CISN Parkfield array (Figure 4). Consequently, there are many strong motion recordings of the earthquake. Although the aftershock patterns are predominantly from the epicenter to the NW, the recorded ground motions are highly variable, suggesting that slip along the fault was complex.

A key feature of the near-fault ground motions is the large variability: near the fault the average horizontal peak accelerations range from 0.1 to 1.3g. The closest station to the epicenter was about 3 km to the NW; it recorded 0.16 g. The highest acceleration of 1.3 g was at the northern end of the aftershock zone, north of Parkfield, about 15 km from the epicenter. Two additional stations recorded over 1 g ground motions, within 5 km of Parkfield. These recordings are near the location of the two M5 aftershocks. There also was unusually strong ground shaking recorded southeast of the epicenter, suggesting that the rupture was not unilateral. A peak acceleration of 0.85 g was recorded 9 km SE of the epicenter, less than 1 km from the fault, and two additional stations to the SE and E of the fault recorded accelerations of 0.84 g and 0.82 g.

The free-field peak accelerations recorded at DCPP are compared to other free-field peak acceleration in Figure 5. The distance from DCPP to the Parkfield rupture is about 85 km. This comparison shows that the peak accelerations recorded at DCPP are slightly smaller than other peak acceleration at similar rupture distances. Also shown in this figure are the peak accelerations predicted by the Abrahamson & Silva (1997) attenuation relation for a magnitude 6.0 strike-slip earthquake. Since all the site conditions are not currently available, both rock and soil attenuation relations are shown. Overall, the Abrahamson and Silva model is consistent with the observed PGA values, but it tends to overestimate the peak accelerations at large distances.

DCPP Strong Ground Motion
The main shock was felt in the DCPP Administration building and it triggered the newly installed Consolidated Seismic System (CSS). The location of the new CSS are listed in Table 1 and are shown in Figures 6 and 7.

The recordings were processed as follows:
1. Remove the baseline shift.
   The average acceleration over the first two seconds was used to remove the baseline shift.

2. Determine useable frequency band .
   The Fourier spectra of the recordings were computed. Based on the shape of the Fourier spectra, the reliable frequency band was estimated. For free-field recordings, high-pass corner frequencies of 0.1 Hz and 0.2 Hz were selected

for the horizontal and vertical components, respectively. For the in-structure recordings, high-pass corner frequencies of 0.2 Hz and 0.4 Hz were selected for the horizontal and vertical components, respectively. For all components, low-pass corner frequencies of 40 Hz were selected.

3. Apply a band-pass filter
   Using the corner frequencies identified in step 2, a band-pass filter is applied to each recording. A 5-pole Butterworth filter is used.

4. Apply baseline correction
   A baseline correction is applied to the band-pass filtered recordings. The displacement baseline is modeled using a high-order polynomial without the constant or linear terms.

5. Integrate to velocity and displacement
   The baseline corrected recordings are then integrated to velocity and displacement using a time domain integration. The normalized arias intensity (used to compute the duration) is also computed in this step.

6. Compute the response spectra
   In the final step, the response spectra at 5% damping are computed.

Table 1 lists the peak accelerations, peak velocities, and peak displacements of the recordings from the Consolidated Seismic System. The free-field ground motions had peak horizontal accelerations of about 0.006g to 0.011g after the baseline shift, filters, and baseline corrections are applied. The peak vertical accelerations on the free-field recordings were less than one-half of the average horizontal peak acceleration.

The acceleration, velocity, and displacement time series for the three-components of free-field station ESTA28 are shown in Figures 8-10. The normalized Arias intensity, shown in Figure 11, is used to evaluate the duration of the ground shaking. One common measure of duration is the time interval from the 0.05 to 0.75 level of the normalized Arias Intensity (called the 5-75% duration). For these recordings, the 5-75% duration corresponds to about 7 seconds.

The free-field response spectral values at frequencies greater than 1 Hz recorded at the DCPP site were factors of 2-3 lower than the median response spectral values computed for this earthquake using attenuation relations similar to those used in the LTSP (Figure 12). This is partly due to the general over-prediction of the ground motions at large distances by the attenuation relation and partly due to the larger than typical shear-wave velocities at DCPP (the DCPP site has a shear-wave velocity of 4500-5000 ft/s, but the attenuation relations used in the LTSP were based on ground motions primarily recorded on soft-rock and shallow soil sites with shear wave velocity of about 1500-2000 ft/s). Sites with larger shear-wave velocities tend to have smaller ground motions since there is less of an impedance contrast.

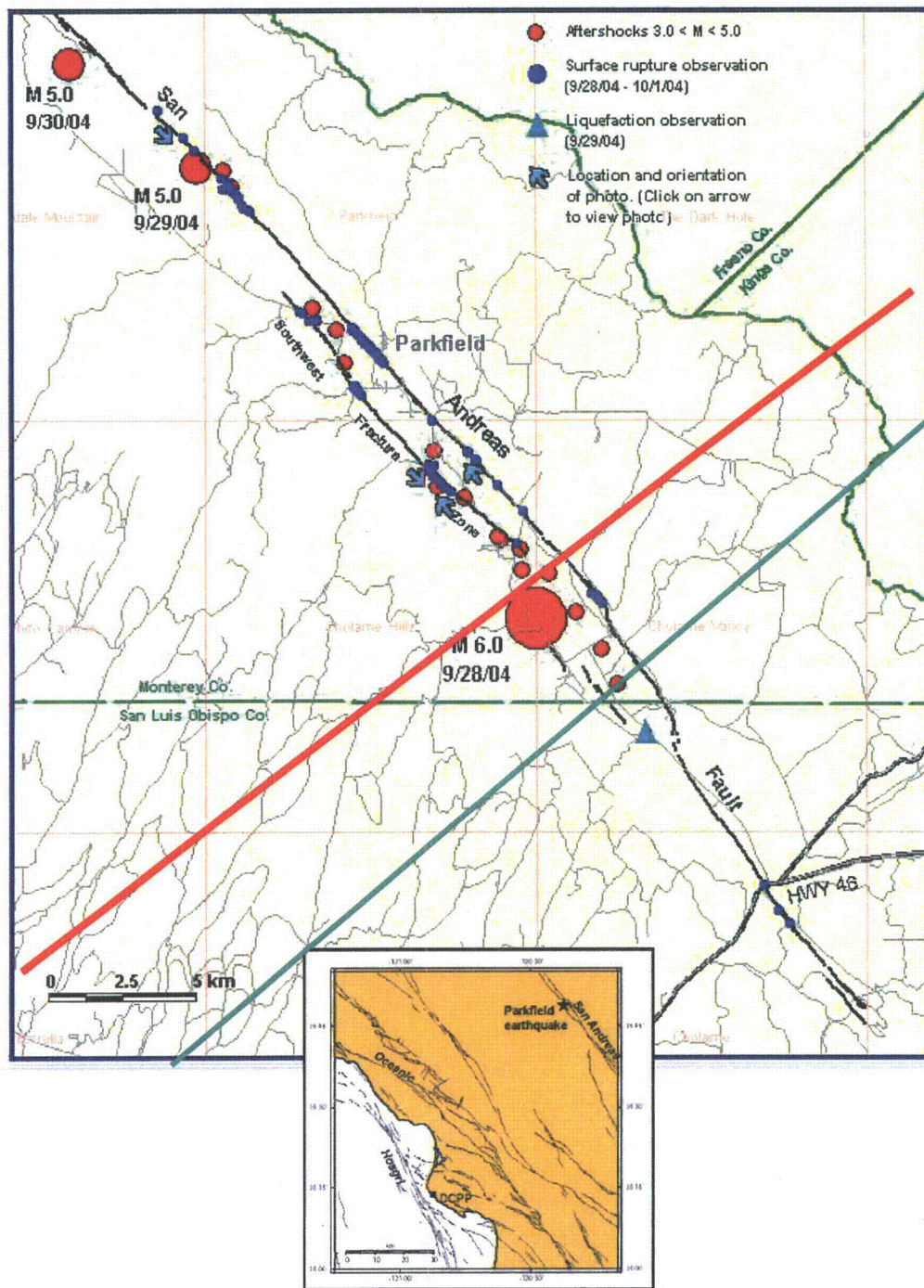The 5% damped response spectra for all the CSS recordings are shown in Figures 13 to 31.

Figure 1. Location of the September 28, 2004 Parkfield earthquake (Mw6.0). Also shown are M3 and greater aftershocks, surface rupture observations, and locations of the 500/230kV transmission lines (red line) and the Gas pipeline 306 (green line). Inset map shows earthquake with regional faults.
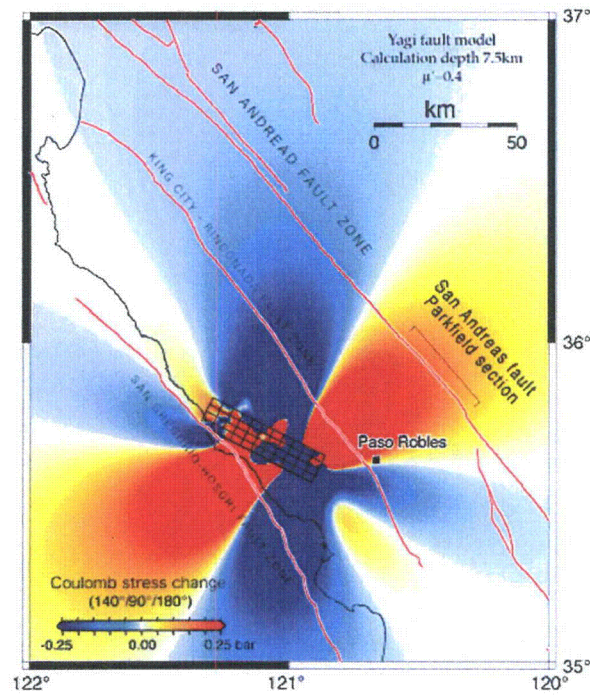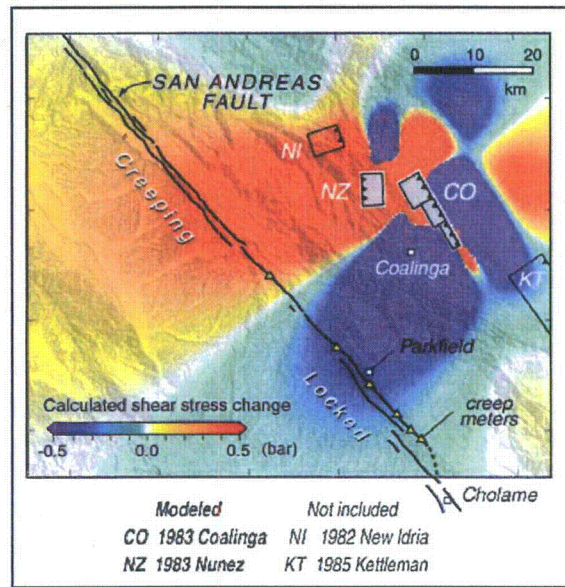
```
September 28, 2004 at 17:15:24 UTC ML=6.0; (USGS/UCB

Berkeley Moment Tensor Solution

Best Fitting Double-Couple:
    Mo = 9.82E+24 Dyne-cm
    Mw = 5.96
    Z  = 8. km


                      ------
              ------------ P ----
          ##------------      -------
          ####------------------------
        ######----------------------------
       ########----------------------------#
      ##########---------------------####
     ############-----------------#######
     #############--------------##########
    ###############,##----------#############
    ################-------###############
    #################-----################
    ##################--################
    ################----################ T
      #############--------################
      ##########------------###############
    #####----------------#############
       #----------------------###########
          ----------------------#########
          ----------------------######
          ----------------------`-##
             -------------------

              -------
```

Figure 2. USGS moment tensor focal mechanism for the Mw 6.0 Parkfield earthquake

Figure 3. Top figure is the calculated shear stress imposed by the 1983 Coalinga earthquake on planes parallel to the San Andreas fault at 8 km depth; bottom figure is calculated shear stress from the 2003 San Simeon earthquake. (Figures from Ross Stein, US Geological Survey, 10/7/04)

Figure 4. Location of the CISN strong motion instruments with corresponding peak horizontal ground motions. Values greater than 0.80g are circled. The heavy line shows the rupture dimension used for computing the rupture distances.
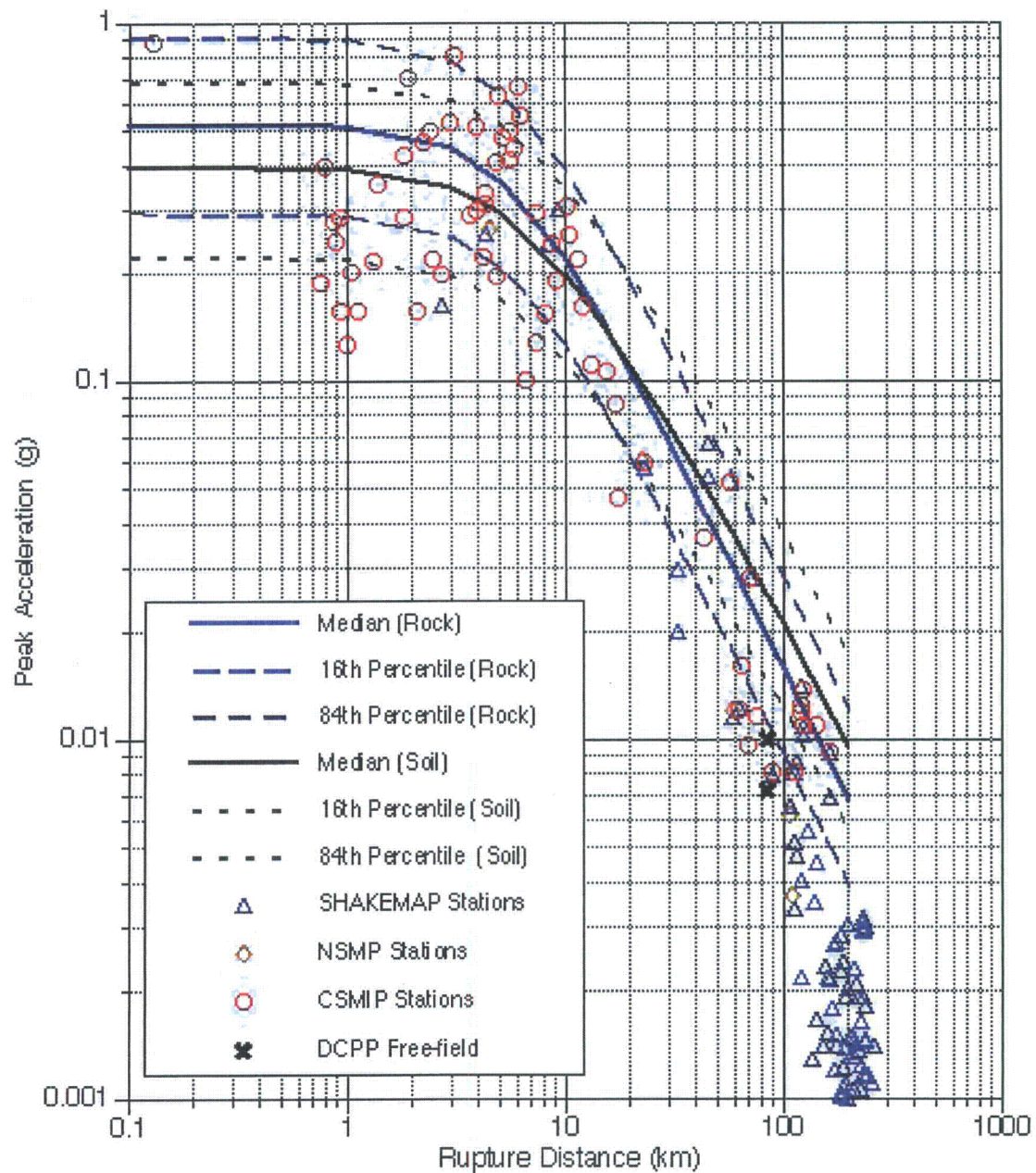
Figure 5. Peak accelerations for the average horizontal component recorded during the Parkfield earthquake compared with the Abrahamson and Silva (1997) attenuation relation. Both rock and soil curves are shown since the site classifications were not yet reviewed.
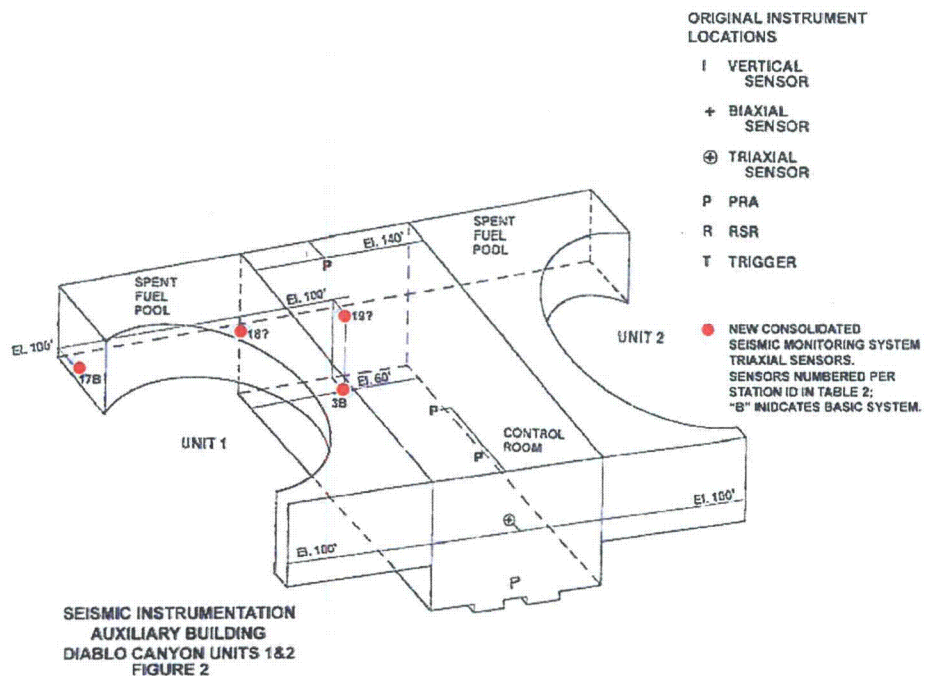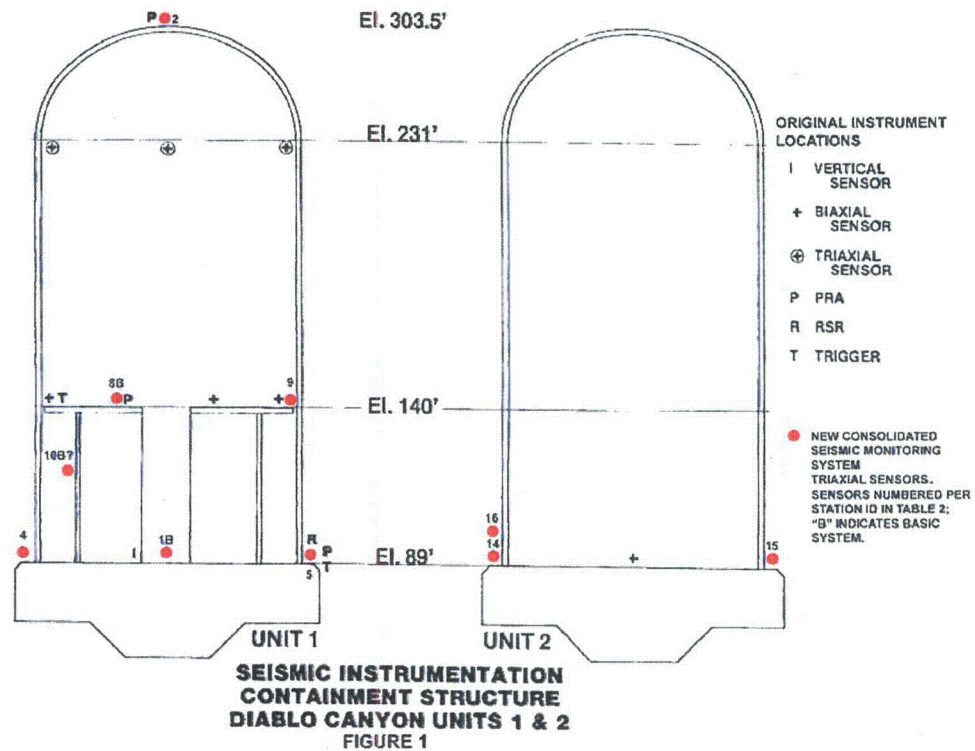
Figure 6. Location of Consolidated Seismic System instruments in Units 1 and 2
Containment (top) and Auxiliary building (bottom).

SEISMIC INSTRUMENTATION
TURBINE BUILDING
DIABLO CANYON UNITS 1 & 2
FIGURE 3

ORIGINAL INSTRUMENT LOCATIONS

I VERTICAL SENSOR

+ BIAXIAL SENSOR

⊕ TRIAXIAL SENSOR

P PRA

R RSR

T TRIGGER

● NEW CONSOLIDATED SEISMIC MONITORING SYSTEM TRIAXIAL SENSORS. SENSORS NUMBERED PER STATION ID IN TABLE 2; "B" INIDCATES BASIC SYSTEM.

ORIGINAL INSTRUMENT LOCATIONS

I VERTICAL SENSOR

+ BIAXIAL SENSOR

⊕ TRIAXIAL SENSOR

P PRA

R RSR

T TRIGGER

● NEW CONSOLIDATED SEISMIC MONITORING SYSTEM TRIAXIAL SENSORS. SENSORS NUMBERED PER STATION ID IN TABLE 2; "B" INIDCATES BASIC SYSTEM.

UNITS 1 AND 2
DIABLO CANYON SITE

SEISMIC INSTRUMENTATION

FIGURE 4

Figure 7. Location of Consolidated Seismic System instruments in Units 1 and 2 turbine building (top) and Free field (bottom).
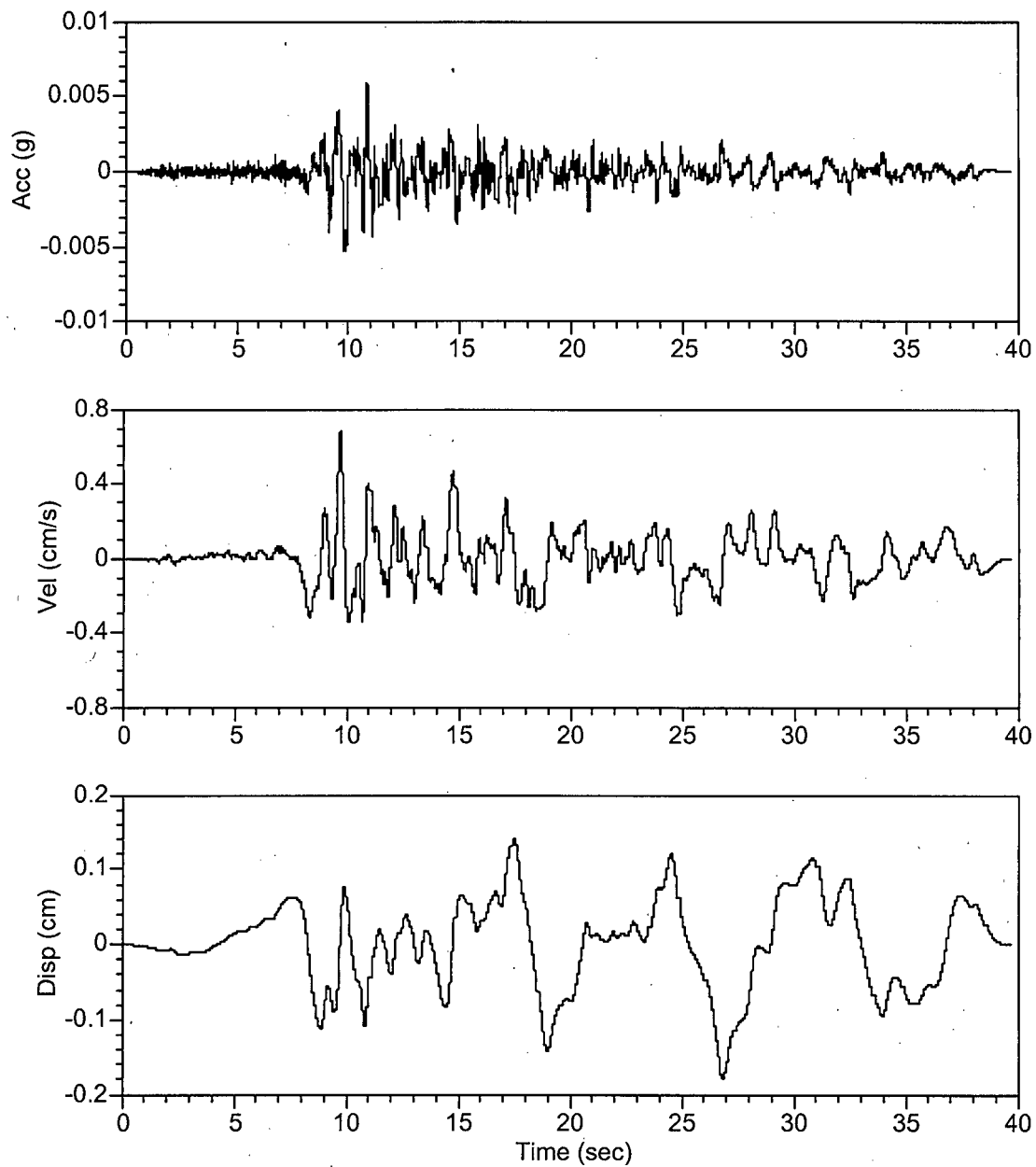
Figure 8. Free-field ground motions: ESTA28 X component (85' elev. Free Field in paved area north of U1 containment).
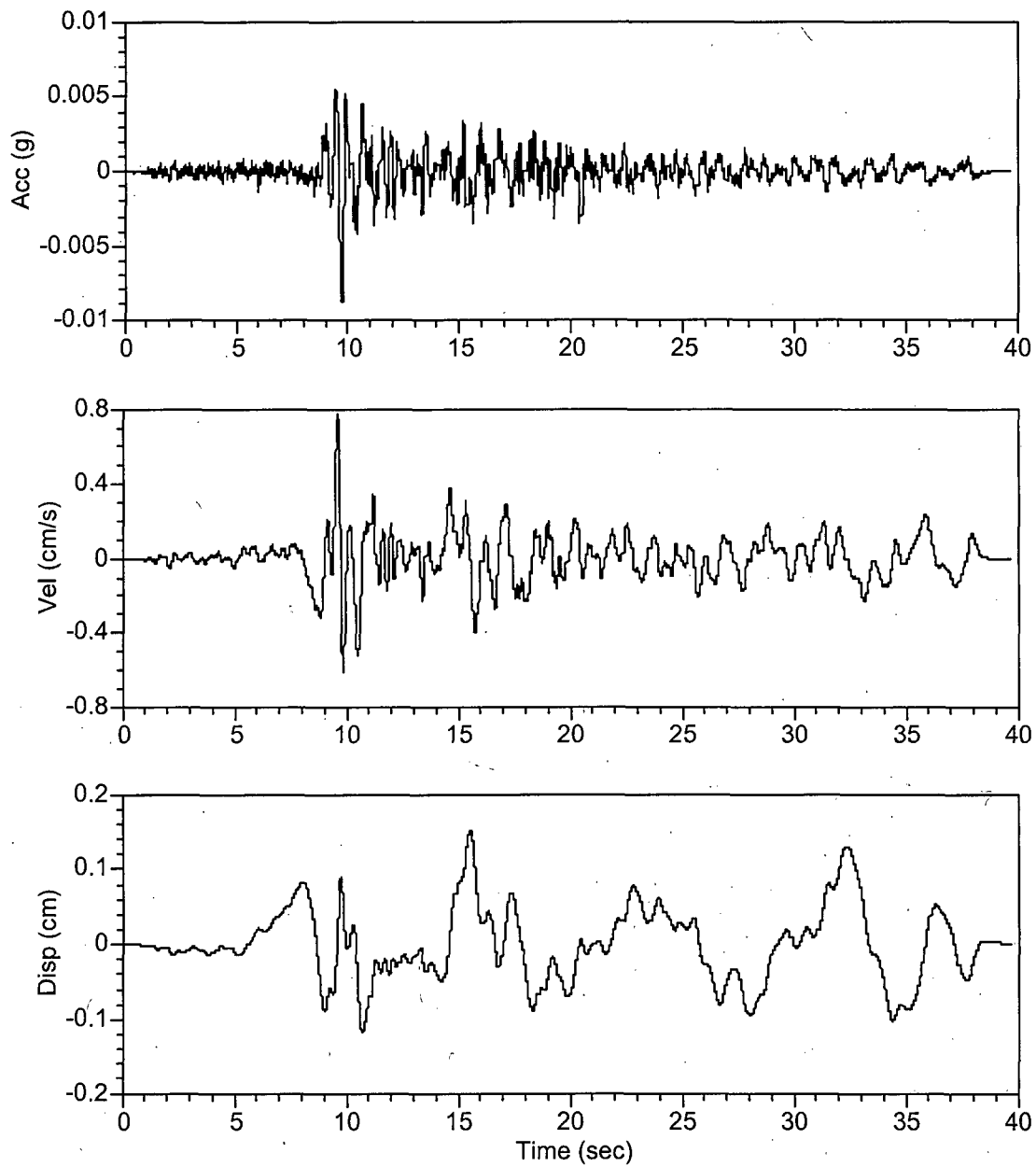
Figure 9. Free-field ground motions: ESTA28 Y component (85' elev. Free Field in paved area north of U1 containment).
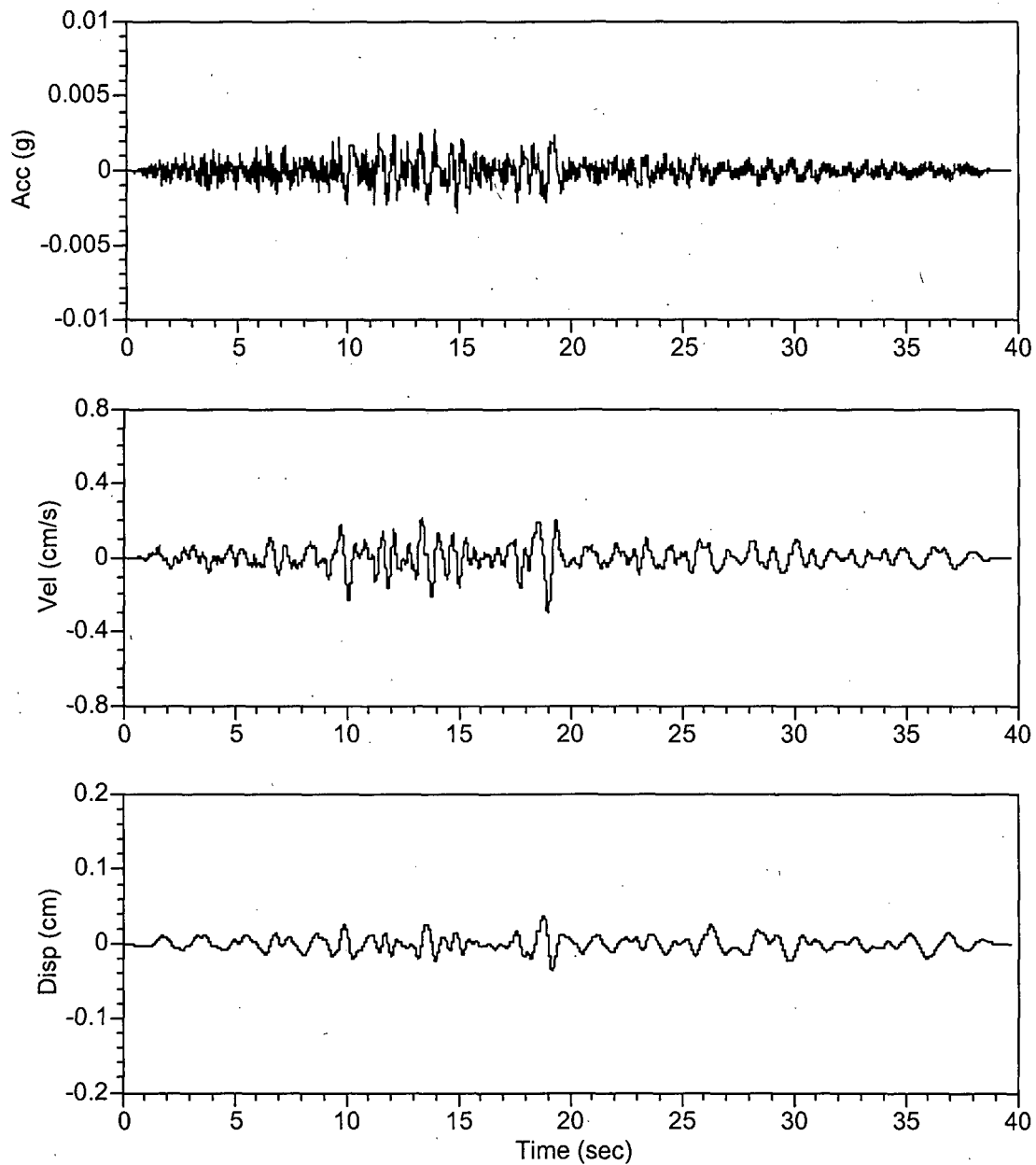
Figure 10. Free-field ground motions: ESTA28 Z component (85' elev. Free Field in paved area north of U1 containment).
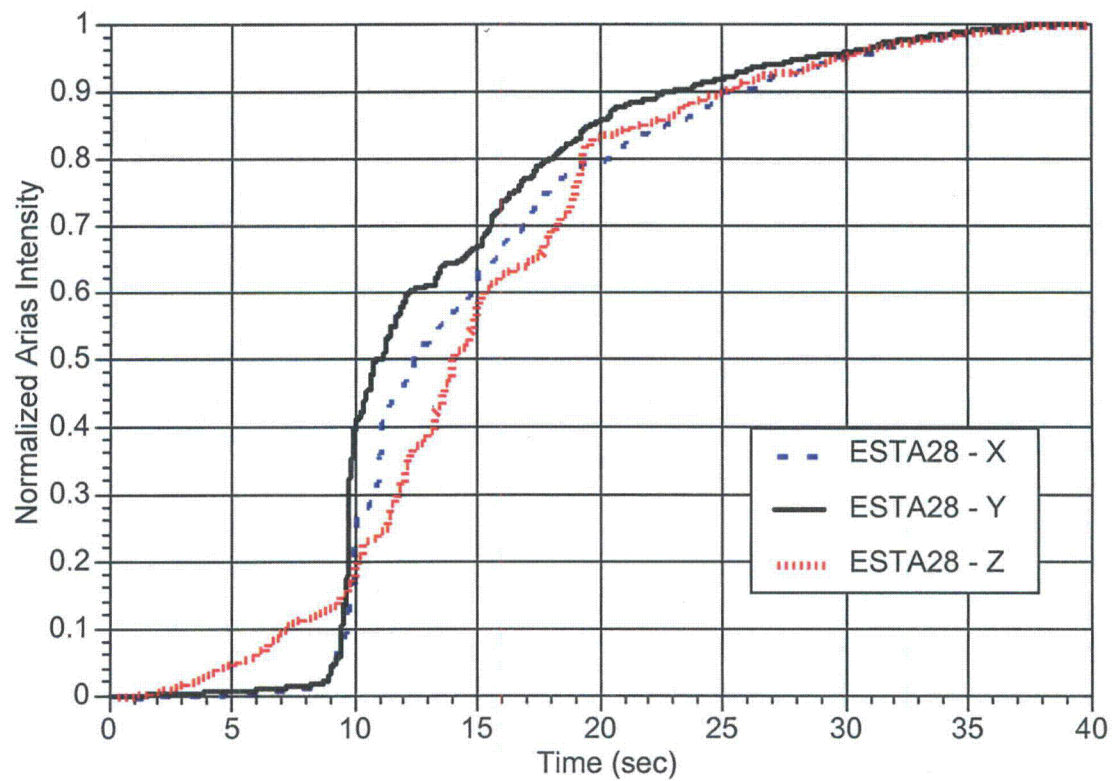
Figure 11 Acceleration normalized Arias Intensity from free-field station ESTA28. This shows the duration of the accelerograms.
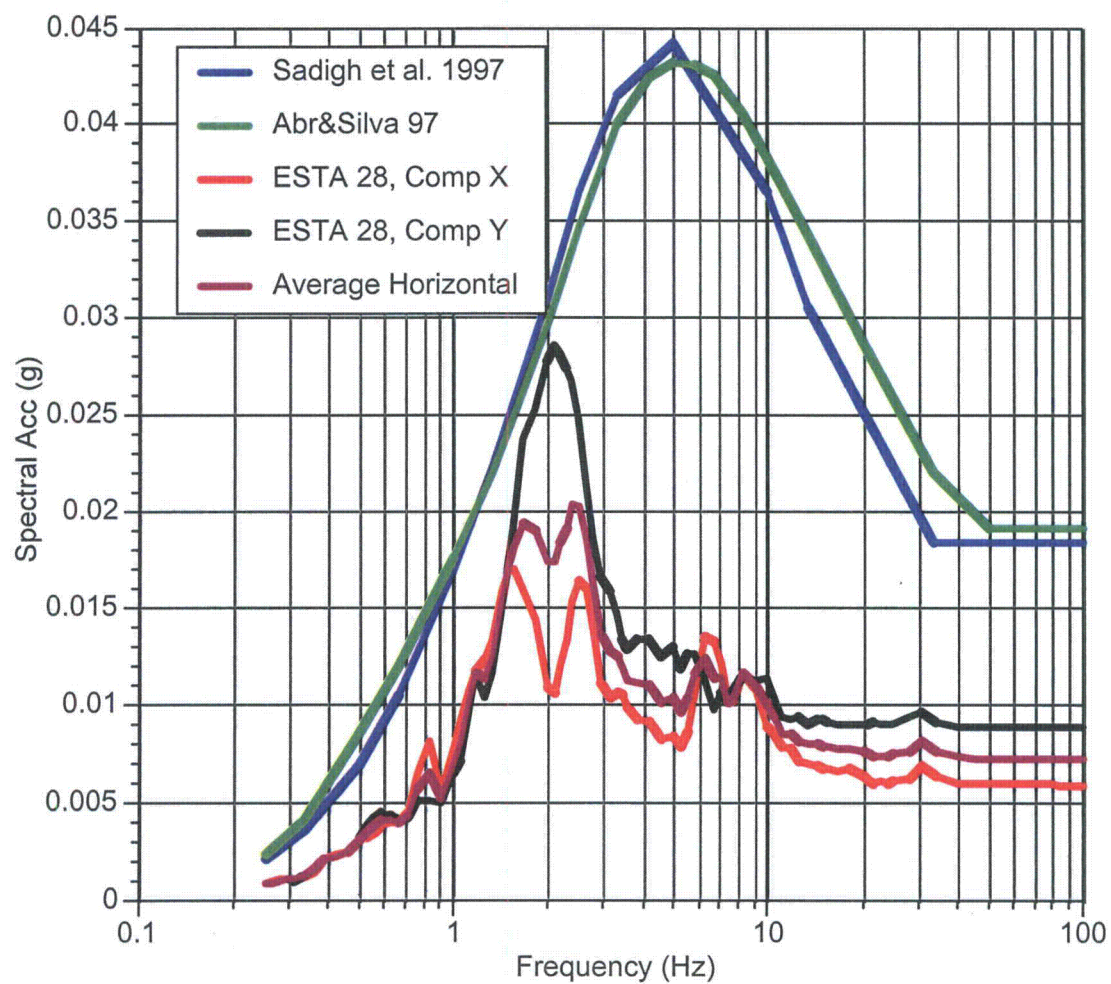
Figure 12. Comparison of free-field spectra from DCPP with those predicted from commonly used attenuation relations.

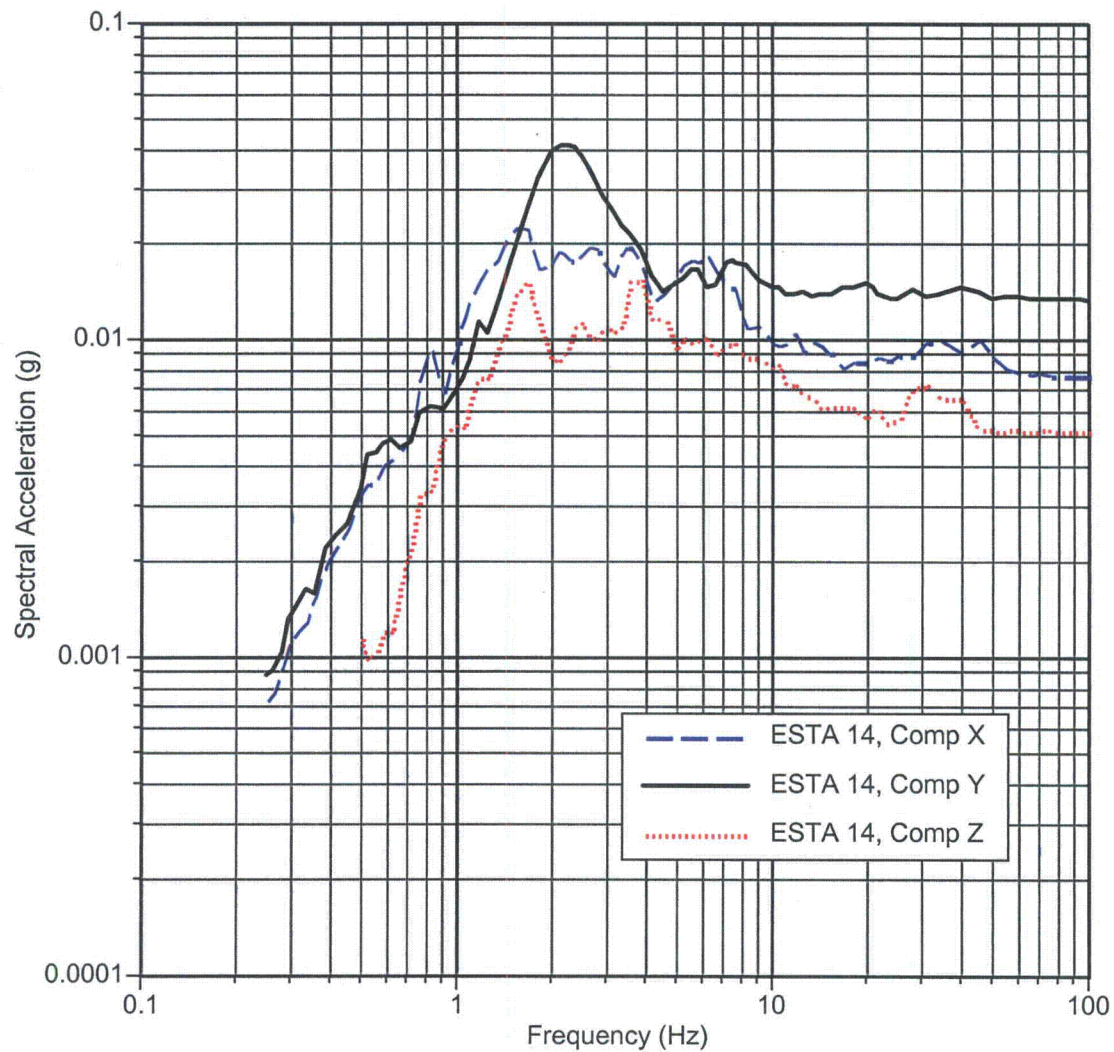DCPP: Station ESTA01, Parkfield EQ (09/28/04), Mw=6.0
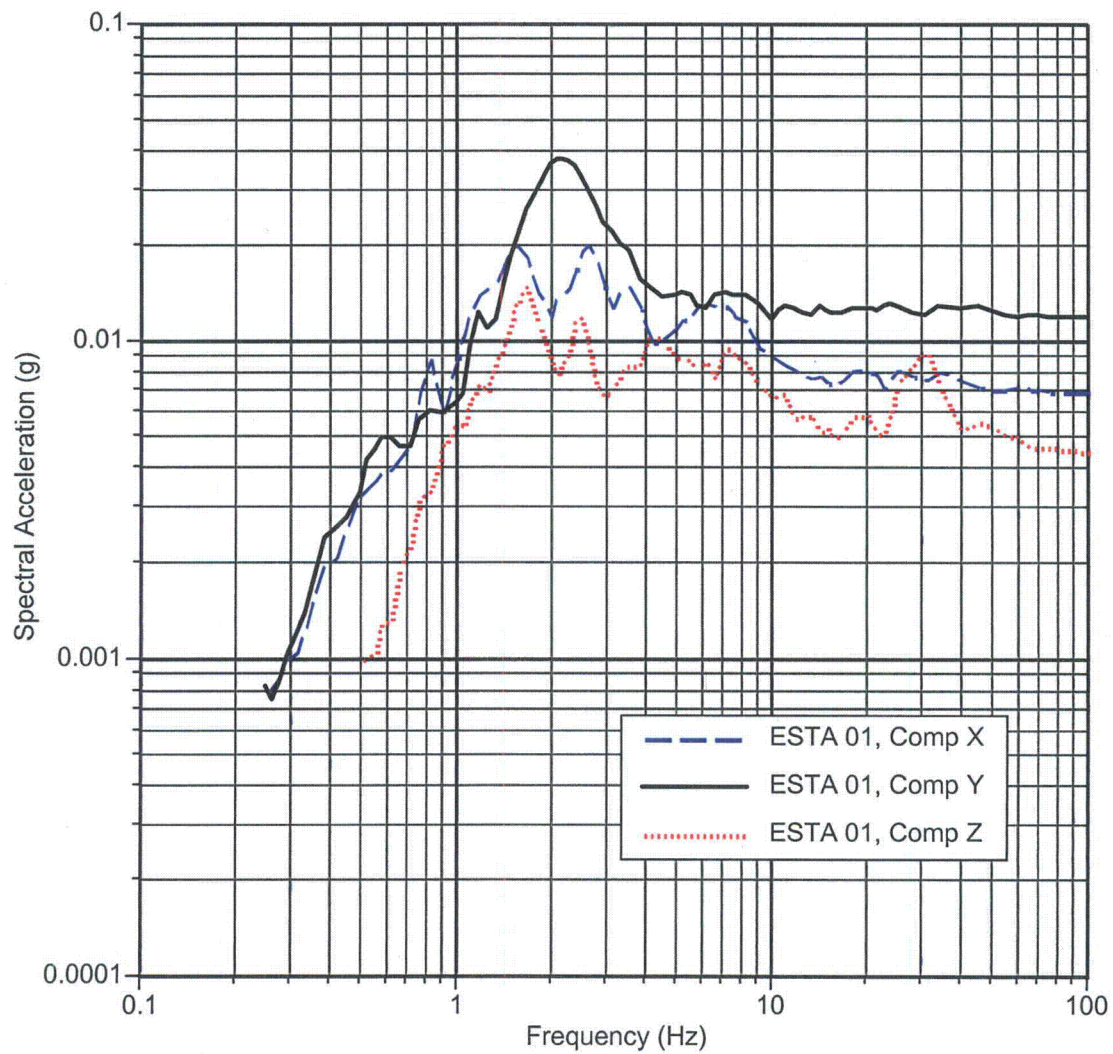
Figure 13. Response spectra at 5% damping for ESTA 01 (89', 180 degrees on containment Base Slab).
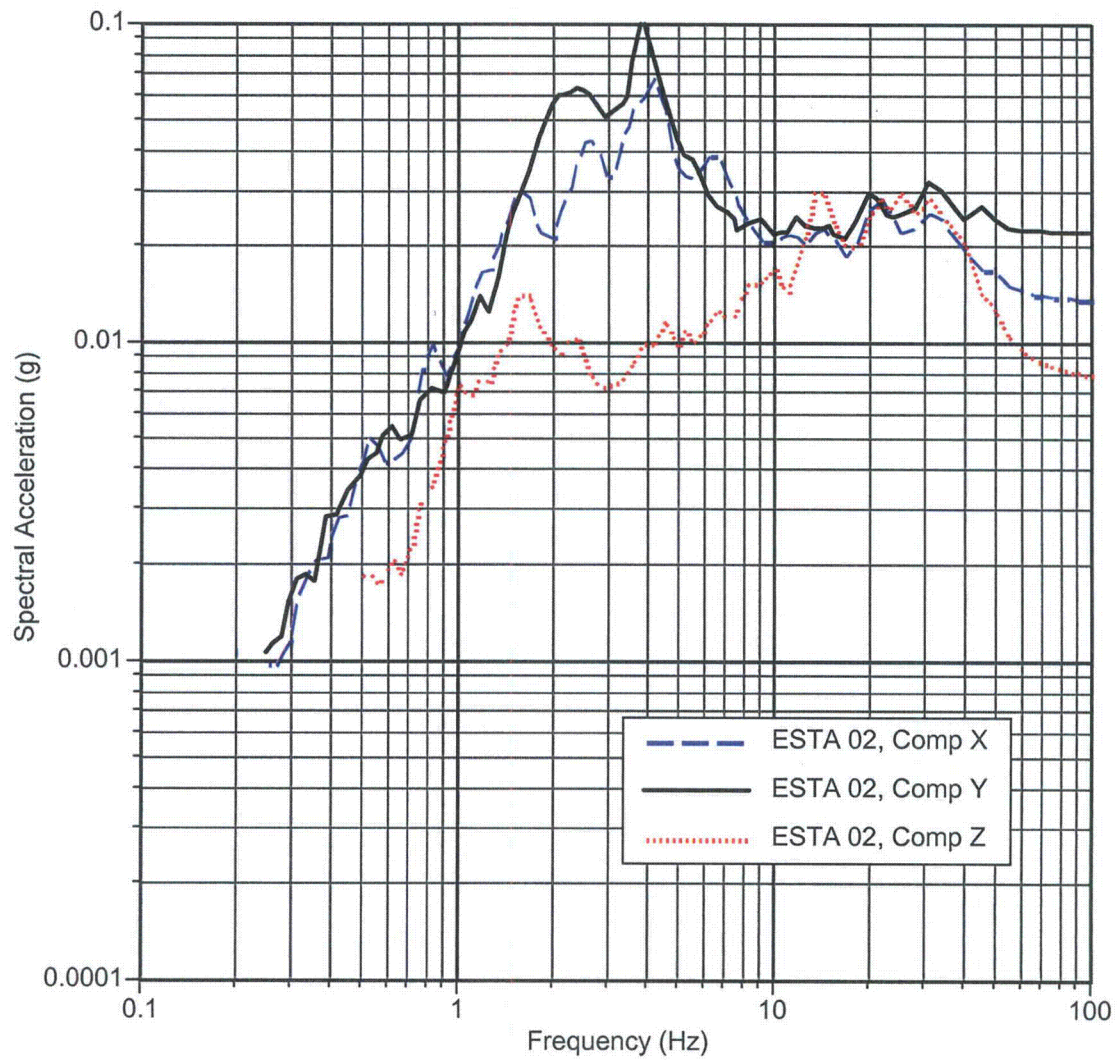
Figure 14. Response spectra at 5% damping for ESTA 02 (U1 303' elevation, 225 degrees).
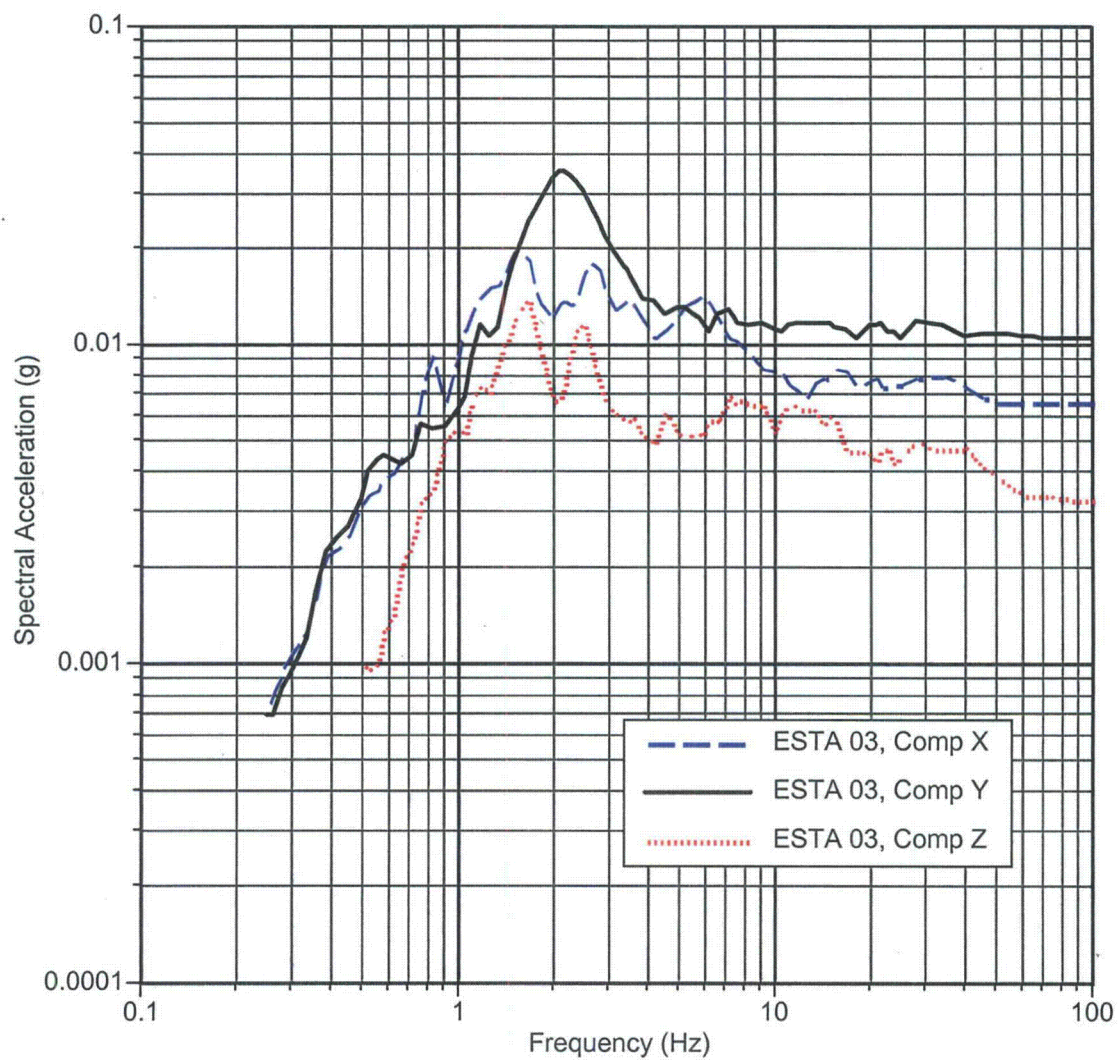
Figure 15. Response spectra at 5% damping for ESTA 03. (64' elev, U1 in Aux. Bldg).

DCPP: Station ESTA04, Parkfield EQ (09/28/04), Mw=6.0
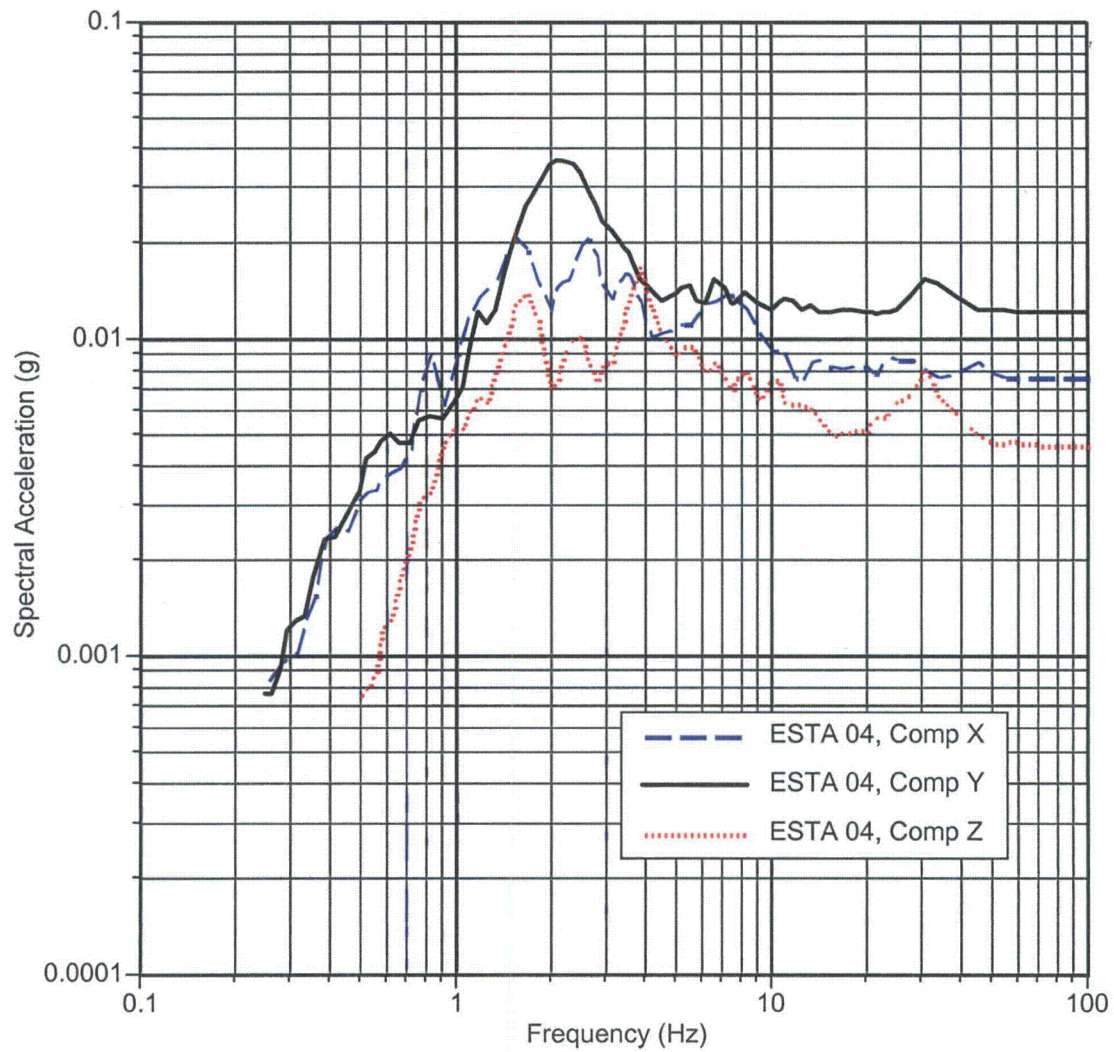
Figure 16. Response spectra at 5% damping for ESTA 04 (89' elev, area FW outside U1 containment on Base Slab).
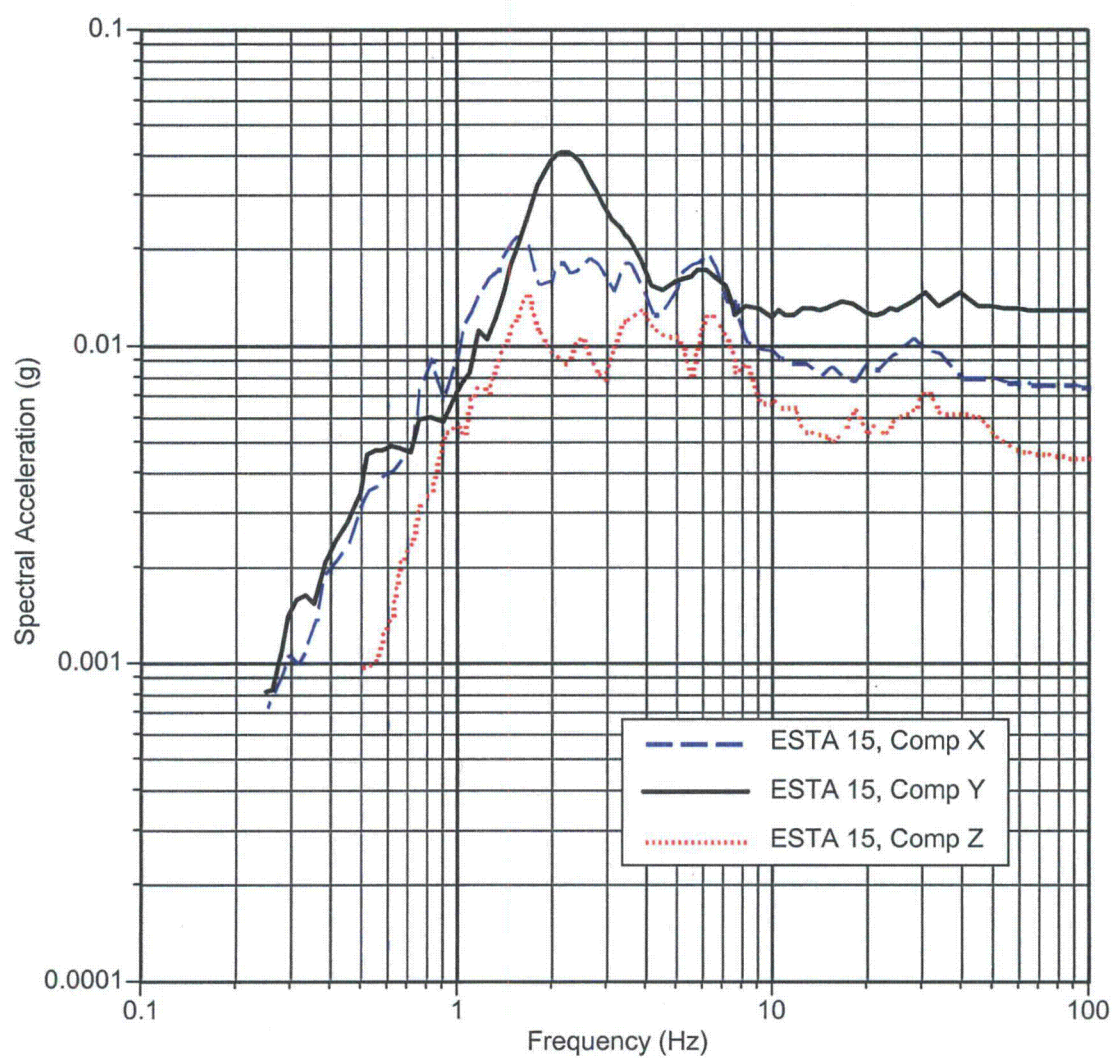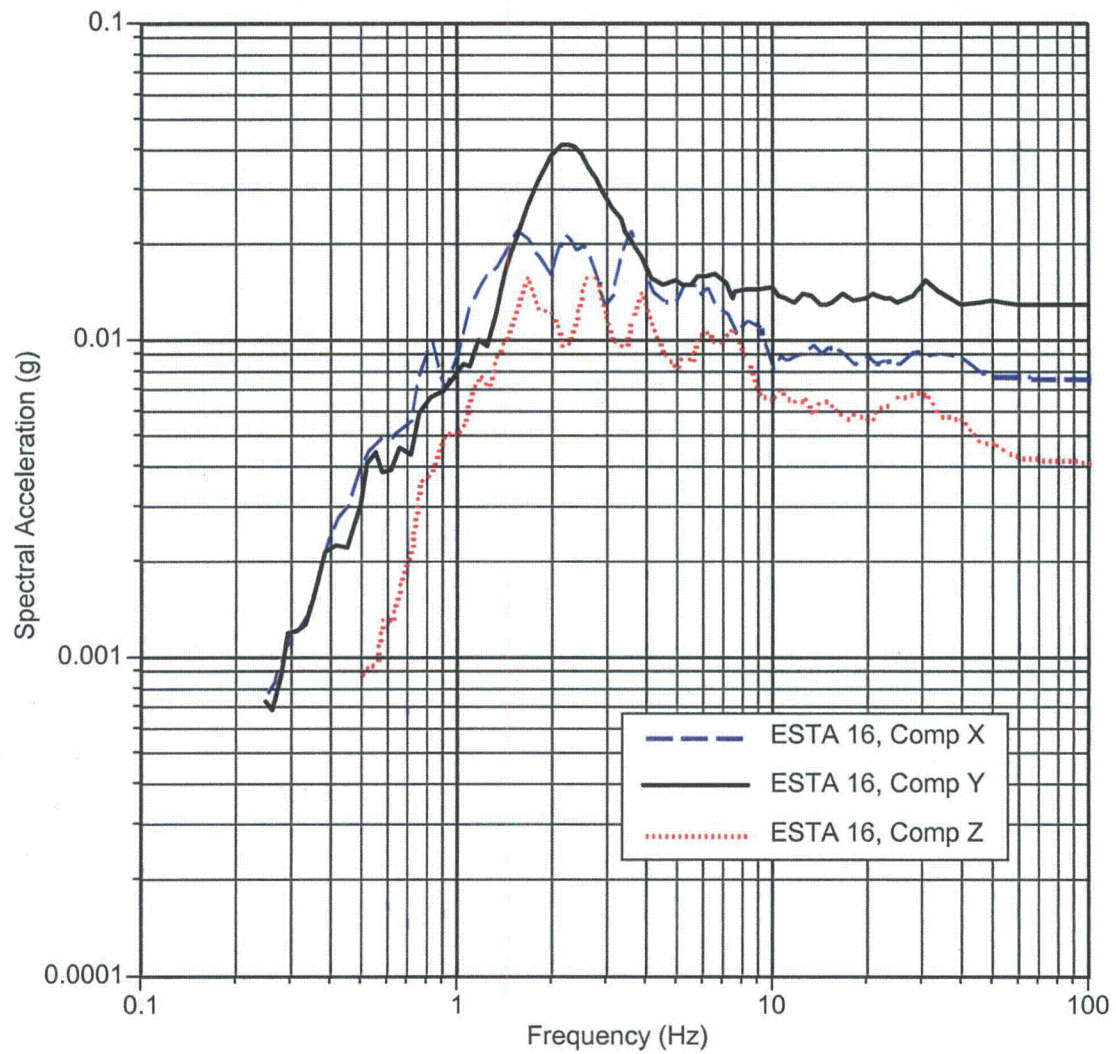
Figure 17. Response spectra at 5% damping for ESTA 05(89' elev, outside U1 containment on Base Slab).
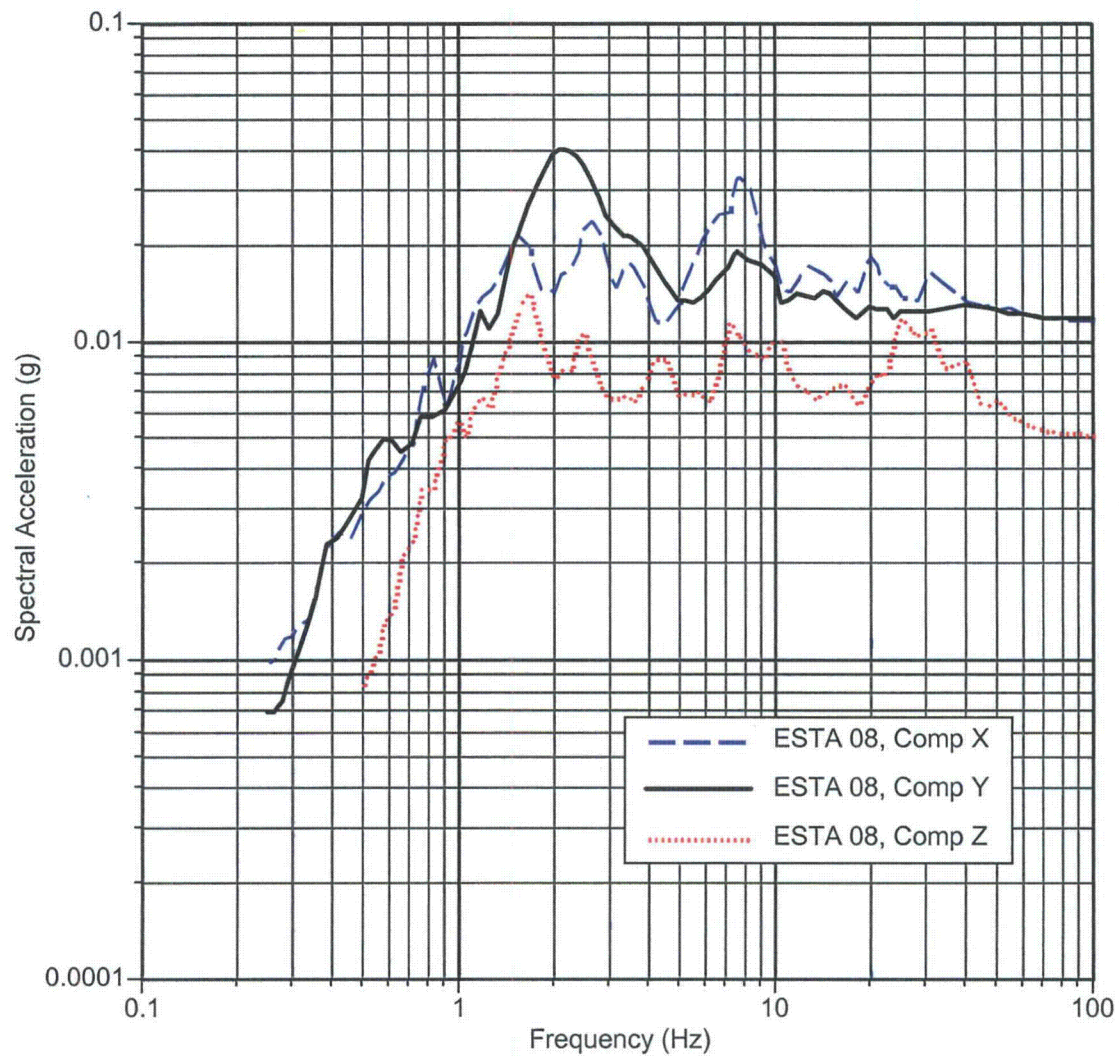
Figure 18. Response spectra at 5% damping for ESTA 08 (140' elev in U1 containment at operating floor).
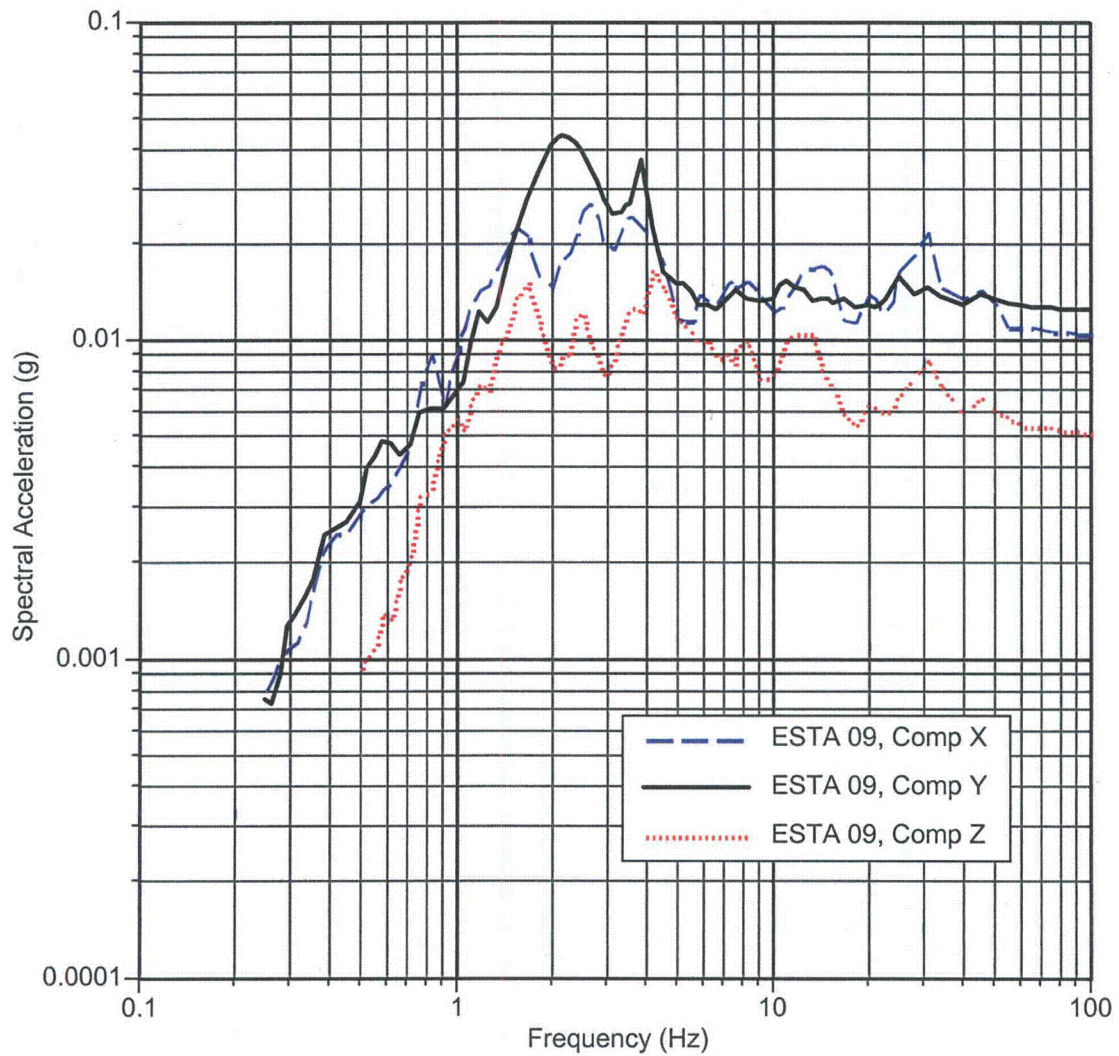
Figure 19. Response spectra at 5% damping for ESTA 09 (140' elev in U1 containment on liner).
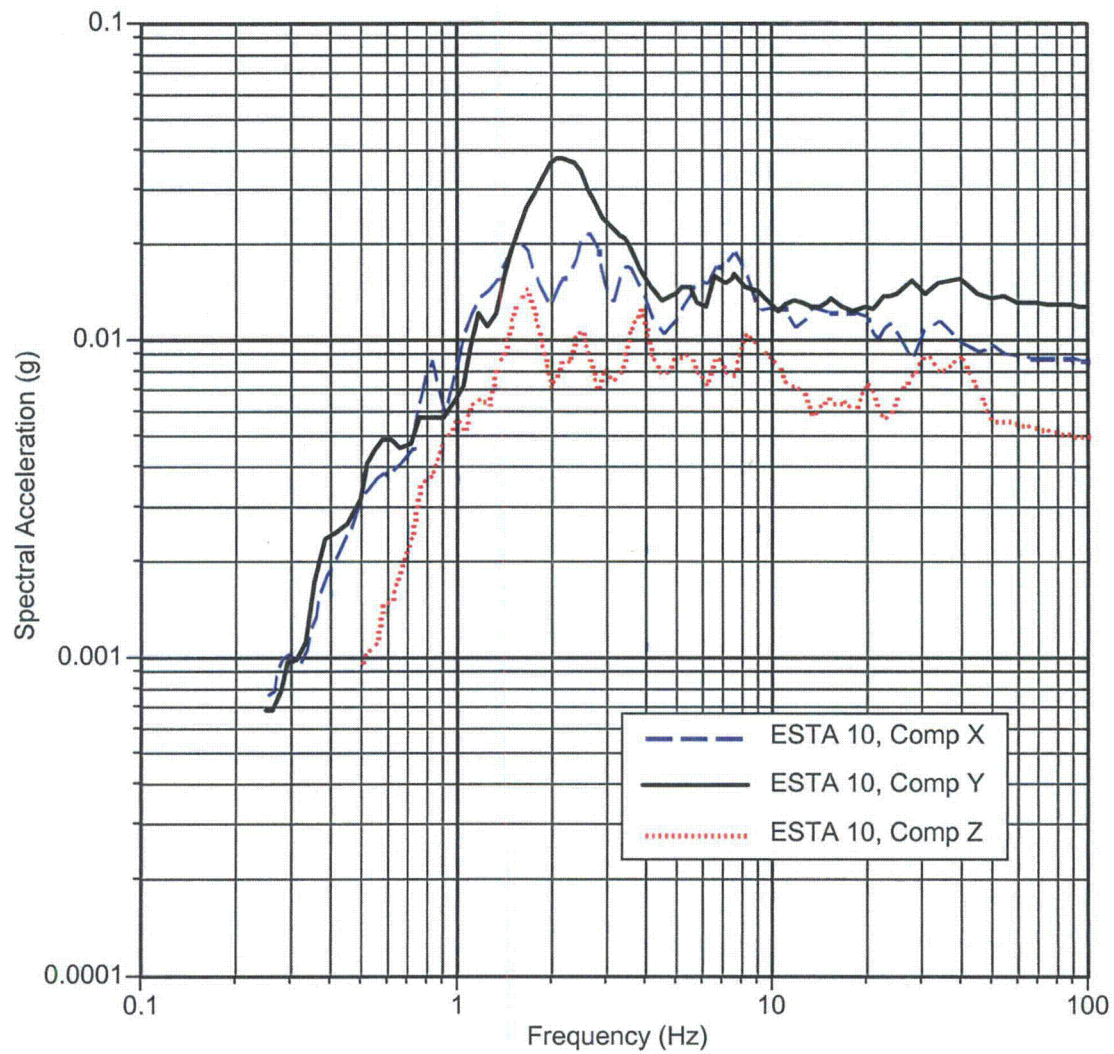
Figure 20. Response spectra at 5% damping for ESTA 10 (117' elev in U1 containment on bio shield).

Figure 21. Response spectra at 5% damping for ESTA 14 (89' elev outside U2 containment on base slab).

Figure 22. Response spectra at 5% damping for ESTA 15 (89' elev outside U2 containment on base slab).

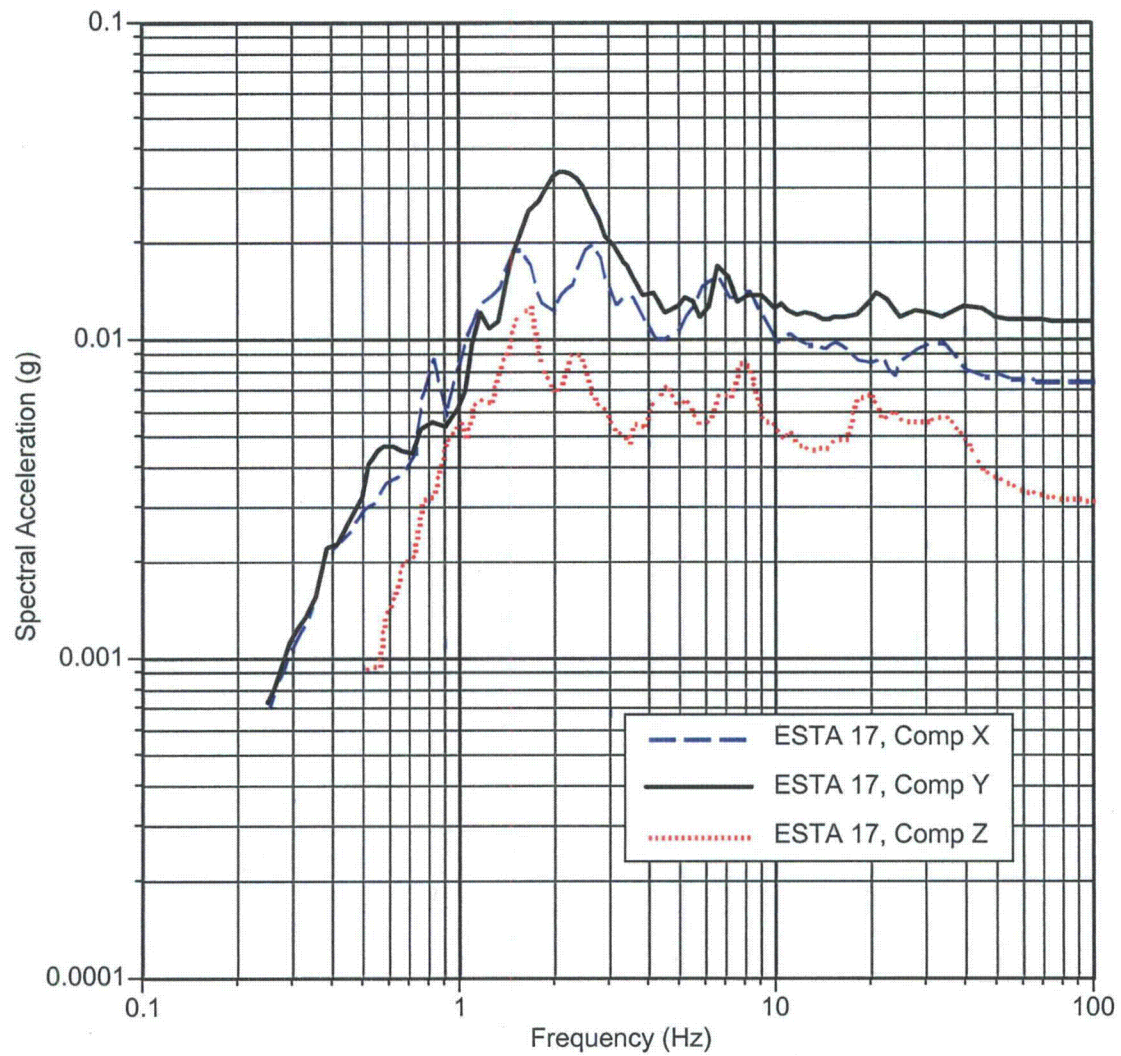Figure 23. Response spectra at 5% damping for ESTA 16 (89' elev outside U2 containment on base slab).

DCPP: Station ESTA17, Parkfield EQ (09/28/04), Mw=6.0

Figure 24. Response spectra at 5% damping for ESTA 17 (100' elev U1 Aux/Fuel Handling Building).

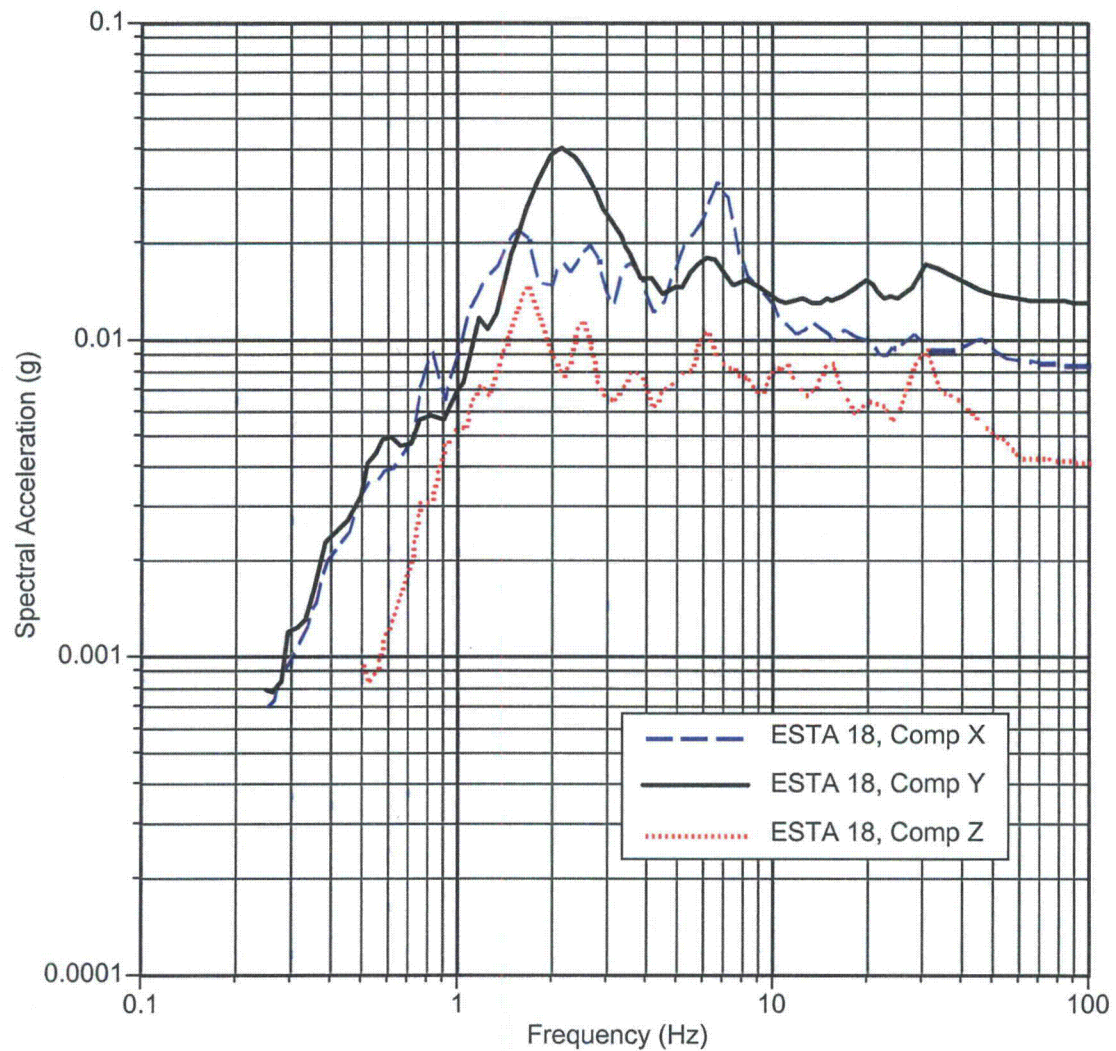DCPP: Station ESTA01, Parkfield EQ (09/28/04), Mw=6.0

Figure 25. Response spectra at 5% damping for ESTA 18 (100' elev U1 Aux Building).
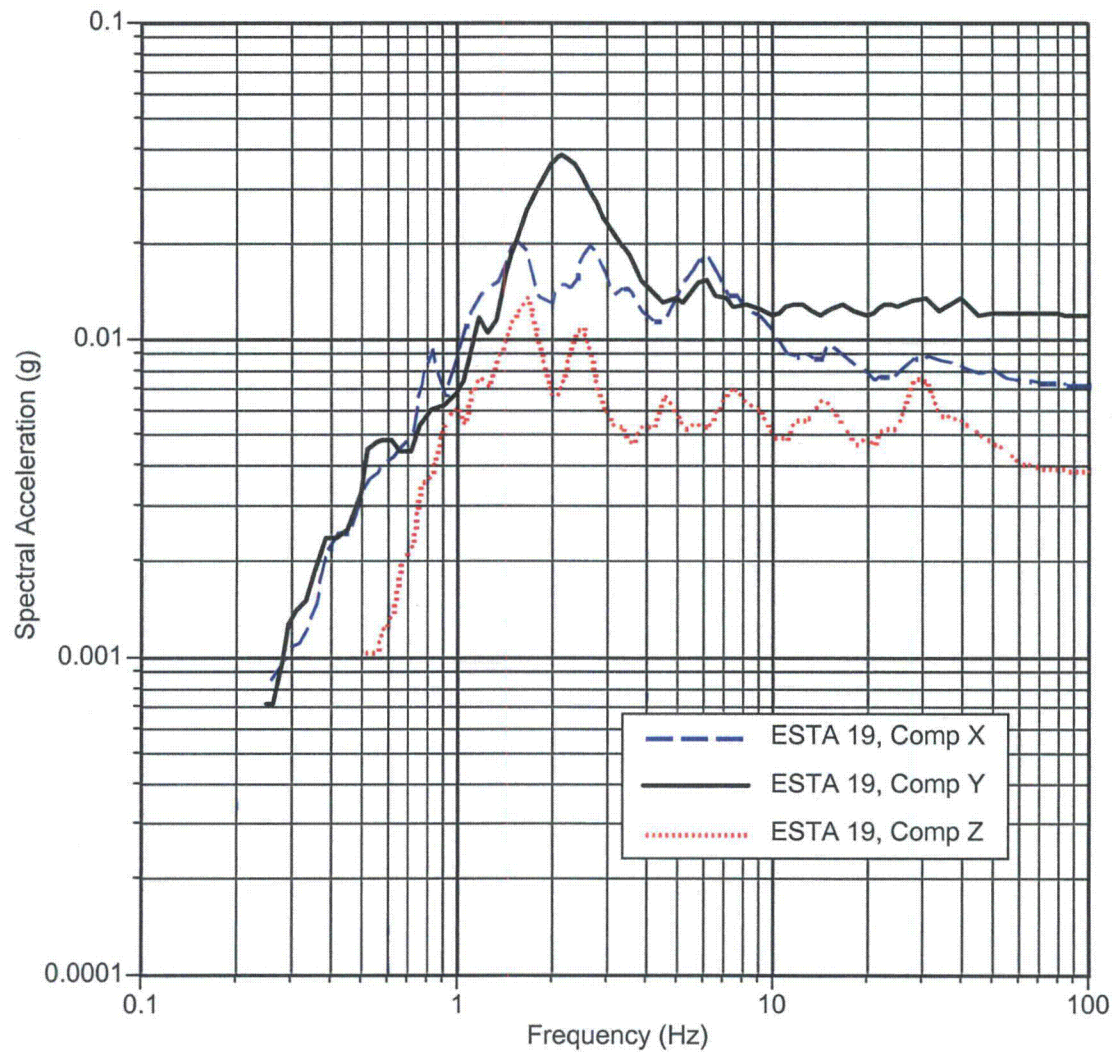
Figure 26. Response spectra at 5% damping for ESTA 19 (100' elev U1 & U2 Aux Building).

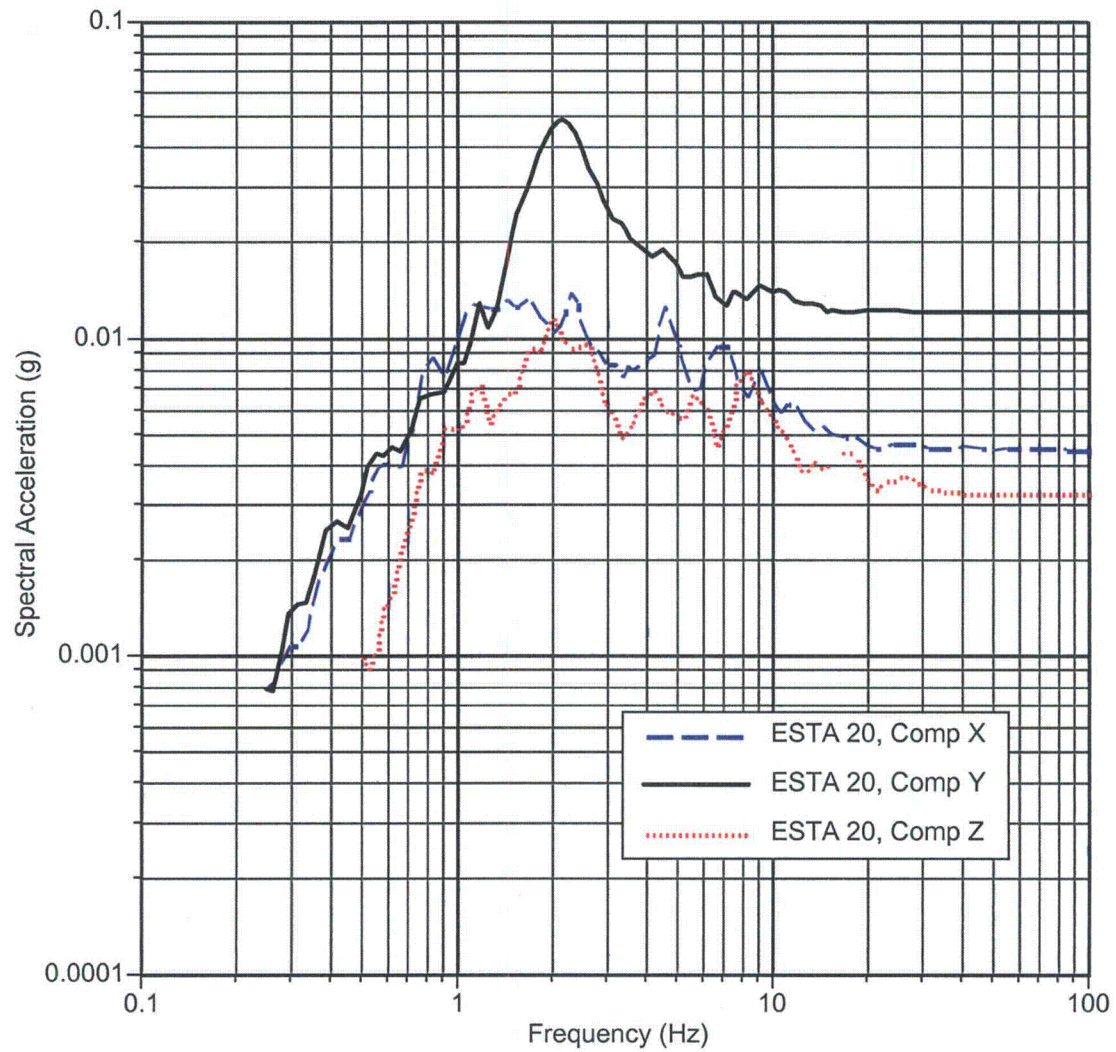DCPP: Station ESTA20, Parkfield EQ (09/28/04), Mw=6.0

Figure 27. Response spectra at 5% damping for ESTA 20 (Free Field near Raw Water reservoirs).
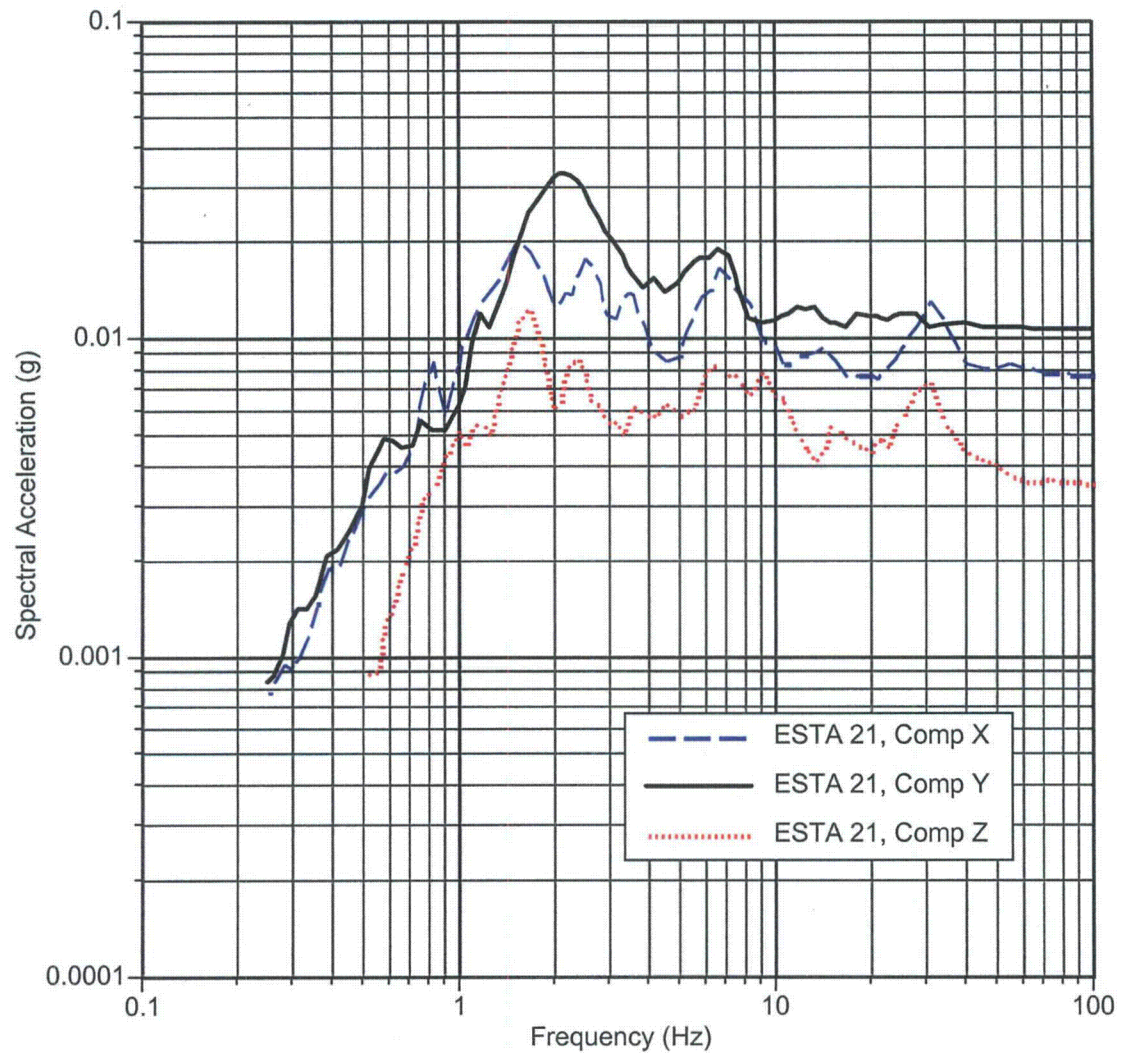
Figure 28. Response spectra at 5% damping for ESTA 21 (85' elev. U1 Turb Bldg North end of switch gear room).

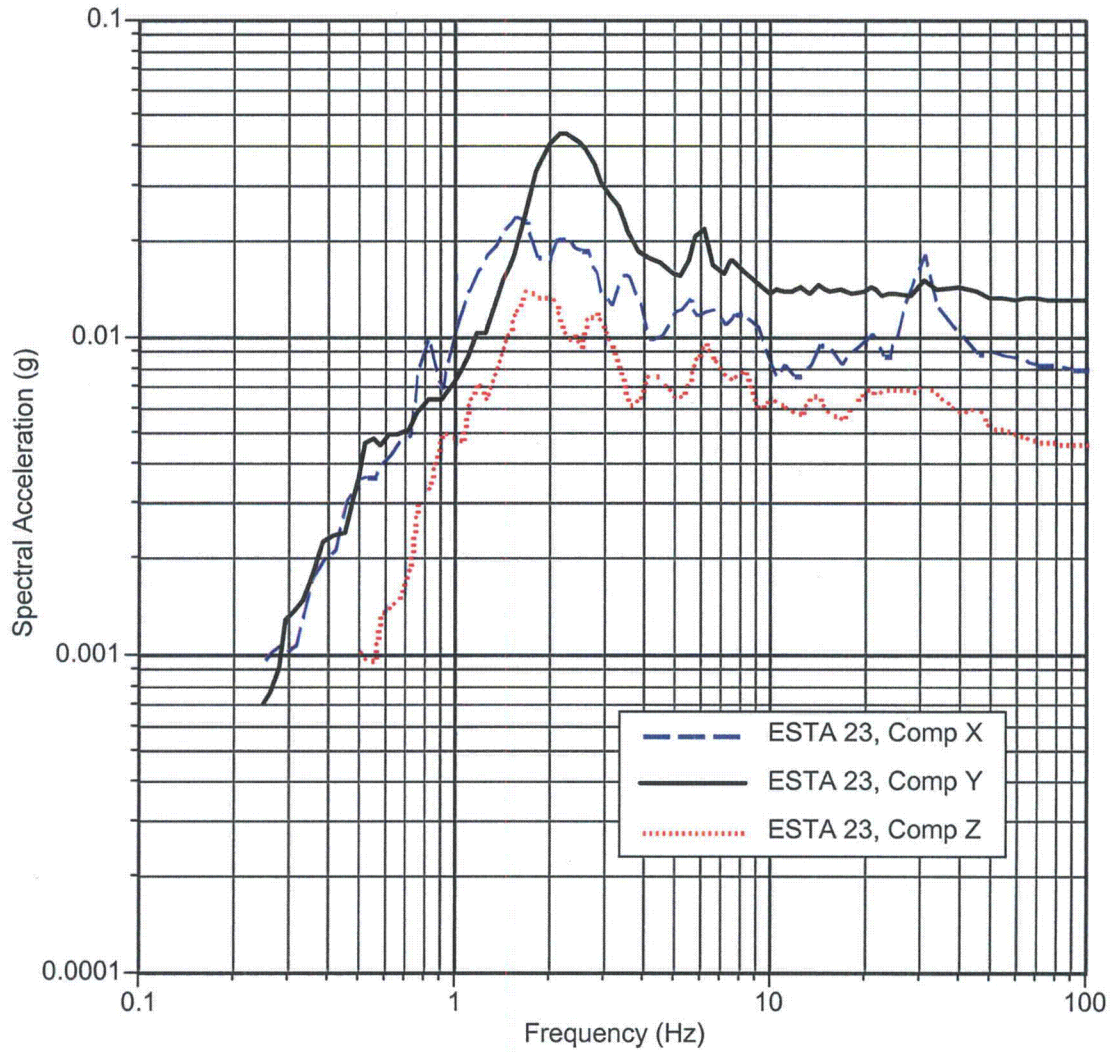DCPP: Station ESTA23, Parkfield EQ (09/28/04), Mw=6.0

Figure 29. Response spectra at 5% damping for ESTA 23 (85' elev. U2 Turbine Building South end Stairs).

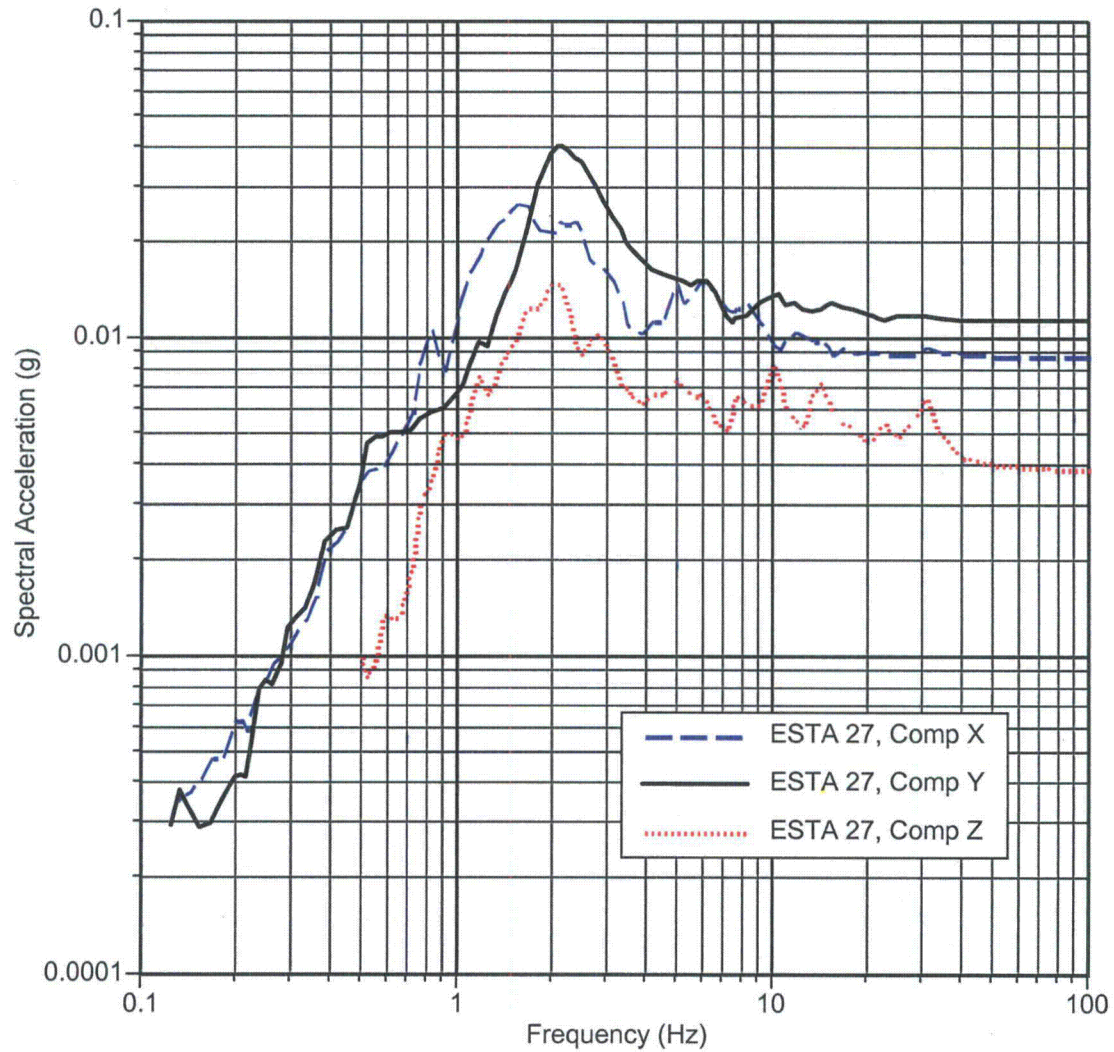DCPP: Station ESTA27, Parkfield EQ (09/28/04), Mw=6.0

Figure 30. Response spectra at 5% damping for ESTA 27 (82' elev. Free Field in underground vault near Fitness Trailer).
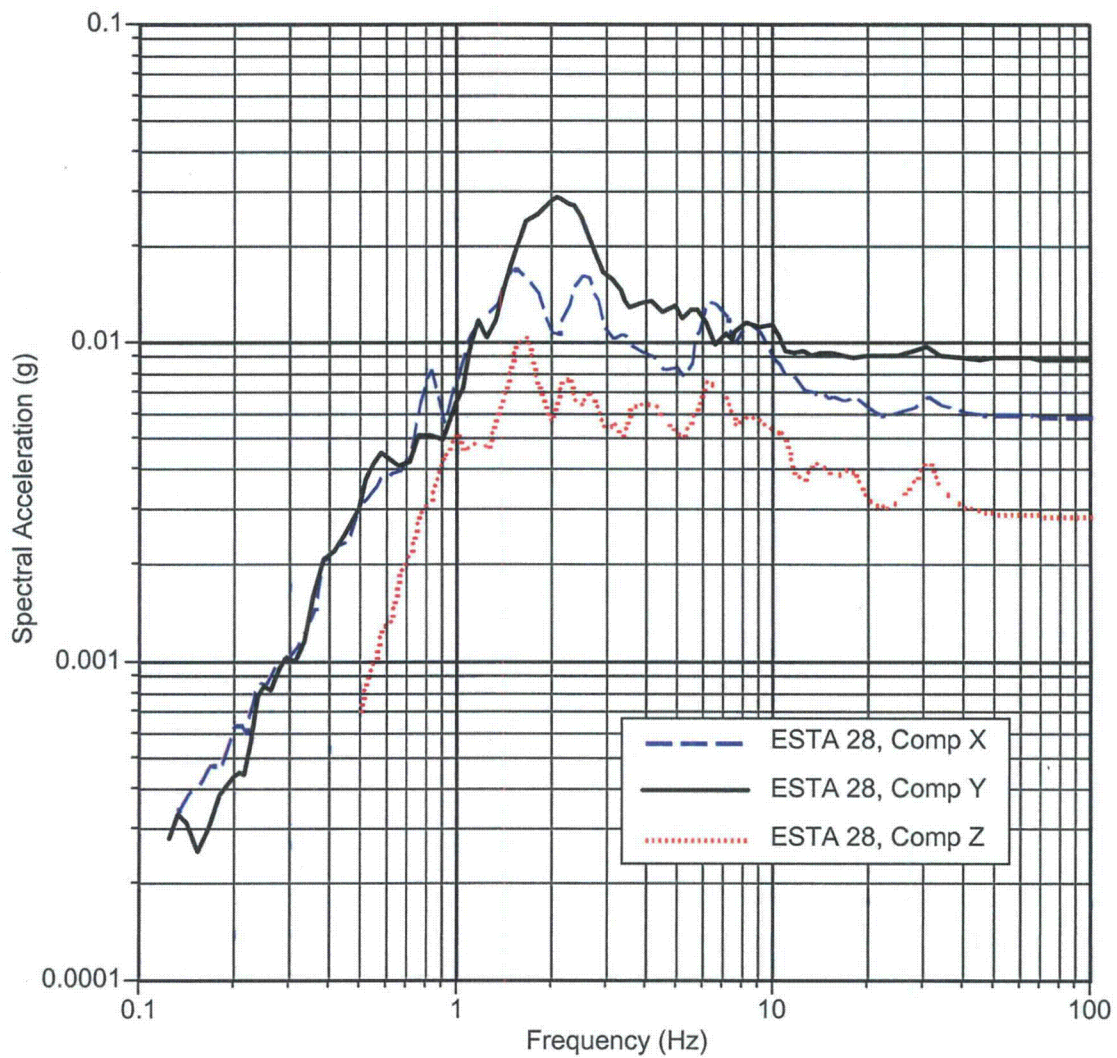
Figure 31. Response spectra at 5% damping for ESTA 28 (85' elev. Free Field in paved area north of U1 containment).

Table 1. Peak values from the DCPP recordings of the 2004 Parkfield Earthquake after filtering and baseline corrections. See Figures 6 and 7 for instrument locations.

Station	PGA(g)			PGV (cm/s)			PGD (cm)		
	X	Y	Z	X	Y	Z	X	Y	Z
ESTA01	0.0069	0.0119	0.0045	0.711	0.990	0.310	0.127	0.128	0.044
ESTA02	0.0137	0.0220	0.0080	0.985	1.329	0.366	0.169	0.183	0.068
ESTA03	0.0065	0.0105	0.0032	0.682	0.907	0.317	0.124	0.112	0.043
ESTA04	0.0075	0.0121	0.0046	0.717	0.958	0.324	0.131	0.120	0.042
ESTA05	0.0072	0.0115	0.0036	0.651	0.883	0.310	0.119	0.100	0.043
ESTA08	0.0118	0.0118	0.0051	0.0727	1.012	0.324	0.125	0.130	0.044
ESTA09	0.0105	0.0124	0.0051	0.799	1.071	0.331	0.124	0.119	0.046
ESTA10	0.0087	0.0127	0.0050	0.752	0.964	0.358	0.136	0.123	0.047
ESTA14	0.0077	0.0133	0.0051	0.696	1.036	0.367	0.127	0.125	0.042
ESTA15	0.0075	0.0128	0.0044	0.671	1.017	0.297	0.116	0.122	0.049
ESTA16	0.0075	0.0128	0.0041	0.735	0.906	0.352	0.129	0.104	0.042
ESTA17	0.0074	0.0113	0.0032	0.687	0.912	0.323	0.111	0.043	0.179
ESTA18	0.0083	0.0131	0.0041	0.741	0.971	0.299	0.122	0.119	0.041
ESTA19	0.0072	0.0119	0.0038	0.691	0.965	0.328	0.129	0.132	0.044
ESTA20	0.0045	0.0120	0.0032	0.0628	0.965	0.293	0.113	0.125	0.044
ESTA21	0.0077	0.0106	0.0035	0.733	0.903	0.309	0.117	0.113	0.038
ESTA23	0.0079	0.0131	0.0046	0.738	1.007	0.284	0.139	0.128	0.039
ESTA27	0.0087	0.0113	0.0039	0.882	0.966	0.289	0.163	0.154	0.040
ESTA28	0.0059	0.0088	0.0028	0.684	0.774	0.295	0.179	0.152	0.037

THIS PAGE IS AN OVERSIZED DRAWING OR FIGURE,

THAT CAN BE VIEWED AT THE RECORD TITLE :

PLATE 1
GEOLOGIC MAP OF THE SHORELINE
FAULT ZONE STUDYAREA

THESE DRAWINGS CAN BE ACCESSED WITHIN THE ADAMS PACKAGE WITHIN THIS PACKAGE...

D01

THIS PAGE IS AN OVERSIZED DRAWING OR FIGURE,

THAT CAN BE VIEWED AT THE RECORD TITLE :

PLATE B-1A
NORTH SECTION GEOLOGIC MAP
MORRO BAY TO POINT BUCHON

THESE DRAWINGS CAN BE
ACCESSED WITHIN THE ADAMS
PACKAGE WITHIN THIS PAKAGE...

D02

THIS PAGE IS AN OVERSIZED DRAWING OR FIGURE,

THAT CAN BE VIEWED AT THE
RECORD TITLED DRAWING NO:

PLATE B-1B
CENTRAL SECTION GEOLIC MAP
POINT BUCHON TO DOUBLE ROCK

THESE DRAWINGS CAN BE
ACCESSED WITHIN THE ADAMS
PACKAGE WITHIN THIS PACKAGE...

D03

THIS PAGE IS AN OVERSIZED DRAWING OR FIGURE,

THAT CAN BE VIEWED AT THE RECORD TITLED: DRAWING NO:

PLATE B-1C
SOUTH SECTION GEOLOGIC MAP
DOUBLE ROCK TO SAN LUIS HILL

THESE DRAWINGS CAN BE ACCESSED WITHIN THE ADAMS PACKAGE WITHIN THIS PACKAGE...

D04

THIS PAGE IS AN OVERSIZED DRAWING OR FIGURE,

THAT CAN BE VIEWED AT THE RECORD TITLED

PLATE B-1D
SOUTHEAST SECTION GEOLOGIC
MAP POINT SAN LUIS TO PISMO
BEACH

WITHIN THIS PACKAGE...OR
BY SEARCHING USING THE
DOCUMENT/REPORT NO.

D05

THIS PAGE IS AN OVERSIZED DRAWING OR FIGURE,

THAT CAN BE VIEWED AT THE
RECORD TITLED:

PLATE I – 1B
MAP OF SUBMERGED WAVE-CUT
PLATFORMS AND STRANDLINES

WITH IN THIS PACKAGE...OR
BY SEARCHING USING THE
DOCUMENT/REPORT NO.

D07

THIS PAGE IS AN OVERSIZED DRAWING OR FIGURE,

THAT CAN BE VIEWED AT THE RECORD TITLED:

PLATE I-1C
MAP OF SUBMERGED WAVE-CUT
PLATFORMS AND STRANDLINES

WITHIN THIS PACKAGE...OR
BY SEARCHING USING THE
DOCUMENT/REPORT NO.

D08

THIS PAGE IS AN OVERSIZED DRAWING OR FIGURE,

THAT CAN BE VIEWED AT THE RECORD TITLED:

PLATE I – 1D

MAP OF SUBMERGED WAVE-CUT PLATFORMS AND STRANDLINES

WITHIN THIS PACKAGE...OR BY SEARCHING USING THE DOCUMENT/REPORT NO.

D-09

THIS PAGE IS AN OVERSIZED DRAWING OR FIGURE,

THAT CAN BE VIEWED AT THE
RECORD TITLED:

PLATE I- 2A

MAP SHOWING SUBMERGED
STRANDLINES, WAVE-CUT
PLATFORMS, AND GEOLOGY

WITHIN THIS PACKAGE...OR
BY SEARCHING USING THE
DOCUMENT/REPORT NO.

D-10

THIS PAGE IS AN OVERSIZED DRAWING OR FIGURE,

THAT CAN BE VIEWED AT THE
RECORD TITLED:

PLATE I-2B

MAP SHOWING SUBMERGED
STRANDLINES, WAVE-CUT
PLATFORMS, AND GEOLOGY

WITHIN THIS PACKAGE...OR
BY SEARCHING USING THE
DOCUMENT/REPORT NO.

D-11

THIS PAGE IS AN OVERSIZED DRAWING OR FIGURE,

THAT CAN BE VIEWED AT THE RECORD TITLE :

PLATE I-2C

MAP SHOWING SUBMERGED STRANDLINES, WAVE-CUT PLATFORMS, AND GEOLOGY

THESE DRAWINGS CAN BE ACCESSED WITHIN THE ADAMS PACKAGE WITHIN THIS PACKAGE...

D12

THIS PAGE IS AN OVERSIZED DRAWING OR FIGURE,

THAT CAN BE VIEWED AT THE RECORD TITLE :

PLATE I-2D

MAP SHOWING SUBMERGED STRANDLINES, WAVE-CUT PLATFORMS, AND GEOLOGY

THESE DRAWINGS CAN BE ACCESSED WITHIN THE ADAMS PACKAGE WITHIN THIS PAKAGE...

D13

THIS PAGE IS AN OVERSIZED DRAWING OR FIGURE,

THAT CAN BE VIEWED AT THE RECORD TITLED DRAWING NO:

LONGITUDINAL PROFILE ALONG COASTLINE SHOWING CORRELATION OF SUBMERGED STRANDLINES

PLATE I-3A

THESE DRAWINGS CAN BE ACCESSED WITHIN THE ADAMS PACKAGE WITHIN THIS PACKAGE...

D14

THIS PAGE IS AN OVERSIZED DRAWING OR FIGURE,

THAT CAN BE VIEWED AT THE RECORD TITLED: DRAWING NO:

LONGITUDINAL PROFILE ALONG COASTLINE SHOWING CORRELATION OF SUBMERGED STRANDLINES (ALTERNATIVE 1)

PLATE I-3B

THESE DRAWINGS CAN BE ACCESSED WITHIN THE ADAMS PACKAGE WITHIN THIS PACKAGE...

D15

THIS PAGE IS AN OVERSIZED DRAWING OR FIGURE,

THAT CAN BE VIEWED AT THE RECORD TITLED

LONGITUDINAL PROFILE ALONG COASTLINE SHOWING CORRELATION OF SUBMERGED STRANDLINES (ALTERNATIVE 2)

PLATE I-3C

WITHIN THIS PACKAGE...OR BY SEARCHING USING THE DOCUMENT/REPORT NO.

D16

THIS PAGE IS AN OVERSIZED DRAWING OR FIGURE,

THAT CAN BE VIEWED AT THE RECORD TITLED:

LONGITUDINAL PROFILE ALONG COASTLINE SHOWING CORRELATION OF SUBMERGED STRANDLINES (ALTERNATIVE 3)

PLATE I-3D

WITHIN THIS PACKAGE...OR BY SEARCHING USING THE DOCUMENT/REPORT NO.

D17x